AD_____


AWARD NUMBER:  W81XWH-04-1-0590



TITLE:  Constrained Adaptive Beamforming for Improved Contrast in Breast Ultrasound



PRINCIPAL INVESTIGATOR: William F. Walker, Ph.D.



CONTRACTING ORGANIZATION:  University of Virginia
                                              Charlottesville, Virginia  22904


REPORT DATE:  June 2006



TYPE OF REPORT:  Annual



PREPARED FOR:  U.S. Army Medical Research and Materiel Command
                        Fort Detrick, Maryland  21702-5012


DISTRIBUTION STATEMENT: Approved for Public Release;
                                           Distribution Unlimited

# REPORT DOCUMENTATION PAGE

Public reporting burden for this collection of information is estimated to average 1 hour per response, including the time for reviewing instructions, searching existing data sources, gathering and maintaining the data needed, and completing and reviewing this collection of information. Send comments regarding this burden estimate or any other aspect of this collection of information, including suggestions for reducing this burden to Department of Defense, Washington Headquarters Services, Directorate for Information Operations and Reports (0704-0188), 1215 Jefferson Davis Highway, Suite 1204, Arlington, VA 22202-4302. Respondents should be aware that notwithstanding any other provision of law, no person shall be subject to any penalty for failing to comply with a collection of information if it does not display a currently valid OMB control number. **PLEASE DO NOT RETURN YOUR FORM TO THE ABOVE ADDRESS.**

| 1. REPORT DATE *(DD-MM-YYYY)* | 2. REPORT TYPE | 3. DATES COVERED *(From - To)* |
|---|---|---|
| 01-06-2006 | Annual | 1 Jun 2005 – 31 May 2006 |

**4. TITLE AND SUBTITLE**

Constrained Adaptive Beamforming for Improved Contrast in Breast Ultrasound

**5a. CONTRACT NUMBER**

**5b. GRANT NUMBER**
W81XWH-04-1-0590

**5c. PROGRAM ELEMENT NUMBER**

**6. AUTHOR(S)**

William F. Walker, Ph.D.

E-Mail:  bwalker@virginia.edu

**5d. PROJECT NUMBER**

**5e. TASK NUMBER**

**5f. WORK UNIT NUMBER**

**7. PERFORMING ORGANIZATION NAME(S) AND ADDRESS(ES)**

University of Virginia
Charlottesville, Virginia  22904

**8. PERFORMING ORGANIZATION REPORT NUMBER**

**9. SPONSORING / MONITORING AGENCY NAME(S) AND ADDRESS(ES)**
U.S. Army Medical Research and Materiel Command
Fort Detrick, Maryland  21702-5012

**10. SPONSOR/MONITOR'S ACRONYM(S)**

**11. SPONSOR/MONITOR'S REPORT NUMBER(S)**

**12. DISTRIBUTION / AVAILABILITY STATEMENT**
Approved for Public Release; Distribution Unlimited

**13. SUPPLEMENTARY NOTES**

**14. ABSTRACT**

Ultrasonic imaging plays an important role as an adjunct to mammography, with an emerging role in breast cancer screening. Ultrasound's real-time nature, lack of ionizing radiation, and relative comfort for the patient make it an attractive imaging choice. Unfortunately, ultrasound image quality is often limited. We hypothesize that bright scatters seriously degrade ultrasound images by introducing image clutter. In the breast bright off-axis echoes may originate from Cooper's ligaments, structured glandular tissue, calcification, fat-soft tissue interfaces, or other structure. While we initially proposed using a variant of the Frost Adaptive Beamformer to reduce clutter, we have since discovered that this technique is non-optimal for our application. Extensive literature reviews have led us to utilize a recently proposed method, Spatial Processing Optimized and Constrained (SPOC). In initial simulations this method not only dramatically reduces image clutter, but also yields super-resolution. We are actively refining this method while developing the experimental tools needed for in vivo testing.

**15. SUBJECT TERMS**
Imaging, Ultrasound, Diagnosis, Non-Invasive

| 16. SECURITY CLASSIFICATION OF: | | | 17. LIMITATION OF ABSTRACT | 18. NUMBER OF PAGES | 19a. NAME OF RESPONSIBLE PERSON USAMRMC |
|---|---|---|---|---|---|
| a. REPORT | b. ABSTRACT | c. THIS PAGE | | | 19b. TELEPHONE NUMBER *(include area code)* |
| U | U | U | UU | 135 | |

# Table of Contents

**Introduction:**

Ultrasonic imaging currently plays an important role as an adjunct to mammography [1, 2]. Ultrasound's real-time nature, lack of ionizing radiation, and relative comfort for the patient make it an attractive choice for applications which include the differentiation of fluid filled cysts and solid masses, differentiation of benign and malignant lesions, and guidance of needle and core biopsy procedures. Recent studies have even shown the potential of ultrasound as a screening tool, especially for pre-menopausal women whose radio-dense breast tissue seriously limits x-ray mammography [3]. In both differential diagnosis and screening applications however, ultrasound image quality is limited, with high levels of background clutter representing a significant problem in many patients.

While the cause of high background clutter and poor breast image quality has not been determined with certainty, it is widely held that acoustic velocity inhomogeneities in breast tissue cause defocusing of the acoustic beam. This distortion manifests itself through mainlobe broadening and increasing sidelobe levels. Numerous researchers, including the Principal Investigator, have suggested that this problem, known as phase aberration, might be corrected through the application of compensating time delays [4-6], a combination of delay and amplitude corrections [7], or other more complex techniques [8-10]. While proposed phase aberration correction methods have been shown to have great potential in *ex vivo* or other non real-time environments, there has been limited evidence of significant clinical image improvement. The development of a real-time phase aberration correction system at the GE Global Research Center has shown that real-time phase correction is possible, however *in vivo* results using 1.5-D arrays show contrast improvements of only about 3 dB in the abdomen [11, 12]. This unimpressive outcome may result from imperfect algorithm optimization, or perhaps a lower level of *in vivo* phase aberration than previously suspected. This latter hypothesis is supported by recent phase aberration measurements performed at Duke University which indicate *in vivo* phase aberrations of only ~25ns RMS (Root Mean Squared) with a 3.5 mm FWHM (Full Width at Half Maximum) [13]. The limited improvements of real-time phase correction, coupled with low measured aberrations, suggest that phase aberration may not represent the major source of breast image degradation.

If phase aberration is not the primary factor limiting breast image quality, then what is? We hypothesize that localized bright scatterers seriously degrade ultrasound images by introducing broad image clutter. Figure 1 shows single channel Radio Frequency (RF) echo data obtained from calcifications in the thyroid of a human subject at Duke University. A focused transmit beam was used and RF data was acquired from each element in a 1.5-D array consisting of approximately 1000 elements. Figure 1 shows data from one row of this array after application of geometrically determined focal delays. At least three clear waveforms are visible in this data set, with each probably resulting from a single calcification. Although summation across channels to form an RF image line would amplify the echo coming from directly in front of the array, it would not entirely eliminate the two other visible targets. These non-focal targets would appear in this image line as clutter, reducing image contrast. In addition to the three dominant calcification waveforms, the data set also includes echoes from background speckle. These background echoes also include discernable off-axis scatterers that undoubtedly generate further clutter in the image. Note that the thyroid data presented in figure 1 is similar in appearance to breast data obtained at Duke. In the breast bright off-axis echoes may originate from Cooper's ligaments, highly structured glandular tissue, calcification, fat-soft tissue interfaces, or other tissue structures.

The presence of bright off-axis scatterers and the image degradation that they cause is not surprising. It is well known that the acoustic reflectivity of targets within the body covers many orders of magnitude. It is precisely for this reason that manufacturers employ aggressive apodization to reduce sidelobe levels in diagnostic ultrasound. It has also been argued that harmonic imaging is effective at improving image quality because it further reduces sidelobe levels and therefore reduces the spatial spread of bright targets. The detrimental impact of bright scatterers on ultrasound image quality is recognized in experimental data, physical intuition, and years of experience in ultrasound system design.
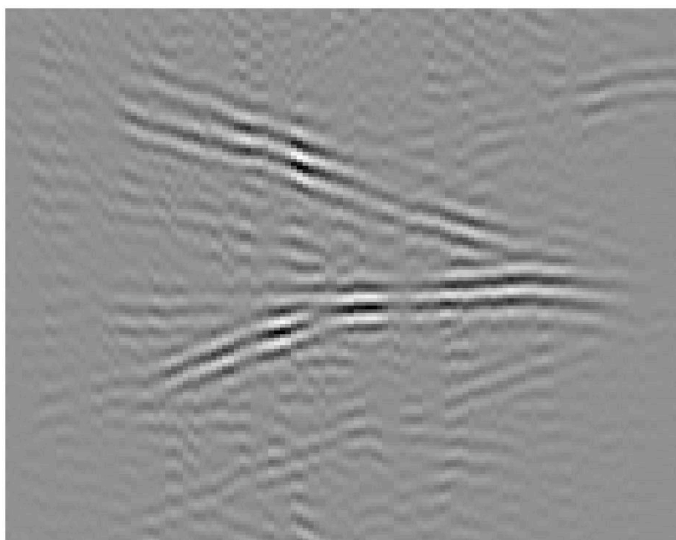
Figure 1: Single channel data obtained *in vivo* from a human thyroid. At least three bright scatterers (likely microcalcifications) are visible. While one target lies near the focus, the other two are off-axis and will contribute clutter to this image line. Off-axis targets are also visible within the speckle generating background echoes. (Data courtesy Gregg Trahey, Duke University.)

The impact of a few bright targets in an otherwise dim image has been well studied in both RADAR and SONAR. In SONAR the detection of an intentionally stealthy submarine among many noisy ships requires separating out a signal that is orders of magnitude below the signals from other nearby targets. A broad variety of adaptive beamforming algorithms have been developed for this scenario. It is the goal of this research project to evaluate the potential applicability of these methods in medical ultrasound.

**Body:**

**Summary of First Year Progress:**

In our original proposal we described a research plan to explore the potential of a novel technique the Constrained Adaptive Beamformer (CAB) build upon a particularly elegant and well studied method for adaptive beamforming, the Frost Adaptive Beamformer (FAB). This FAB, represents the beamforming process using a linear algebra formulation. A set of beamformer weights, corresponding to an individual FIR filter for each element of the array, is determined adaptively from the data acquired by the sensor array. The weights minimize the energy in the beamsum signal, subject to the constraint that the beamformer must exhibit a given impulse response for signals received from the array look direction. In work performed prior to the initiation of this grant we built upon FAB and modified it to yield the CAB, which works in transmit-receive systems, can be applied to near-field data, and can handle the broad bandwidths and limited stationarity of ultrasound data [14, 15]. As our initial proposal indicated, the CAB showed great potential with both simulation and experimental ultrasound data.

As described in last year's progress report, we found the potential of the CAB to be limited by an excessive computational cost and a high performance dependency on the target characteristics. When applied to point target data we found that straight-forward implementation of the algorithm termed Single-Iteration CAB (SI-CAB) yielded excellent results; the main-lobe was narrowed and sidelobes were reduced, improving both spatial resolution and image contrast. When we applied the same algorithm to data from a point target embedded within a speckle target however the results were much more complicated. While the center of the point target was better focused, strange behavior was exhibited in the "tails" or side-lobes of the point response. In these areas the algorithm not only eliminated the clutter contribution of the bright target, but it also eliminated the background speckle signal. Thus the output image was black in the tail regions of point target, regardless of what sort of target was actually present. This was clearly an unsatisfactory result. In an attempt to compensate for this problem a previous student of the Principal Investigator (Jake Mann) developed an alternate version of the algorithm that he called Multi-Iteration CAB or MI-CAB. This algorithm repeatedly performed the SI-CAB algorithm on windows of data with partial overlap. It then averaged output results in areas of overlap. Although this approach eliminated some of the artifacts present in speckle regions it also showed much worse performance than SI-CAB for point targets. Thus we were left with the highly unsatisfactory situation of requiring different algorithms for different target types.

In our first year of support under this grant we performed an extensive review of the adaptive beamforming literature. This effort yielded two important conclusions. First, that FAB (and by extension CAB) is not an appropriate tool for adaptive beamforming when only a single snapshot of the target environment is available. This simple conclusion led us to search for an alternate algorithm. Our second conclusion was that from the dozens of algorithms and hundreds of papers published in this area, only the SPOC (Spatial Processing Optimized and Constrained) algorithm could be readily modified to meet the constraints of medical ultrasound imaging. Based on these conclusions, we have altered our research effort to focus on adapting SPOC to meet the constraints of our problem and to evaluate the performance of this method.

Another major thrust in the first year of support was the development of experimental tools to enable measurement of off-axis scattering *in vivo*. Ongoing challenges with the development of single channel acquisition on our Philips SONOS 5500 and with reverse engineering signal processing on our GE Logiq 700MR system have led us to move to a new experimental platform, the Ultrasonix Sonix RP system. We describe developments on that system below.

Finally, the other major thrust in the first year was development of novel ultrasound simulation tools. This work has been extended, as described below, and is expected to yield two new publications and potentially significant open-source software tool in the coming year.

**Conventional Beamformer Optimization:**

The value of adaptive beamforming is only apparent when we can quantify image quality and when we have a clear measure of the limits on the performance of optimized conventional beamforming. In the past year we have made significant progress on both of these fronts.

We have derived a novel metric for quantifying ultrasound image quality. Unlike traditional measures, such as the Rayleigh resolution, which quantify point target resolution, our metric quantifies the contrast of an anechoic cyst as a function of cyst radius. Cystic contrast is a much more relevant parameter for medical ultrasound where point targets are rare and of little clinical importance. Our paper describing this new metric was revised in April 2006 after receiving positive reviewer comments [16]. We expect this paper to be published before the end of 2007.

In the past year we have also developed two novel techniques for optimizing conventional beamformer performance. These techniques, termed Linear Constrained Least Squares (LCLS) and Quadratically Constrained Least Squares (QCLS) optimization both design optimal beamformer weights using slightly different mathematical criterion. LCLS minimizes the point spread function energy outside a given cyst radius while maintaining a constant gain at the center of the cyst. This technique yields a closed form solution that makes best use of the element responses, regardless of system non-idealities including limited element angular response and bandwidth. The second technique, QCLS, also minimizes the point spread function energy outside a given cyst radius, but constrains the energy within the cyst radius. This technique effectively optimizes the cystic contrast metric and therefore should optimize image quality. The theoretical underpinnings and simulation validation of these techniques are described in two papers submitted to IEEE Transactions on Ultrasonics, Ferroelectrics, and Frequency Control [17, 18].

**SPOC Progress:**

As stated above, our major research effort under this proposal has now focused on the refinement and validation of the SPOC algorithm. SPOC was first developed by Van Trees *et al.* for application in passive SONAR imaging. A similar approach has also been discussed by Malioutov *et al.* This algorithm, briefly described below, can be successfully applied to medical ultrasound data, with some significant algorithmic refinement.

The region of tissue to be imaged region (the region of interest or ROI), is subdivided into a collection of hypothetical targets at arbitrary positions, as shown in figure 2. Finer target placement yields finer final image resolution but entails higher computational costs. For each hypothetical target in the ROI, we model the signal received by the array for that specific point (i.e., the spatial responses). These spatial responses can be determined using a theoretical model, computational model, or can be extracted from experimental data. For every hypothetical target, the spatial impulse response is a matrix of dimensions TxN, where T is the number of samples in the time dimension and N is the number of elements in the array. After the spatial impulse responses for all the hypothetical targets have been calculated, these responses are reshaped to form an array manifold matrix $\underline{V}$ of dimensions NTxLP, where L and P are the numbers of hypothetical sources in the range and lateral dimensions, respectively. The observation model then becomes:

$$\underline{x} = \underline{V}\,\underline{f} \qquad\qquad\qquad\qquad (1)$$

where $\underline{x} = [\underline{x_1}\ \underline{x_2} \cdots\cdots \underline{x_N}]^T$ is the data received by the N-element array and $\underline{f}$ is the LPx1 target amplitude vector, whose elements are the amplitudes of the hypothetical targets located in the ROI. $\underline{x}$ is a NTx1 vector that is obtained by concatenating the Tx1 channel data $\underline{x_i}$. Given $\underline{x}$ and $\underline{V}$, SPOC matches the received data $\underline{x}$ to

the signal model to solve for the position and intensity of the real sources (i.e., the $\underline{f}$ vector). If there is no real source at a particular location within the ROI, then the element of $\underline{f}$ that corresponds to that location should be zero. Mathematically, this is accomplished by solving the following maximum a posteriori (MAP) optimization problem:

$$Cost \quad function: \quad \sum_{l=1}^{LP} \ln|f_l|^2$$

$$subject \quad to: \quad \underline{x} = \underline{V}\,\underline{f}$$

(2)

where $f_l$ are elements of $\underline{f}$. A solution for the MAP optimization problem is found using the following iterative procedure described by K. W. Lo.
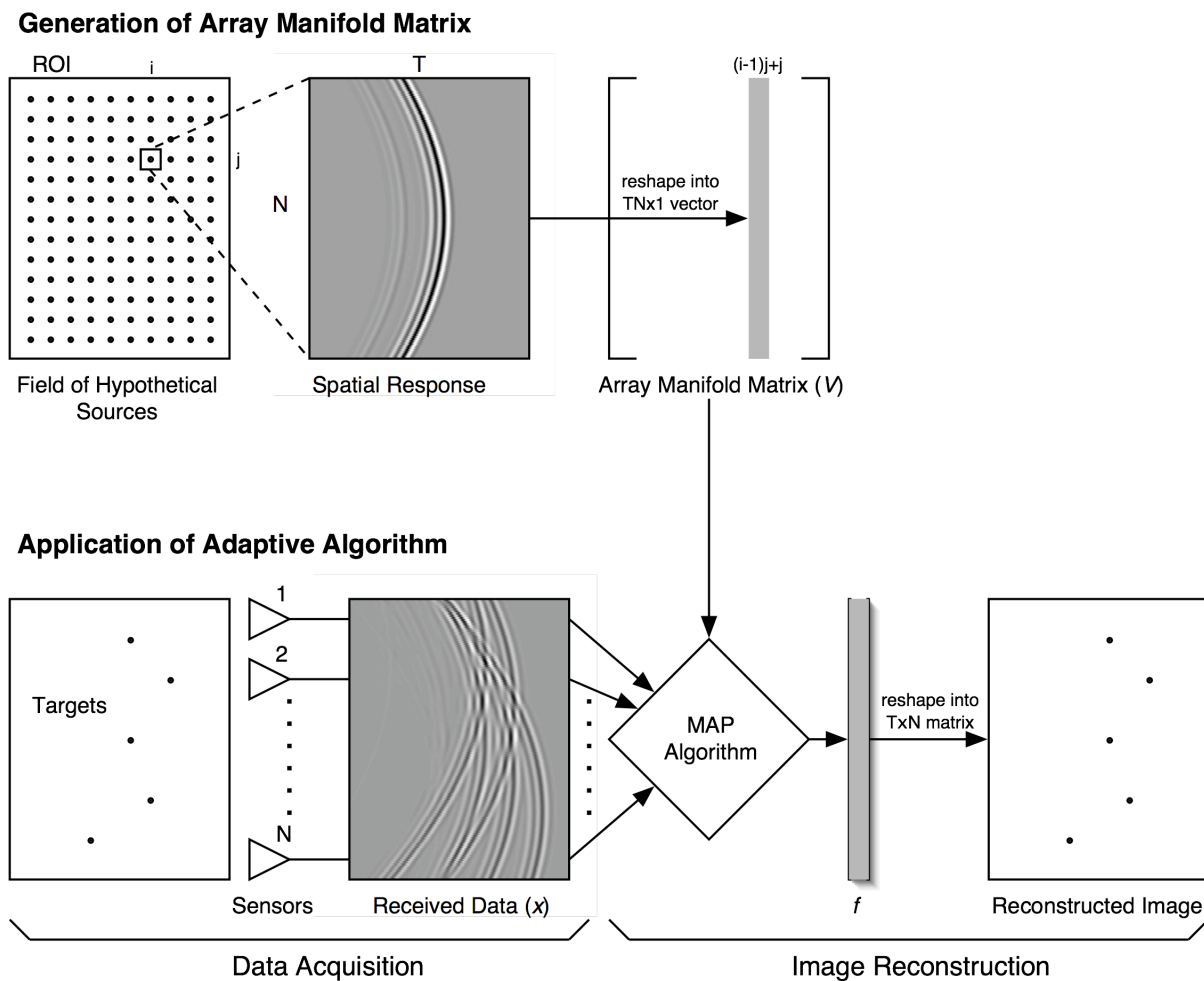


Figure 2. Schematic diagram of SPOC.

A series of computer simulations were performed in Matlab to test the potential of SPOC.

Single Point Target Simulations

A point target was placed directly in front of the transducer at a depth of 20.1mm. We simulated a 33 element linear array operating at 5 MHz with element spacing of 150μm. Signals were sampled at 40 MHz. Plane wave transmission was used for conventional beamforming and SPOC. Conventional beamforming was applied on the received RF data using Hann apodization and dynamic receive focusing. For SPOC, we discretized the image region as a setof hypothetical targets separated 20μm in range and 100μm in azimuth.
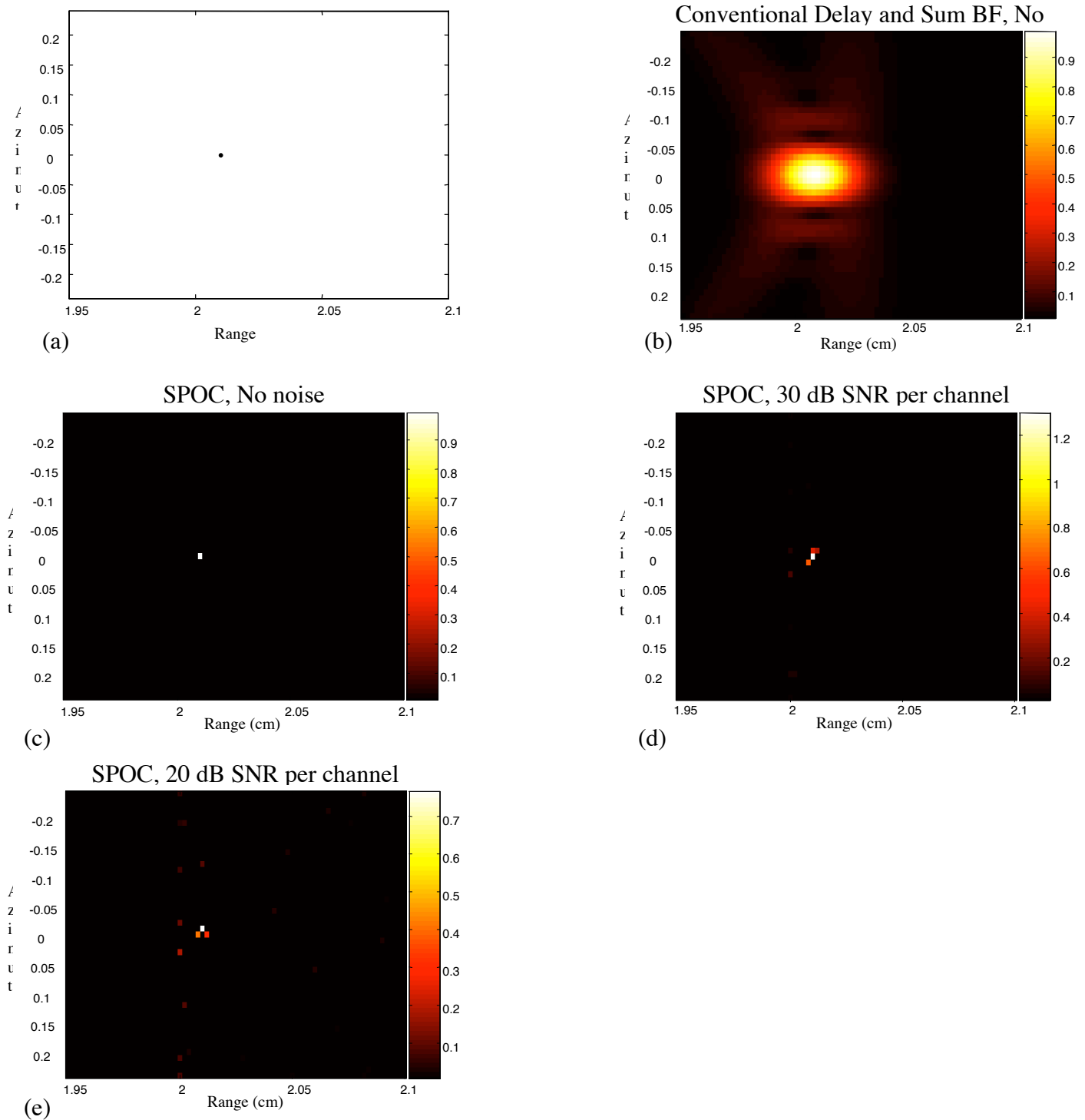


Figure 3. Point target simulations. The point target is depicted in (a); (b) shows conventional delay-and-sum beamforming, whereas images (c) to (e) show SPOC with different levels of electronic noise.

Multiple Point Target Simulations

A series of point targets were distributed within a 4x5mm region in range and azimuth, respectively. In this case, we simulated a 33 element linear array operating at 5 MHz with element spacing of 150μm. The final sampling frequency was set at 40 MHz. A plane wave was used on transmit for both conventional beamforming and SPOC. Conventional beamforming was applied on the received RF data using Hann apodization and dynamic receive focusing.

For SPOC, we discretized the image region in a set of hypothetical target locations separated 20μm in range and 120μm in azimuth. The positions of the points were chosen so that some, but not all coincide with the positions of the hypothetical targets. Results are encouraging in that they show SPOC is robust to differences between true target location and model target location.



(a)



Conventional Delay and Sum BF, No
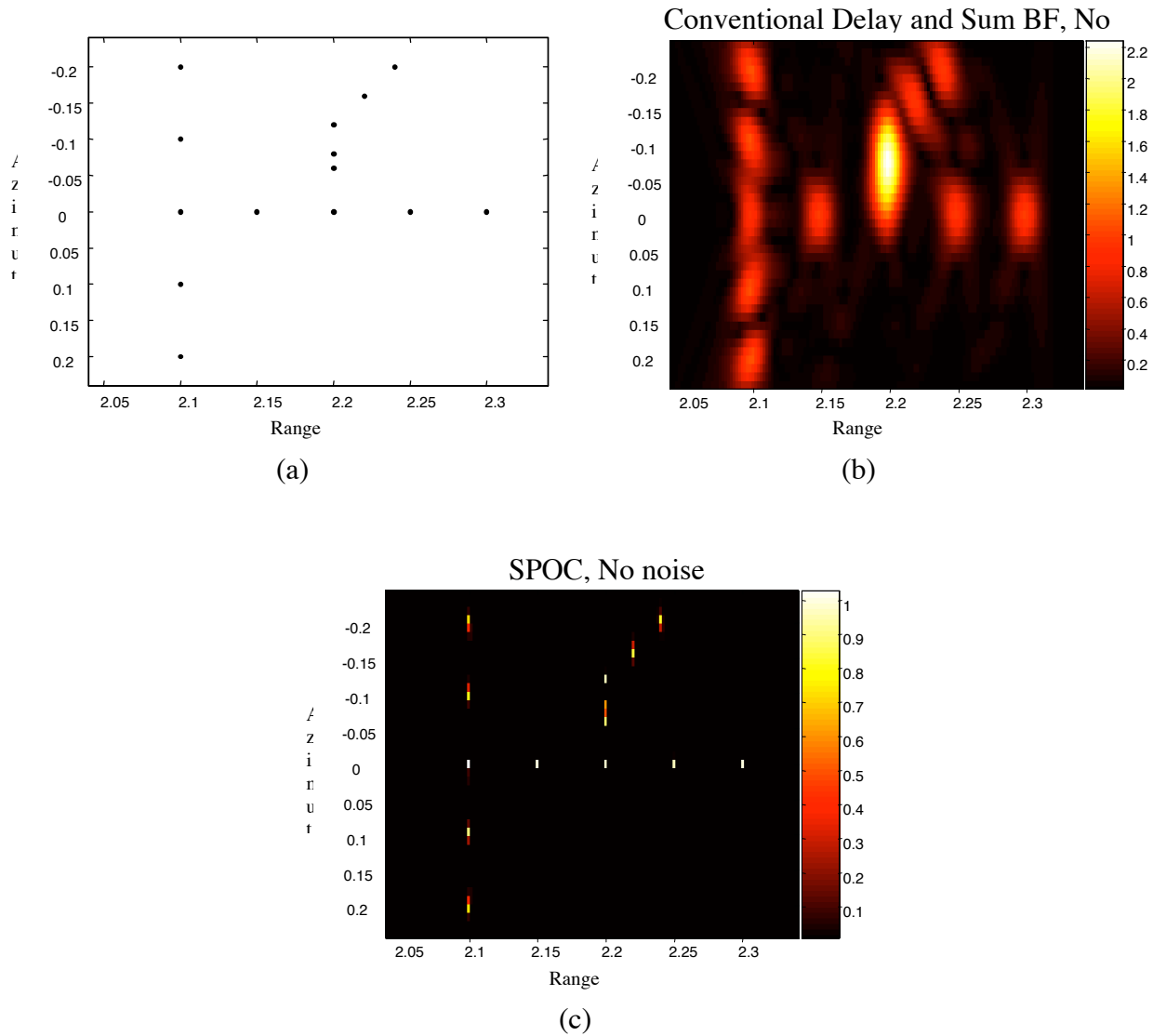
(b)



SPOC, No noise

(c)

Figure 4. Results obtained simulating a series of wire targets. The wires are depicted in (a); (b) shows conventional delay-and-sum beamforming, whereas (c) show SPOC.

Anechoic Cyst Simulation

A 1mm radius anechoic cyst was placed in front of the array and surrounded by ultrasonic scatterers randomly distributed within the image region. Scatterer amplitudes followed a Gaussian distribution with zero mean and standard deviation of one. Simulation methods are the same of those described in the previous section, except that the hypothetical source sampling was reduced to 100μm in azimuth. Again, the positions of the scatterers do not necessarily coincide with the position of the hypothetical sources. Results indicate that SPOC is robust in the presence of large numbers of targets placed at intervals closer than the conventional resolution.



(a)



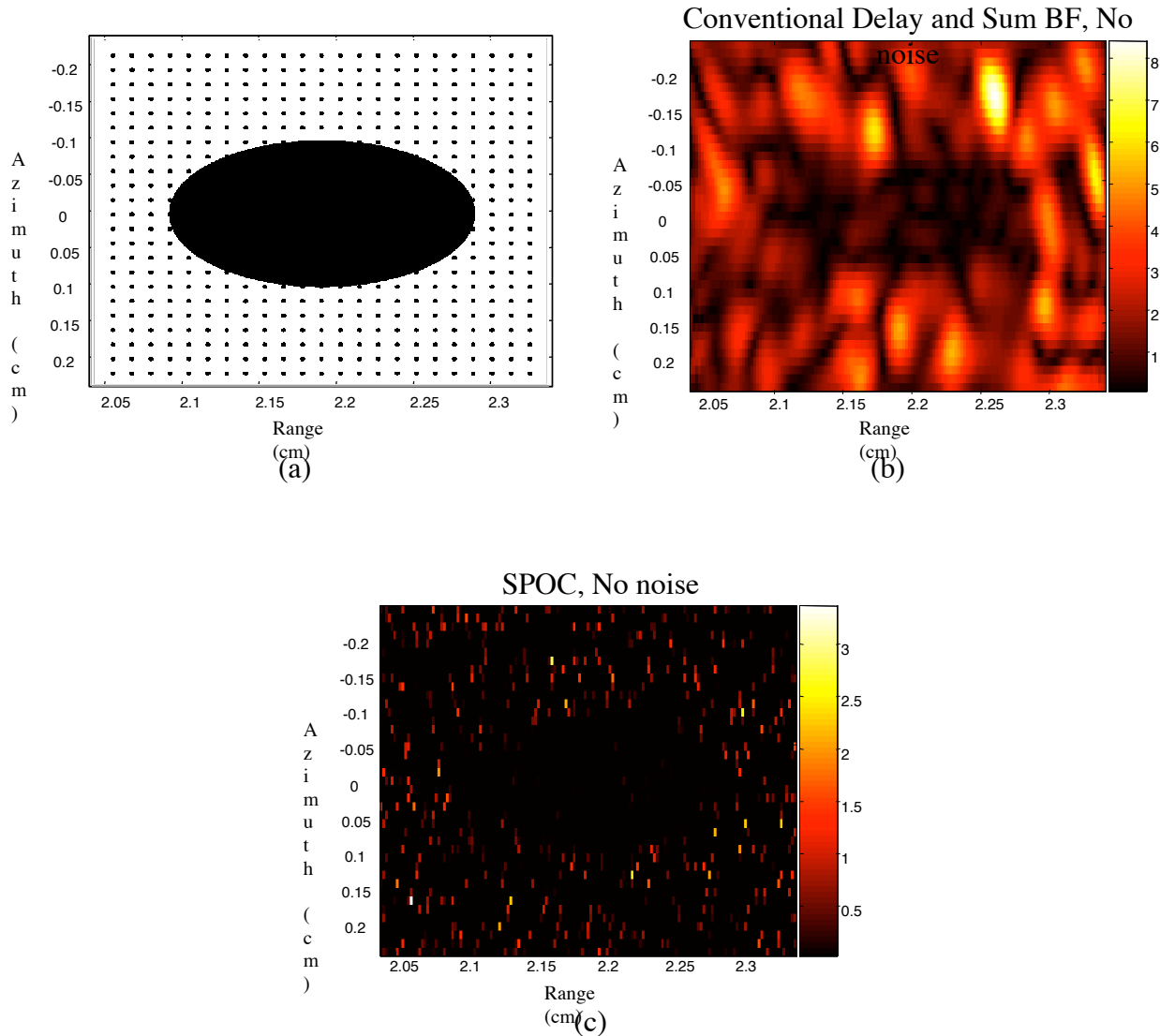Conventional Delay and Sum BF, No noise

(b)



SPOC, No noise

(c)

Figure 5. Results obtained simulating an anechoic cyst surrounded by scatterers. The cysts is depicted in (a); (b) shows conventional delay-and-sum beamforming, whereas (c) show SPOC.

Experimental results

We also performed a series of experiments using a commercially available Philips SONOS 5500 imaging scanner and a series of 5 wires suspended in a water tank. The wires are 20μm in diameter and spaced roughly 2mm apart. The top panel of figure 6 shows the image generated by the Philips scanner, whereas the bottom panel shows the SPOC reconstructed image. In the case of SPOC we discretized the image region in a

series of hypothetical targets separated by roughly 20μm in both range and azimuth. Results indicate that SPOC can perform robustly with real experimental data. Further work is ongoing to test SPOC in excised tissues.
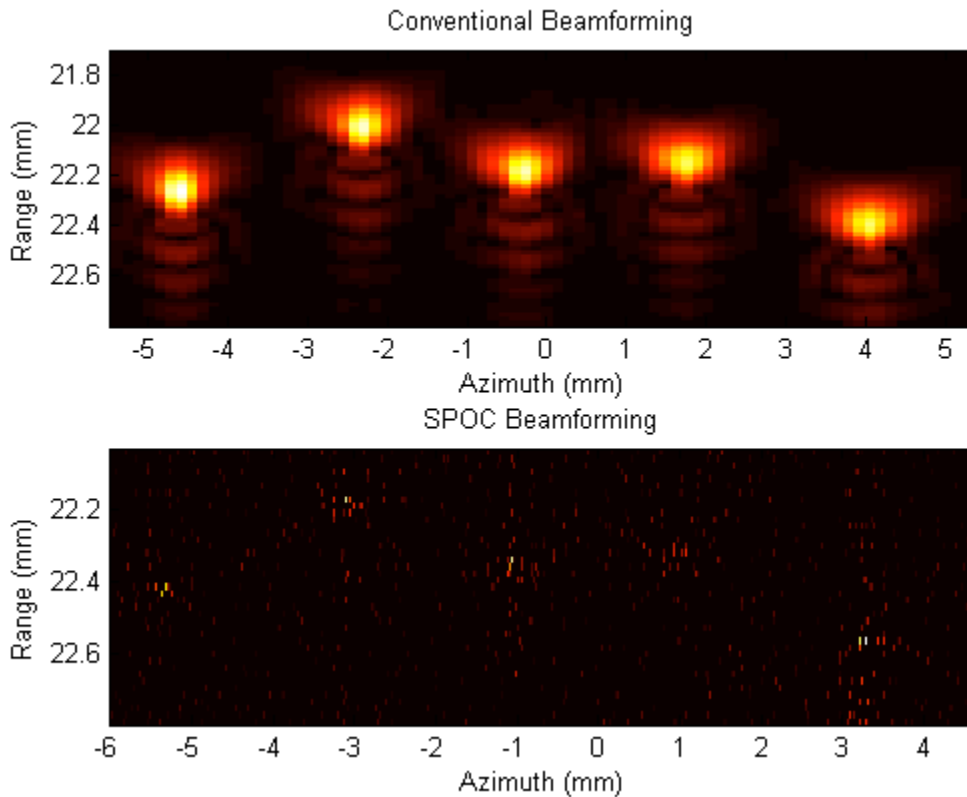


Figure 6. Comparison between conventional beamforming (top) and SPOC (bottom) on a set of 5 wires suspended within a water tank. The wires are 20μm in diameter.

**Simulation Tool Development:**
The performance of the SPOC algorithm depends greatly upon the quality of the system model it applies. In our initial simulations (presented above) we modeled the system using analytical methods, or using the well known FIELD program written by Jørgen Jensen. Unfortunately FIELD is quite slow when computing full 3D spatial impulse responses. Further, because FIELD works entirely on sampled data sets it is prone to artifacts from undersampling. We have implemented the Tupholme-Stepanishen method (the core approach used in FIELD) in a new piece of code we call DELFI. The DELFI code uses cubic spline representations of the transmitted pulse, and the transmit and receive spatial impulse responses. This approach avoids the potential sampling difficulties of FIELD. It is also significantly faster at computing space-space-space responses at an instant in time. These sort of responses are critical in much of our research and the 25 fold increase in speed for DELFI is of great significance. We have submitted a paper describing the algorithm and DELFI code last year[19]. While reviewer comments were positive, we concluded that a more detailed analysis was warranted because of the potential long-term significance of this code. We are now completing a revised version of the paper including just such an analysis. Early results are shown below in figure 7. Note that for space-space responses DELFI is significantly faster to achieve a given accuracy level. For space-time responses DELFI is somewhat slower, but can achieve high accuracy at significantly lower sampling rates. Once this paper is accepted for publication we will place the 1000 lines of DELFI source code on the Mathworks public access web site.
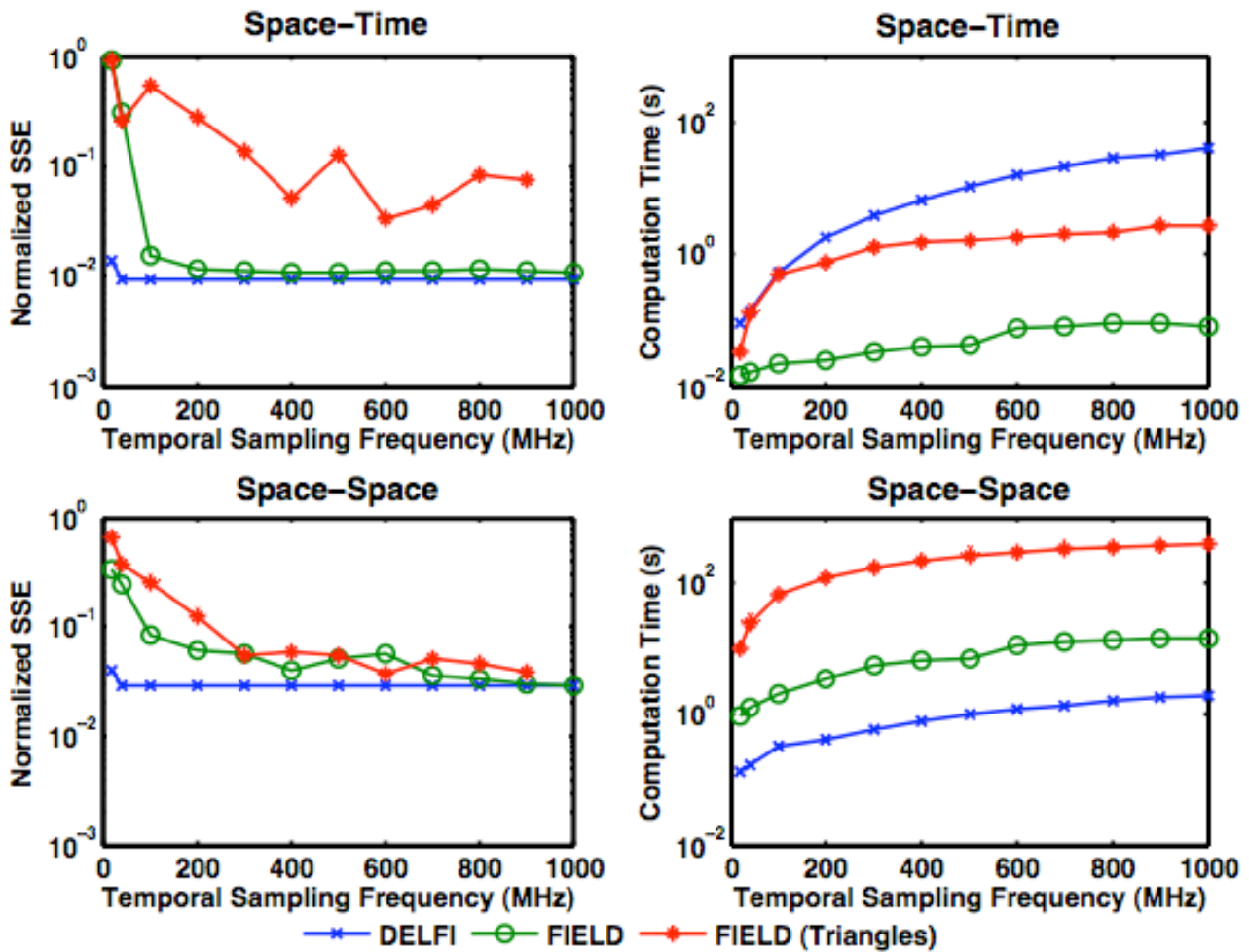
Figure 7: Simulation results comparing the speed and accuracy of DELFI and FIELD (both rectangular and triangular computational elements) for space-space and space-time responses. Note the high accuracy achieved for DELFI at even low sampling rates.

A limitation of the DELFI code is that it utilizes the same far-field approximation used by FIELD. This assumption requires intensive subsampling of the transducer array when the point of interest lies in the near-field of the transducer. We are currently refining the algorithm to be more accurate in the near-field. The modifications currently being explored would not have a significant impact on computational complexity. We anticipate completing and testing this refined algorithm in the coming year. We will submit a publication describing this work as it develops.

**Experimental Platform Development:**
In last year's progress report we described our efforts to harness the GE Logiq 700 MR, Philips SONOS 5500, and custom Sonic Window systems for data acquisition and clinical experimentation. At the same time we continued our efforts to modify the SONOS to enable parallel single channel acquisition. While some level of effort is ongoing in all of these platforms our major experimental platform is now built around the UltraSonix Sonix RP system.

The Sonix RP is a highly programmable research platform built around a clinical ultrasound imaging system. We acquired this system in June 2006 and have already implemented the following tools:

* Python scripting interface for Ultrasonix, to allow interactive control of all transmit/receive sequences without recompilation, for rapid experiment turnaround.
* Synthetic receive control - ability to receive single element RF data on successive transmits.
* Synthetic transmit control - ability to transmit on single elements.
* Automated full synthetic transmit/receive, this lets us capture full synthetic data sets from a 128-element transducer in 30 seconds.
* Automated transducer characterization in conjunction with hydrophone.
* Matlab interface for execution and analysis of simple sequences in a single script.

We are now working to quantify acoustic power output under a variety of operating conditions. These calibrations are a necessary precursor to clinical trials of angular scatter quantification and SPOC testing. We anticipate that this step will be completed in a matter of weeks. At the same time we are working on two additional system modifications:

* Automated averaging of repeatedly captured data to improve SNR.
* Full synthetic transmit/receive capture with improved SNR due to spatial encoding.

In just over a month we have dramatically modified the Sonix RP to make it one of the easiest to use and most programmable ultrasound research tools in the world. We look forward to applying this system aggressively in tissue and clinical studies in the next few months.

Another experimental system, not described in the original proposal, is a fully custom system developed in a collaboration with two other investigators at the University of Virginia (John A. Hossack and Travis N. Blalock.) A second generation of this system is already being assembled. This second generation system will utilize a 3600 element 2D array and will operate at a 5.0 MHz center frequency. Data from all channels will be acquired in parallel in real-time, however only four real samples will be acquired by each channel. Although the data acquisition of this system is certainly limited in some ways, we believe that this system will provide an excellent testbed for SPOC. In the coming months as this system becomes operational we will acquire data to test the viability of SPOC on 2D arrays.

**Corporate Interactions:**
Our work on SPOC has both great potential and great challenges. We have been assisted in these efforts through a number of valuable corporate interactions.

Our experimental work was originally aided through technical support and equipment donations from Philips Medical Systems. Our transition to the Sonix RP system has of course been supported by UltraSonix.

SPOC is extremely challenging to implement computationally and we are working closely with Interactive Supercomputing to test the algorithm. They have provided technical support to enable the transition of our algorithms to their Star-P MATLAB parallelization software. Interactive Supercomputing has also provided us with free CPU cycles on their high-end cluster.

One of the most exciting corporate collaborations in this project has been our ongoing interaction with InnerVision Medical Technologies. InnerVision is currently developing an ultrasound platform that has both the data acquisition capabilities and computational capabilities to implement SPOC clinically. The University of Virginia Patent Foundation is actively negotiating licensing terms with InnerVision and both sides have indicated that they expect to achieve a mutually agreeable conclusion in the next few months.

**Key Research Accomplishments:**
• Extensive simulation of SPOC for point and speckle targets (performance is quite robust)
• Experimental validation of SPOC for wire targets
• Implementation of SPOC in Star-P to speed execution and enable higher resolution
• Drafted paper for submission to Science (collecting further experimental data before submission)
• Drafted paper for submission to IEEE Transactions on Medical Imaging (awaiting response from Science)

• Developed a novel resolution metric for medical ultrasound
• Submitted paper describing resolution metric to IEEE-UFFC

• Developed two new methods for optimal apodization in conventional beamforming
• Submitted two papers describing optimal apodization to IEEE-UFFC

• Extensive testing of DELFI speed and accuracy
• Rewriting paper describing DELFI for IEEE-UFFC

• Acquisition of Sonix RP System
• Development of extensive tools for Sonix RP experimentation

• Initiated collaboration with Interactive Supercomputing
• Active licensing negotiation with InnerVision Medical Technologies

# Reportable Outcomes:

## Papers:

Ranganathan, K. and W.F. Walker, "A General Cystic Resolution Metric for Medical Ultrasound," revised for IEEE Trans. Ultrason. Ferroelec. Freq. Contr., Apr., 2006.

Guenther, D.A., and W.F. Walker, "Optimal Apodization Design for Medical Ultrasound using Constrained Least Squares. Part I: Theory," submitted to IEEE Trans. Ultrason. Ferroelec. Freq. Contr.

Guenther, D.A., and W.F. Walker, "Optimal Apodization Design for Medical Ultrasound using Constrained Least Squares. Part II: Results," submitted to for IEEE Trans. Ultrason. Ferroelec. Freq. Contr.

Walker, W.F., "A Spline Based Approach for Computing Spatial Impulse Responses," submitted to IEEE Trans. Ultrason. Ferroelec. Freq. Contr., Feb., 2005. (accepted with major revisions)

## Conference Abstracts:

Viola, F. and W.F. Walker, "Adaptive Signal Processing in Medical Ultrasound Beamforming," accepted to the 2005 IEEE Ultrasonics Symposium.

Viola, F., and W.F. Walker, "Adaptive Beamforming for Medical Ultrasound Imaging," U.S. Dept. of Defense Breast Cancer Research Program Era of Hope 2005 Meeting, June 2005.

## Patent Disclosures:

"Adaptive Beamformiong for Medical Ultrasound Imaging," F. Viola, and W.F. Walker, patent disclosure filed 2005.

## Software:

DELFI – A cubic spline based code for simulating spatial impulse responses. Currently over 1000 lines of C code.

**Conclusions:**

In our second year of funding we have moved aggressively to test the SPOC algorithm and to develop experimental and theoretical tools to fully validate this technique. We have worked closely with industrial partners to test this approach and to develop necessary tools. In the coming year we will begin testing in more realistic phantoms and *in vivo*.

**References:**

[1]      V. Jackson, "Management of solid breast nodules:  what is the role of sonography?," *Radiology*, vol. 196, pp. 14-15, 1995.

[2]      V. P. Jackson, "The Role of US in Breast Imaging," *Radiology*, vol. 177, pp. 305 - 311, 1990.

[3]      T. M. Kolb, J. Lichy, and J. H. Newhouse, "Comparison of the Performance of Screening Mammography, Physical Examination, and Breast US and Evaluation of Factors that Influence Them: An Analysis of 27,825 Patient Evaluations," *Radiology*, vol. 225, pp. 165-175, 2002.

[4]      M. O'Donnell and S. W. Flax, "Phase aberration correction using signals from point reflectors and diffuse scatters: measurements," *IEEE Trans. Ultrason. Ferroelec. Freq. Contr.*, vol. 35, pp. 768-774, 1988.

[5]      M. O'Donnell and S. W. Flax, "Phase aberration measurements in medical ultrasound: human studies," *Ultrasonic Imaging*, vol. 10, pp. 1-11, 1988.

[6]      L. Nock, G. E. Trahey, and S. W. Smith, "Phase aberration correction in medical ultrasound using speckle brightness as a quality factor," *JASA*, vol. 85, pp. 1819-1833, 1989.

[7]      S. Krishnan, P.-C. Li, and M. O'Donnell, "Adaptive Compensation of Phase and Magnitude Aberrations," *IEEE Transactions on Ultrasonics Ferroelectrics & Frequency Control*, vol. 43, pp. 44-55, 1996.

[8]      L. M. Hinkelman, D.-L. Liu, R. C. Waag, Q. Zhu, and B. D. Steinberg, "Measurement and correction of ultrasonic pulse distortion produced by the human breast.," *Journal of the Acoustical Society of America*, vol. 97:3, pp. 1958-1969, 1995.

[9]      G. Ng, P. D. Freiburger, W. F. Walker, and G. E. Trahey, "A technique for adaptive imaging in the presence of distributed aberrations," presented at IEEE Ultrasonics Symposium, Seattle, Washington, 1995.

[10]    Q. Zhu and B. D. Steinberg, "Correction of multipath interference using clean and spatial location diversity," presented at IEEE International Ultrasonics Symposium, Seattle, Washington, 1995.

[11]    K. Rigby, E. Andarawis, C. Chalek, B. Haider, W. Hinrichs, R. Hogel, W. Leue, M. Angle, B. McEathron, S. Miller, S. Peshman, M. Peters, L. Thomas, S. Krishnan, and M. O'Donnell, "Realtime Adaptive Imaging," presented at IEEE Ultrasonic Symposium, 1998.

[12]    K. Rigby, C. Chalek, B. Haider, R. Lewandowski, M. O'Donnell, L. Smith, and D. Wildes, "Improved in vivo Abdominal Image Quality Using Real-Time Estimation and Correction of Wavefront Arrival Time Errors," presented at IEEE Ultrasonics Symposium, 2000.

[13]    R. Gauss and G. Trahey, "Wavefront Estimation in the Human Breast," presented at SPIE Medical Imaging, 2001.

[14]    J. A. Mann and W. F. Walker, "Constrained Adaptive Beamforming: Point and Contrast Resolution," presented at SPIE Medical Imaging Symposium, 2003.

[15]    J. A. Mann and W. F. Walker, "A Constrained Adaptive Beamformer for Medical Ultrasound: Initial Results," presented at Proc. IEEE Ultrason. Symp., 2002.

[16]    K. Ranganathan and W. F. Walker, "A General Cystic Resolution Metric for Medical Ultrasound," *IEEE Transactions on Ultrasonics Ferroelectrics & Frequency Control*, in revision 2006.

[17]    D. A. Guenther and W. F. Walker, "Optimal Apodization Design for Medical Ultrasound using Constrained Least Squares. Part II: Results," *IEEE Transactions on Ultrasonics Ferroelectrics & Frequency Control*, submitted 2006.

[18]    D. A. Guenther and W. F. Walker, "Optimal Apodization Design for Medical Ultrasound using Constrained Least Squares. Part I: Theory," *IEEE Transactions on Ultrasonics Ferroelectrics & Frequency Control*, submitted 2006.

[19]    W. F. Walker, "A Spline Based Approach for Computing Spatial Impulse Responses," *IEEE Transactions on Ultrasonics Ferroelectrics & Frequency Control*, submitted.

**A General Cystic Resolution Metric for Medical Ultrasound**

Karthik Ranganathan[1] and William F. Walker[1, 2]


[1]Biomedical Engineering, University of Virginia, Charlottesville, VA 22908

[2]Electrical and Computer Engineering, University of Virginia, Charlottesville, VA 22904

**Abstract:**

This paper describes a metric that can be used to characterize the resolution of arbitrary, broadband, coherent imaging systems. The metric is particularly suited to medical ultrasound because it characterizes scanner performance using the contrast obtained by imaging anechoic cysts of various sizes that are embedded in a speckle generating background, accounting for the effect of electronic noise. We present the theoretical derivation of the metric and provide simulation examples that demonstrate its utility. We utilize the metric to compare a low-cost, handheld, C-scan system under development in our laboratory to conventional ultrasound scanners. We also present the results of simulations that were designed to evaluate and optimize various parameters in our system, including the f/# and apodization windows. We investigate the impact of electronic noise on our system and quantify the tradeoffs associated with quantization in the analog to digital converter. Results indicate that an f/1 receive aperture combined with 10 bit precision and an SNR of 0 dB per channel would result in adequate image quality.

# I. INTRODUCTION

The evaluation of imaging performance is an essential task in the development of ultrasound systems, both to predict fundamental limits on quality and to optimize parameters for system design. It is possible to estimate the performance of existing systems by imaging phantoms or human subjects, but during system design, it is necessary to be able to determine imaging performance of a proposed system prior to construction. The ability to accurately predict performance enables system optimization and quantitative consideration of engineering tradeoffs early in the design process and significantly reduces the time and cost investment in system development. To support these goals, this paper develops a general resolution metric for comparing arbitrary imaging systems.

The most common metric used to estimate scanner performance is the beamplot, which has been adapted from RADAR. System resolution is usually described using a combination of the full width at half maximum (FWHM) or -6 dB beamwidth of the beamplot and the beamwidth at other levels [1]. Sidelobe and grating lobe levels are used to estimate eventual image contrast. Although widely used, there are disadvantages to using the beamplot to estimate the performance of ultrasound systems. Targets in medical ultrasound are usually weakly reflecting tissues in a scattering medium, unlike RADAR targets that are more often highly reflective and in a non-scattering background. Therefore, there may be scenarios in which the FWHM criterion indicates excellent performance, but actual images of tissue do not reveal important details. Vilkomerson et al [2] demonstrated that the FWHM criterion sometimes provides misleading information about resolution in ultrasound systems. It is, in addition,

difficult to be certain about the best levels at which to characterize and optimize the beamplot. In other words, it is difficult to decide whether to optimize the mainlobe width or sidelobe and grating lobe levels for an overall increase in image quality. As mentioned above, performance may be determined by imaging phantoms; however, this does not provide a way to theoretically assess the performance of different hypothetical imaging systems. While repeated image simulations could be performed to assess a wide variety of system parameters, including resolution, this approach is very computationally challenging. We need a metric that ties together resolution and contrast in a way that is relevant to diagnostic ultrasound imaging.

Vilkomerson et al addressed the limitations of the beamplot and proposed the concept of "cystic resolution" [2] in which performance was quantified as the size of a void that produced a given contrast. The analysis, while novel and useful, was limited to narrowband circular apertures and neglected the axial dimension. Üstüner et al [3] extended cystic resolution to a 3D broadband model that addressed the above problems but did not describe its theoretical foundation or publish the model in an archival journal. The lack of a theoretical background in [3] obscures important details, resulting in a limited understanding of the formulation and its utility and drawbacks. We derive a metric identical to that in [3], extend it to include the effects of electronic noise, and present simulation results that demonstrate its utility.

## II. THEORY

Our goal is to derive a metric to quantify the contrast resolution of an arbitrary broadband ultrasound system. Let the point spread function (psf) of the ultrasound system be defined as

$\boxed{\times}$, a function of three-dimensional (3D) space ($\vec{x}$) and time ($t$). Time in this expression is included for the propagation of the sensitivity function through the tissue and thus typically begins at transmission and ends at the completion of a single echo line. The medium scattering function is modeled as a stochastic process $N(\vec{x})$, undergoing negligible tissue motion during reception of an individual echo line and therefore being constant with time. We assume that the effect of electronic noise during transmit is negligible due to the high signal to noise ratio (SNR) on transmit, and model the electronic noise on receive as another stochastic process $E(t)$. Combining these factors, and assuming that the electronic noise is purely additive, the received signal as a function of time is

$$S_b(t) = \int_{-\infty}^{\infty} P(\vec{x},t)\, N(\vec{x})\, d\vec{x} + E(t) \tag{1}$$

Consider the mean squared received signal $\langle S_b^2(t)\rangle$ where $\langle\ \rangle$ is the expected value operator:

$$\langle S_b^2(t)\rangle = \left\langle \left[\int_{-\infty}^{\infty} P(\vec{x}_1,t)N(\vec{x}_1)d\vec{x}_1 + E(t)\right]\left[\int_{-\infty}^{\infty} P(\vec{x}_2,t)N(\vec{x}_2)d\vec{x}_2 + E(t)\right]\right\rangle. \tag{2}$$

$$\langle S_b^2(t)\rangle = \left\langle \int_{-\infty}^{\infty}\int_{-\infty}^{\infty} P(\vec{x}_1,t)P(\vec{x}_2,t)N(\vec{x}_1)N(\vec{x}_2)d\vec{x}_1\, d\vec{x}_2 \right\rangle$$

$$+ \left\langle \int_{-\infty}^{\infty}\int_{-\infty}^{\infty} P(\vec{x}_1,t)N(\vec{x}_1)E(t)d\vec{x}_1 \right\rangle$$

$$+\left\langle \int_{-\infty}^{\infty}\int_{-\infty}^{\infty} P(\vec{x}_2,t)N(\vec{x}_2)E(t)d\vec{x}_2 \right\rangle + \left\langle E^2(t) \right\rangle \tag{3}$$

Rearranging the expected value operator to account for the fact that the scattering function and electronic noise are stochastic but the psf is deterministic yields:

$$\left\langle S_b^2(t) \right\rangle = \int_{-\infty}^{\infty}\int_{-\infty}^{\infty} P(\vec{x}_1,t)P(\vec{x}_2,t)\left\langle N(\vec{x}_1)N(\vec{x}_2) \right\rangle d\vec{x}_1\,d\vec{x}_2$$

$$+ \int_{-\infty}^{\infty}\int_{-\infty}^{\infty} P(\vec{x}_1,t)\left\langle N(\vec{x}_1)E(t) \right\rangle d\vec{x}_1$$

$$+ \int_{-\infty}^{\infty}\int_{-\infty}^{\infty} P(\vec{x}_2,t)\left\langle N(\vec{x}_2)E(t) \right\rangle d\vec{x}_2 + \left\langle E^2(t) \right\rangle \tag{4}$$

We assume that the electronic noise $E(t)$ and the scattering function $\boxed{\times}$ are uncorrelated and obtain:

$$\left\langle S_b^2(t) \right\rangle = \int_{-\infty}^{\infty}\int_{-\infty}^{\infty} P(\vec{x}_1,t)P(\vec{x}_2,t)\left\langle N(\vec{x}_1)N(\vec{x}_2) \right\rangle d\vec{x}_1\,d\vec{x}_2 + \left\langle E^2(t) \right\rangle \tag{5}$$

This expression can be further simplified by assuming that the target scattering function is a stationary, white noise process whose autocorrelation is a delta function. Applying this assumption yields:

$$\left\langle S_b^2(t) \right\rangle = \int\limits_{-\infty}^{\infty} \int\limits_{-\infty}^{\infty} P(\vec{x}_1, t) P(\vec{x}_2, t) a \delta(\vec{x}_1 - \vec{x}_2, t) d\vec{x}_1 \, d\vec{x}_2 + \left\langle E^2(t) \right\rangle$$

(6)

where $a$ is a scaling factor. Performing the outermost integral in the first term yields:

$$\left\langle S_b^2(t) \right\rangle = a \int\limits_{-\infty}^{\infty} P^2(\vec{x}, t) d\vec{x} + \left\langle E^2(t) \right\rangle \qquad (7)$$

The mean squared received signal is therefore a function of only the 3D psf and the electronic noise. We can now describe a mask that defines the location and size of a spherical anechoic void (cyst):

$$\begin{aligned} M(\vec{x}) &= 0, \; |\vec{x}| \le R \\ &= 1, \; |\vec{x}| > R, \end{aligned} \qquad (8)$$

where $R$ is the radius of the cyst and the cyst center is at the origin of the coordinate system. $M(\vec{x})$ is also independent of time since we assume no tissue motion during the acquisition.

The scattering medium with the void is represented as $N(\vec{x})M(\vec{x})$. The received signal energy is expected to be at a minimum when the beam axis coincides with the center of the void and as much of the psf energy as possible lies in the region defined by the void. The received signal in this circumstance can then be written as:

$$S_c(t) = \int_{-\infty}^{\infty} P(\vec{x},t) N(\vec{x}) M(\vec{x}) d\vec{x} + E(t) \qquad (9)$$

The mean squared received signal $\langle S_c^2(t) \rangle$ is:

$$\langle S_c^2(t) \rangle = \left\langle \left[ \int_{-\infty}^{\infty} P(\vec{x}_1,t) N(\vec{x}_1) M(\vec{x}_1) d\vec{x}_1 + E(t) \right] \right.$$

$$\left. \cdot \left[ \int_{-\infty}^{\infty} P(\vec{x}_2,t) N(\vec{x}_2) M(\vec{x}_2) d\vec{x}_2 + E(t) \right] \right\rangle \qquad (10)$$

$$\langle S_c^2(t) \rangle = \left\langle \int_{-\infty}^{\infty} \int_{-\infty}^{\infty} P(\vec{x}_1,t) P(\vec{x}_2,t) N(\vec{x}_1) N(\vec{x}_2) M(\vec{x}_1) M(\vec{x}_2) d\vec{x}_1 \, d\vec{x}_2 \right\rangle$$

$$+ \left\langle \int_{-\infty}^{\infty} \int_{-\infty}^{\infty} P(\vec{x}_1,t) N(\vec{x}_1) M(\vec{x}_1) E(t) d\vec{x}_1 \right\rangle$$

$$+ \left\langle \int_{-\infty}^{\infty} \int_{-\infty}^{\infty} P(\vec{x}_2,t) N(\vec{x}_2) M(\vec{x}_2) E(t) d\vec{x}_2 \right\rangle + \left\langle E^2(t) \right\rangle \qquad (11)$$

Since the psf and the mask are deterministic:

$$\langle S_c^2(t) \rangle = \int_{-\infty}^{\infty} \int_{-\infty}^{\infty} P(\vec{x}_1,t) P(\vec{x}_2,t) M(\vec{x}_1) M(\vec{x}_2) \left\langle N(\vec{x}_1) N(\vec{x}_2) \right\rangle d\vec{x}_1 \, d\vec{x}_2$$

$$+ \int_{-\infty}^{\infty} \int_{-\infty}^{\infty} P(\vec{x}_1,t) M(\vec{x}_1) \left\langle N(\vec{x}_1) E(t) \right\rangle d\vec{x}_1$$

$$+ \int_{-\infty}^{\infty}\int_{-\infty}^{\infty} P(\vec{x}_2,t)M(\vec{x}_2)\langle N(\vec{x}_2)E(t)\rangle d\vec{x}_2 + \langle E^2(t)\rangle \tag{12}$$

Once again, assuming $N(\vec{x})$ is a stationary white noise process and uncorrelated to $E(t)$, we get:

$$\langle S_c^2(t)\rangle = \int_{-\infty}^{\infty}\int_{-\infty}^{\infty} P(\vec{x}_1,t)P(\vec{x}_2,t)M(\vec{x}_1)M(\vec{x}_2)a\delta(\vec{x}_1 - \vec{x}_2,t)d\vec{x}_1\, d\vec{x}_2 + \langle E^2(t)\rangle \tag{13}$$

$$\langle S_c^2(t)\rangle = a\int_{-\infty}^{\infty} P^2(\vec{x},t)M^2(\vec{x})d\vec{x} + \langle E^2(t)\rangle \tag{14}$$

The contrast of the cyst can then be defined as:

$$C(t) = \sqrt{\frac{\langle S_c^2(t)\rangle}{\langle S_b^2(t)\rangle}} = \sqrt{\frac{a\int_{-\infty}^{\infty} P^2(\vec{x},t)M^2(\vec{x})d\vec{x} + \langle E^2(t)\rangle}{a\int_{-\infty}^{\infty} P^2(\vec{x},t)d\vec{x} + \langle E^2(t)\rangle}} \tag{15}$$

We define the electronic SNR as a function of time:

$$SNR(t) = \frac{\sigma_{signal}(t)}{\sigma_{noise}(t)} \tag{16}$$

where $\sigma_{signal}(t)$ and $\sigma_{noise}(t)$ are the standard deviations of the signal and noise components respectively. Note that we define the standard deviations over an ensemble of signal and noise realizations and not in time. $\sigma_{signal}(t)$ can be expressed as:

$$\sigma_{signal}(t) = \sqrt{\left\langle \int_{-\infty}^{\infty} P(\vec{x}_1,t)N(\vec{x}_1)d\vec{x}_1 \int_{-\infty}^{\infty} P(\vec{x}_2,t)N(\vec{x}_2)d\vec{x}_2 \right\rangle} \tag{17}$$

$$\sigma_{signal}(t) = \sqrt{a \int_{-\infty}^{\infty} P^2(\vec{x},t)d\vec{x}} \tag{18}$$

$\sigma_{noise}(t)$ can be expressed as:

$$\sigma_{noise}(t) = \sqrt{\left\langle E^2(t) \right\rangle} \tag{19}$$

Applying (18) and (19) to (16) yields:

$$SNR(t) = \frac{\sigma_{signal}(t)}{\sigma_{noise}(t)} = \sqrt{\frac{a \int_{-\infty}^{\infty} P^2(\vec{x},t)d\vec{x}}{\left\langle E^2(t) \right\rangle}} \tag{20}$$

or equivalently

$$\left\langle E^{2}(t)\right\rangle = \frac{a\int\limits_{-\infty}^{\infty} P^{2}(\vec{x},t)d\vec{x}}{SNR^{2}(t)} \qquad (21)$$

Applying (21), (15) can now be modified to yield:

$$C(t) = \sqrt{\frac{a\int\limits_{-\infty}^{\infty} P^{2}(\vec{x},t)M^{2}(\vec{x})d\vec{x} + \dfrac{a\int\limits_{-\infty}^{\infty} P^{2}(\vec{x},t)d\vec{x}}{SNR^{2}(t)}}{a\int\limits_{-\infty}^{\infty} P^{2}(\vec{x},t)d\vec{x} + \dfrac{a\int\limits_{-\infty}^{\infty} P^{2}(\vec{x},t)d\vec{x}}{SNR^{2}(t)}}} \qquad (22)$$

We can simplify the expression in (22) as follows:

$$C(t) = \sqrt{\frac{SNR^{2}(t)\int\limits_{-\infty}^{\infty} P^{2}(\vec{x},t)M^{2}(\vec{x})d\vec{x} + \int\limits_{-\infty}^{\infty} P^{2}(\vec{x},t)d\vec{x}}{SNR^{2}(t)\int\limits_{-\infty}^{\infty} P^{2}(\vec{x},t)d\vec{x} + \int\limits_{-\infty}^{\infty} P^{2}(\vec{x},t)d\vec{x}}} \qquad (23)$$

$$= \sqrt{\frac{1 + SNR^{2}(t)\dfrac{\int\limits_{-\infty}^{\infty} P^{2}(\vec{x},t)M^{2}(\vec{x})d\vec{x}}{\int\limits_{-\infty}^{\infty} P^{2}(\vec{x},t)d\vec{x}}}{1 + SNR^{2}(t)}} \qquad (24)$$

$$= \sqrt{\frac{1 + SNR^2(t)\dfrac{E^{out}(t)}{E^{tot}(t)}}{1 + SNR^2(t)}} \quad (25)$$

where $E^{out}(t)$ is the psf energy outside the void as a function of time:

$$E^{out}(t) = \int_{-\infty}^{\infty} P^2(\vec{x}, t) M^2(\vec{x}) d\vec{x} \quad (26)$$

and $E^{tot}(t)$ is the total psf energy as a function of time:

$$E^{tot}(t) = \int_{-\infty}^{\infty} P^2(\vec{x}, t) d\vec{x} \quad (27)$$

Equations (24) and (25) describe the contrast relative to background speckle obtained by an imaging system with the psf $P(\vec{x}, t)$ and electronic SNR defined statistically by $SNR(t)$, when imaging an anechoic cyst whose size and location are described by the mask $M(\vec{x})$. Equation (25) can alternatively be expressed as a function of the psf energy within the cyst, $E^{in}(t)$, given by:

$$E^{in}(t) = E^{tot}(t) - E^{out}(t) \quad (28)$$

Modifying (25):

$$C(t) = \sqrt{\dfrac{1 + SNR^2(t)\left(1 - \dfrac{E^{tot}(t) - E^{out}(t)}{E^{tot}(t)}\right)}{1 + SNR^2(t)}}$$

(29)

Substituting (28) in (29) yields:

$$C(t) = \sqrt{\dfrac{1 + SNR^2(t)\left(1 - \dfrac{E^{in}(t)}{E^{tot}(t)}\right)}{1 + SNR^2(t)}}$$

(30)

Note that if the cyst is large enough so that the entire psf energy is contained within the cyst, the contrast depends solely on the electronic noise. While (24), (25), and (30) can individually completely characterize system performance for a given cyst, analysis at the instant in time when the received signal is minimum (i.e. when as much of the psf energy as possible lies within the cyst) is usually sufficient. At this single instant in time $t_o$, we can express the psf as a function of only 3D space at the time of interest $P_{t_o}(\vec{x})$, and the SNR also at the time of interest $SNR_{t_o}$. Modifying (24), the contrast at time $t_o$ is:

$$C_{t_o} = \sqrt{\dfrac{1 + SNR_{t_o}^2 \dfrac{\displaystyle\int_{-\infty}^{\infty} P_{t_o}^2(\vec{x}) M^2(\vec{x}) d\vec{x}}{\displaystyle\int_{-\infty}^{\infty} P_{t_o}^2(\vec{x}) d\vec{x}}}{1 + SNR_{t_o}^2}}$$

(31)

$$= \sqrt{\frac{1 + SNR_{t_o}^2 \dfrac{E_{t_o}^{out}}{E_{t_o}^{tot}}}{1 + SNR_{t_o}^2}} \tag{32}$$

where $E_{t_o}^{out}$ is the psf energy outside the cyst and $E_{t_o}^{tot}$ is the total psf energy, both at time $t_o$.

Equation (32) can also be modified to express the contrast as a function of the psf energy within

the cyst at time $t_o$, $E_{t_o}^{in}$.

$$C_{t_o} = \sqrt{\frac{1 + SNR_{t_o}^2 \left(1 - \dfrac{E_{t_o}^{in}}{E_{t_o}^{tot}}\right)}{1 + SNR_{t_o}^2}} \tag{33}$$

If we neglect electronic noise, $SNR_{t_o}$ becomes infinite and (31) can be modified to the

equation for contrast presented in [3]:

$$C_{t_o} = \sqrt{\frac{\displaystyle\int_{-\infty}^{\infty} P_{t_o}^2(\vec{x}) M^2(\vec{x}) d\vec{x}}{\displaystyle\int_{-\infty}^{\infty} P_{t_o}^2(\vec{x}) d\vec{x}}} = \sqrt{\frac{E_{t_o}^{out}}{E_{t_o}^{tot}}} = \sqrt{1 - \frac{E_{t_o}^{in}}{E_{t_o}^{tot}}} \tag{34}$$

We can compute the contrast for cysts of different sizes using one of the above

expressions for cystic contrast, and characterize system performance as a function of cyst size as

in [2] and [3]. This metric can be used for 4D spatiotemporal analysis of arbitrary broadband

ultrasound systems, but 3D spatial analysis using (31) or (34) is adequate to characterize scanner performance as temporal analysis does not provide critical information. Note that in certain cases, it is valuable to compute the metric for different cyst locations to quantify depth of field, the effect of dynamic focusing, and other factors pertaining to the shift variance of the imaging system. Note also that while (24), (31), and (34) can be used to determine cystic resolution, we can also optimize system parameters by computing contrast as a function of cyst size and determining parameter values that maximize the contrast at the cyst sizes of interest.

## III. METHODS

The derived metric is useful for guiding the design and optimization of ultrasound systems. We highlight these applications through a series of examples drawn from our ongoing efforts to develop a low cost, handheld, C-scan ultrasound system for use in routine procedures such as image guided needle/IV line insertion and emergency room/battlefield triage. Our system utilizes a fully sampled 2D array [4] interfaced to a custom integrated circuit with transmit protection, analog conditioning, and sampling and digitizing circuitry [5]. Beamforming is implemented by complex phase rotation of I/Q data that are generated by directly sampling the received radiofrequency (RF) signal [6]. Our beamforming strategy, direct sampled I/Q (DSIQ) beamforming, results in poorer image quality than might be obtained using time delays; however, the use of a fully sampled 2D array enables dynamic focusing in elevation, which may outweigh the performance loss incurred by using DSIQ beamforming. In order to investigate such tradeoffs, we compared our current first generation prototype system to a conventional system with a 1D array that focused in azimuth using time delays and in elevation with a lens.

The conventional system had a 128 element 1D array with a pitch of 135 μm, while default parameters for our prototype system are listed in table 1. Our system does not have the ability to focus or apodize on transmit, so we focused and apodized only on receive in both sets of simulations. Receive apodization was implemented with 1D and 2D Nuttall windows [7]. We simulated our system using DELFI [8], a custom ultrasound simulation package. Spatial pulse-echo responses were computed by transmitting a plane wave on all elements and receiving sequentially on each element. The psfs were computed in the 3D cylindrical volume described in table 1 at two times - the time taken to propagate to the focus and back to the transducer, and a quarter period (at the center frequency) later [6]. We then combined the two psfs computed for each receive element to form a single complex psf [6]. We implemented apodization and focusing by complex phase rotation, and summed across elements to obtain the complete summed and focused response. Note that our first generation system differs significantly from the final system we envision. The final system will have a much larger element count and smaller pitch. We will likely focus using a modified version of DSIQ beamforming to avoid focusing problems due to phase wraparound. The current prototype does not have sampling and digitizing circuitry, and we also intend to improve the analog conditioning circuitry.

We used FIELD II [9] to simulate the conventional system by computing the spatiotemporal response at each point in the 3D spatial window of analysis. We applied the Hilbert transform [10] to form a complex analytic signal whose real part was the original received response and whose imaginary part was the Hilbert transform of that response. The 3D spatial psf was constructed by summing the samples at the two-way propagation time determined by array geometry and the location of the focus. Since the conventional system uses a lens in

elevation and since significant portions of targets are often imaged away from the elevation focus, we computed two psfs to compare to our system, one with the elevation focus coincident with the azimuthal focus at 1 cm, and one with the elevation focus set to 2.8 cm. Figure 1 shows slices of the two psfs obtained with the 1D array and focusing via time delays. Figure 2 shows slices of the psf obtained with the 2D array and DSIQ beamforming. We used (34) to compute the contrast for cysts of different sizes. We ignored the effects of electronic noise because noise estimates for our first generation prototype will be of limited relevance in our final system. Figure 3 depicts the contrast as a function of cyst size for the three geometries examined.

The above application of the metric allows direct comparison between our C-scan system and more conventional linear array based systems; a comparison which would be difficult using only the beamplot or even the psf. We have also applied the metric to quantify the often subtle differences in performance that result from changes in our system configuration. In each of the following examples, application of the metric provides a clear guidance in system design.

Although lower electronic noise is always preferable, practical systems almost always exhibit other limitations, such as limited dynamic range, which render noise reduction beyond some threshold SNR of limited use. To determine this threshold in our system, we varied the electronic SNR per channel, as listed in table 2, computed the psf using DELFI as described above, and used (31) to compute the contrast as a function of cyst size for our prototype system. Figures 4(a) and 4(b) depict the obtained contrast as a function of cyst size when receive apodization was implemented with flat and Nuttall windows, respectively.

It is well known that digitizer quantization affects sidelobe levels [11]. State of the art clinical scanners typically use 10 bits to represent each sample; however, compromises made in fabricating our 2D array transducer and in beamforming might render 10 bits superfluous in our prototype system. We tested this hypothesis by investigating the impact of quantization on cyst contrast in an ideal scanner with no electronic noise. We quantized the single receive element responses, obtained as described above, using different precisions (table 3) and then apodized, focused, and summed the responses. Note that the precisions listed in table 3 correspond to one real sample and therefore a full complex sample would be represented using twice the listed number of bits. The effect of quantization on cyst contrast is illustrated in figure 5.

The choice of receive f/# is an important design parameter in our system because we focus solely by phase rotation of the received data. While larger apertures improve resolution when conventional time delay focusing is used, larger apertures might degrade image quality in our system because of the limitations of DSIQ beamforming [6]. In addition, our elements are highly directive because of our large pitch (635 μm) and thus large apertures might yield higher grating lobes. We explored the impact of f/# by computing the contrast as a function of cyst size for the f/#s listed in table 4. Figure 6 plots contrast as a function of cyst size for each f/# tested.

Finally, we explored the effect of varying the apodization window on our system. We used six windows, listed in table 5. Figure 7(a) depicts contrast as a function of cyst size for each window in a noise free environment, and figure 7(b) plots the obtained contrast in the presence of electronic noise with an SNR of -10 dB per channel. It is worth noting that selecting apodization windows based solely on the presented metric might not result in the best image

quality. A particular window might reduce grating lobes and sidelobes, but if it also reduces array gain, losses in sensitivity (reduction in SNR) might outweigh the contrast benefits. Table 6 lists the contrasts (when imaging a cyst of radius 2.5 mm) and the associated sensitivities obtained using each window. Contrasts with no electronic channel noise, and noise with an SNR of -10 dB and 0 dB per channel are listed. The sensitivities were calculated from the peak magnitude of the psfs and are normalized to the sensitivity obtained using flat apodization. We use a cyst of radius 2.5 mm because one of the major applications envisioned for our C-scan system is image guided needle/IV line insertion in the arm, where the veins are approximately 5 mm in diameter.

## IV. RESULTS AND DISCUSSION

Figure 1 depicts slices of the psf obtained in our control simulation of conventional ultrasound systems, with the elevation focus at the azimuthal focus (1 cm) and at 2.8 cm. We see a similar response for the two geometries in the azimuth-range plane in 1(e) and 1(f), but as expected, the elevation focus plays a role in the azimuth-elevation and elevation-range planes in 1(a)-1(d). We see a significant broadening of the psf in these planes when the elevation focus is moved away from the azimuthal focus.

Figure 2 shows slices of the psf obtained for our C-scan system. The slice in the azimuth-elevation plane in 2(a) shows a broader mainlobe in azimuth than the 1D array in figure 1, due to our use of only phase delays for focusing. The response is also broader in elevation when compared to the 1D array with a coincident focus in azimuth and elevation. The benefit of a

variable elevation focus becomes apparent though when we compare results from our system to those from the 1D array geometry with the elevation focus at 2.8 cm. The beam is broader in elevation in the 1D case, as can be seen in 1(b) and 1(d). However, a slice of the psf obtained with the 2D array in the azimuth-range plane reveals not only a broad mainlobe but also significant grating lobes.

Figure 3 depicts a comparison of the three geometries described above. It can be seen that the contrast obtained with the 2D array is much worse than with the 1D array with a coincident azimuth and elevation foci. Recall that the metric computes the ratio of the psf energy outside the cyst to the total psf energy. Therefore, when considering the contrast curve for our system, the rightmost portion of the contrast curve (for cysts with radii greater than 4 mm) is affected only by the grating lobes. However, as the size of the cyst decreases, the effects of the sidelobes (cyst radii from 1.5 to 4 mm), and eventually the mainlobe (cyst radii less than 2 mm), come into consideration. The effects of a larger mainlobe and grating lobes combine to limit contrast in our prototype system across cysts of all sizes. However, when we compare our system to the 1D case with different foci in azimuth and elevation, we see that the mainlobe broadening in elevation in the 1D case greatly reduces contrast for that geometry. Since one of the primary applications for our system is image guided needle/IV line insertion, we are particularly interested in cysts of radii between 1.5 to 2.5 mm. In this range, we see that our system performs reasonably; an impressive conclusion considering the reductions in hardware complexity and cost of our approach.

Note that the flat region of the contrast curve (radii > 4 mm) for our system depends on the level of the grating lobes and is therefore mostly dependent on the array pitch. The array pitch in our current prototype is large (635 μm) due to printed circuit board (PCB) fabrication limitations [4]. We will reduce array pitch significantly in our next prototype, which should in turn yield an overall improvement in contrast. Under these conditions, our low cost strategies may outperform conventional 1D arrays.

Figure 4 illustrates the effect of electronic noise on receive. It can be seen, as expected, that the contrast increases with increasing SNR. The plots suggest that improving the electronic SNR much beyond 0 dB per channel will yield no noticeable improvement in image quality. While an SNR greater than 0 dB results in better contrast for large cysts, our focus on imaging cysts having a radius less than 2.5 mm  makes this result of limited relevance. As we improve our element pitch and thus reduce grating lobes, the flat region of the curves will change and we will most certainly need to reconsider the effect of SNR.

The effect of quantization can be seen in figure 5. Quantization noise significantly degrades the obtained contrast when less than 10 bits are used per real sample. While these simulations did not include the effect of electronic noise, an electronic SNR as low as 0 dB per channel should still render these results valid.

Figure 6 shows the effect of varying the f/#. We see that contrast increases with increasing f/# for large cysts. This is due to the 2D array pitch, which results in highly directive elements and thus large grating lobes when large apertures are used. Large f/#s (>f/1.5),

however, result in a very broad mainlobe and reduce contrast when imaging small cysts. Figure 6 suggests that an f/1 system would be a good compromise for imaging cysts of all sizes. While this analysis ignores the effect of aperture size on system sensitivity, sensitivity would increase with increasing aperture size. For poor SNR environments, it may be necessary to consider the impact of SNR and f/# simultaneously.

Finally, figure 7 shows the contrasts obtained using different apodization windows in the presence and absence of electronic noise. Contrasts obtained using each tested apodization window for a cyst of radius 2.5 mm are listed in table 6 for various SNR values, along with the effect of the windows on system sensitivity. There is generally an inverse relationship between contrast and sensitivity. The Nuttall window maximizes contrast for all simulated noise levels, but it is also the window most affected by electronic noise. The contrast trends seen in table 6 when the noise level is varied indicate that the Hann or Tukey windows are least affected by noise, because of comparatively high array gain. Note, however, that the Gaussian window would be a poor choice for all conditions because it yields a poorer contrast for the same sensitivity as the Hann window.

As demonstrated by the above examples, application of the proposed metric eases parameter optimization easier because any system can be characterized by a single scalar quantity. The goal of system design is then to simply maximize the cystic contrast, leaving no room for ambiguity. This is in stark contrast to use of the beamplot, in which optimization is not necessarily clear. The proposed metric is also very flexible because the mask ⧖ can be changed to match the target of interest. We could also introduce scatterers in the region defined

by the mask, as described in [2], to predict performance when imaging hypoechoic or hyperechoic lesions. Note, however, that the expressions derived in this paper for the psf energy outside and within the cyst are valid only if the mask represents an anechoic region. The major drawback of the proposed metric is that it neglects the effect of speckle statistics and size on target detectability [15]. Despite this drawback, the above metric is much better suited to characterize medical ultrasound systems than current approaches.

## VI. CONCLUSIONS

Existing methods to characterize ultrasound systems are limited in their utility. The beamplot is usually of limited use unless the goal is to image a bright point target. It is, in addition, difficult to decide how to optimize the beamplot to improve overall imaging performance. Contrast detail phantoms cannot be used to assess hypothetical systems without excessive computational costs. We built upon [2-3] to derive a metric to characterize arbitrary 3D broadband ultrasound systems including the effects of electronic noise. We presented simulation results that demonstrated the use of the metric in designing ultrasound systems, and showed that it enables the straightforward optimization of any parameter that affects image quality.

## VII. ACKNOWLEDGEMENTS

# VIII. REFERENCES

[1]     B. D. Steinberg, *Principles of Aperture and Array System Design*, John Wiley & Sons, 1976, pp. 40-52.

[2]     D. Vilkomerson, J. Greenleaf, and V. Dutt, "Towards a resolution metric for medical ultrasonic imaging," *Proc. IEEE Ultrason. Symp.,* vol. 2, pp. 1405-1410, 1995.

[3]     K. F. Üstüner and G. L. Holley, "Ultrasound Imaging System Performance Assessment," presented at the 2003 AAPM Annual Meeting.

[4]     E. Girard, S. Zhou, W. Walker, T. Blalock, and J. Hossack, "High element count two dimensional transducer array," *Proc. IEEE Ultrason. Symp.,* vol. 1, pp. 964-967, 2003.

[5]     M. I. Fuller, T. N. Blalock, J. A. Hossack and W. F. Walker, "A portable, low-cost, highly integrated, 3D medical ultrasound system," *Proc. IEEE Ultrason. Symp.,* vol. 1, pp. 38-41, 2003.

[6]     K. Ranganathan, M. K. Santy, T. N. Blalock, J. A. Hossack., and W. F. Walker, "Direct Sampled I/Q Beamforming for Compact and Very Low Cost Ultrasound Imaging," *IEEE Trans. Ultrason. Ferroelectr., Freq. Contr.*, vol. 51, no. 9, pp. 1082-1094, 2004.

[7]     A. H. Nuttall, "Some Windows with Very Good Sidelobe Behavior." *IEEE Trans. Acoust. Speech Signal Process.*, vol. 29, no. 1, pp. 84-91.

[8]     W. F. Walker, "A Spline Based Approach for Computing Spatial Impulse Responses," submitted to the IEEE Transactions on Ultrasonics, Ferroelectrics, and Frequency Control.

[9]     J. A. Jensen and N. B. Svendsen, "Calculation of pressure fields from arbitrarily shaped apodized and excited ultrasound transducers," *IEEE Trans. Ultrason. Ferroelectr., Freq. Contr.*, vol. 39, no. 2, pp. 262-267, 1992.

[10]    R. N. Bracewell, *The Fourier Transform and its Applications*, 3rd ed., McGraw-Hill, 2000, pp. 359-367.

[11]    B. D. Steinberg, "Digital Beamforming in Ultrasound," *IEEE Trans. Ultrason. Ferroelectr., Freq. Contr.*, vol. 39, no. 6, pp. 716-721, 1992.

[12]    A. V. Oppenheim, A.V., and R.W. Schafer, *Discrete-Time Signal Processing*, Prentice-Hall, 1989, pp. 447-448.

[13]    F. J. Harris, "On the Use of Windows for Harmonic Analysis with the Discrete Fourier Transform," *Proc. IEEE.* vol. 66, no. 1, pp. 51-83, 1978.

[14]    Digital Signal Processing Committee of IEEE Acoustics, Speech, and Signal Processing

Society, ed., *Programs for Digital Signal Processing,* New York: IEEE Press, 1979.

Program 5.2.


[15]    S. W. Smith, R. F. Wagner, J. M. Sandrik, and H. Lopez, "Low Contrast Detectability

and Contrast/Detail Analysis in Medical Ultrasound," *IEEE Trans. Ultrason.*

*Ferroelectr., Freq. Contr.*, vol. 30, no. 3, pp. 164-173, 1983.

**Figure and table captions -**

Figure 1:

Slices of the simulated 3D spatial psf obtained for a conventional system with a 1D array and time delay focusing. The system had a 128 element 1D array with a pitch of 135 μm and apodization was implemented on receive with a Nuttall window. We computed two psfs, one with the elevation focus at the azimuthal focus of 1 cm and another with the elevation focus at 2.8 cm. (a), (c), and (e) depict slices in azimuth-elevation, elevation-range, and azimuth-range respectively, for the system with a coincident focus. (b), (d), and (f) depict slices in azimuth-elevation, elevation-range, and azimuth-range respectively, with the elevation focus set to 2.8 cm. The beam broadens significantly in elevation when the elevation focus is moved away from the azimuthal focus.

Figure 2:

Slices of the simulated 3D spatial psf obtained simulating the first generation prototype of our low-cost C-scan system with a 2D array and direct sampled I/Q (DSIQ) beamforming. Relevant parameters are listed in table 1. (a) and (b) depict slices in azimuth-elevation and azimuth-range respectively. Due to symmetry, the elevation-range slice is identical to the azimuth-elevation slice and is therefore not shown. The mainlobe is broader in azimuth than both 1D array cases in figure 1, and broader in elevation than the 1D array case with a coincident focus in azimuth and elevation. However, the use of a 2D array enables a variable elevation focus and therefore results in a narrower mainlobe in elevation when compared to the 1D case with different azimuthal and elevation foci. An important and undesirable result of a large pitch

(635 μm) in our 2D array is large grating lobes as seen in (b).

Figure 3:

      Comparison of our prototype C-scan system with a conventional system. Cystic contrast was computed using (34) and is plotted as a function of cyst size. The rightmost portion of the curve (for large cysts) is affected largely by the grating lobes. As the radius of the cyst decreases, the effects of the sidelobes, and eventually the mainlobe, come into consideration. The contrast obtained with the 2D array is poorer than with the 1D array with a coincident focus in azimuth and elevation, due to larger grating lobes and mainlobe in our system.  However, our system outperforms the 1D array system focused at 2.8 cm when imaging small cysts (radii < 1.5 mm) because of the poor elevation beamwidth of the 1D array system. Since one of the primary applications for our low-cost system is image guided needle/IV line insertion, we are most interested in cysts of radii between 1.5 to 2.5 mm. In this range, we see that our system is comparable to the conventional system. Note that we will reduce the array pitch significantly in future generations of our system, and thus hope to reduce grating lobes and improve contrast.

Figure 4:

      Effect of electronic noise. Contrasts were computed using (31) for the SNRs listed in table 2 and are shown as a function of cyst size when receive apodization was implemented using (a) a flat window and (b) a Nuttall window. Image quality improves with increasing SNR, as can be seen, although improving the electronic SNR much beyond 0 dB per channel seems to offer little advantage.

Figure 5:

Effect of quantization. Single receive element responses were quantized using different precisions (table 3) for each real sample, and then apodized, focused, and summed to yield 3D responses. Contrasts were computed using (34) and are plotted as a function of cyst size. Performance is significantly worse when less than 10 bits per real sample are used. We did not include the effects of electronic noise in these simulations; however, from figure 4, an electronic SNR of 0 dB per channel or better would render these results valid.

Figure 6:

Effect of f/#. Contrasts were computed using (34) and are plotted as a function of cyst size for the f/#s listed in table 4. Contrast generally improves with increasing f/#, the highly directive array elements of our prototype system increase grating lobes when large apertures are used. Large f/#s (>f/1.5) result in a very broad mainlobe and reduce contrast when imaging small cysts. An f/1 system results in good all round performance. Note that sensitivity is ignored in these simulations but increases with decreasing f/#.

Figure 7:

Effect of apodization with (a) no electronic noise, and (b) electronic noise with SNR -10 dB per channel. Contrasts were computed using (34) in the noise-free case and (31) when noise was considered, using psfs obtained with the apodization windows listed in table 5 and are plotted as a function of cyst size. The Nuttall window yields the best contrast for cysts of all sizes. Although the contrast values obtained using the Nuttall window are also the most affected

by noise (better perceived in table 6), it yields the best performance through the range of noise levels that we investigated.

Table 1:

List of default parameters used to simulate our C-scan system.

Table 2:

Single receive channel SNR values used with (31) to estimate the impact of electronic noise.

Table 3:

Number of bits used to represent each real value to determine the minimum precision required in our system.

Table 4:

F/#s used on receive to determine the optimal f/# for our system.

Table 5:

Windows used to determine the impact of receive apodization on cyst contrast.

Table 6:

Contrasts obtained for a cyst of radius of 2.5 mm with varying amounts of electronic noise using different apodization windows, and their associated sensitivities or array gain

normalized to the array gain obtained using flat apodization. Contrasts with no electronic channel noise, and noise with an SNR of -10 dB and 0 dB per channel are listed. Contrasts were computed using (34) in the noise-free case and (31) when noise was considered. The Nuttall window maximizes contrast for all simulated noise levels, while the flat and Tukey windows are least affected by electronic noise because of comparatively high array gain. Note that the Gaussian window is a poor choice for this geometry as it yields less contrast for the same sensitivity as the Hann window.
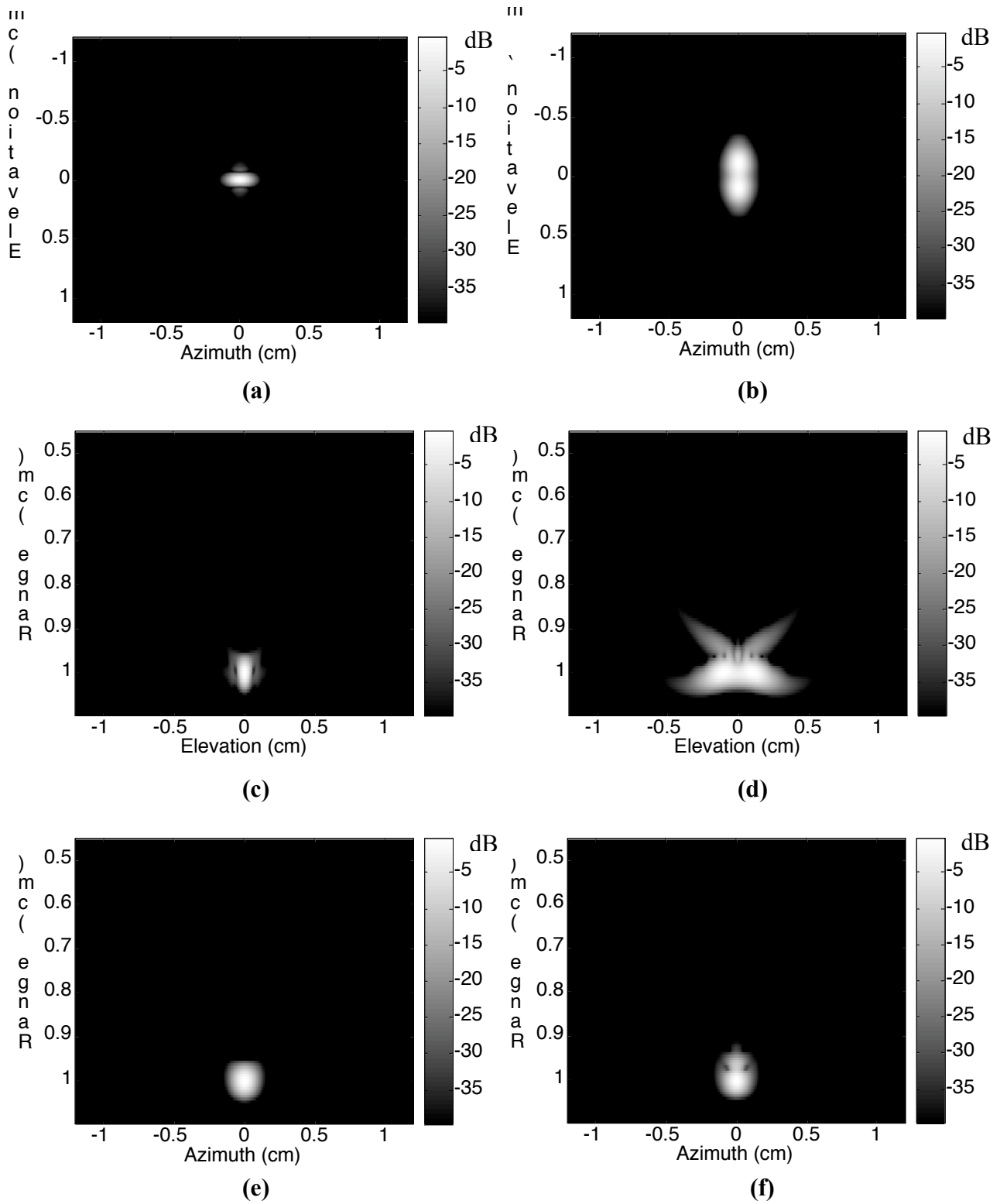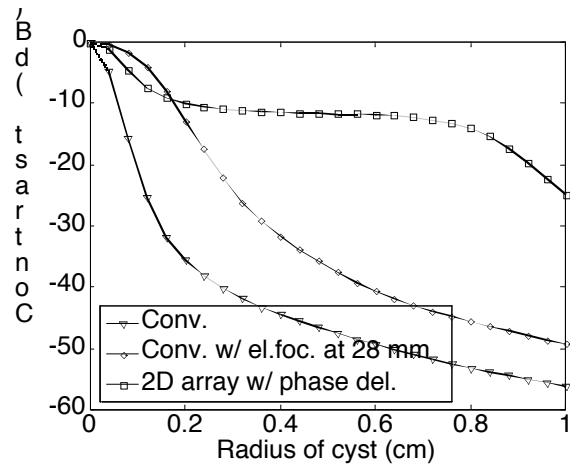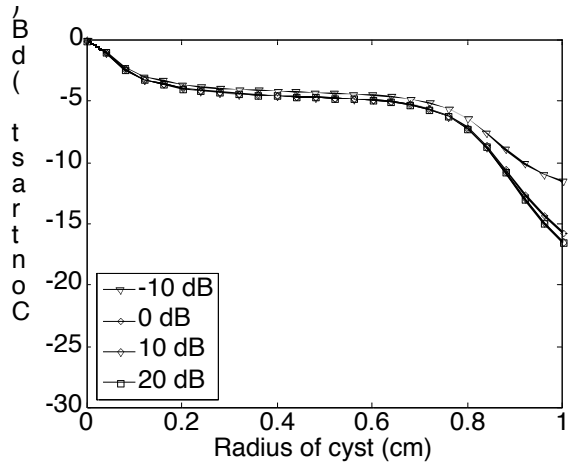
**Figure 1**
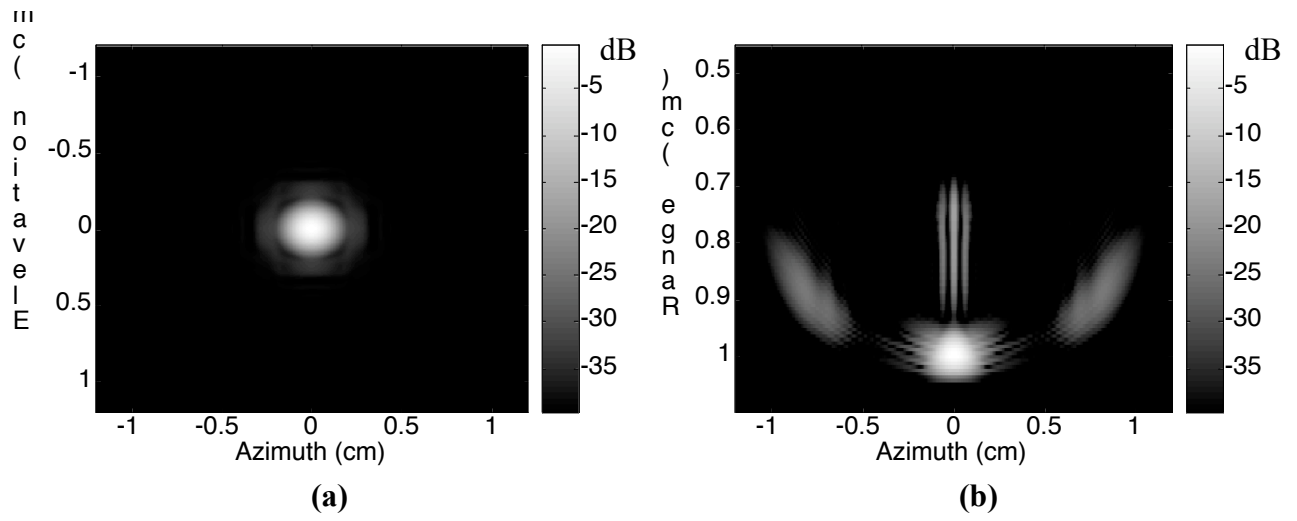
**Figure 2**

**Figure 3**

**(a)**
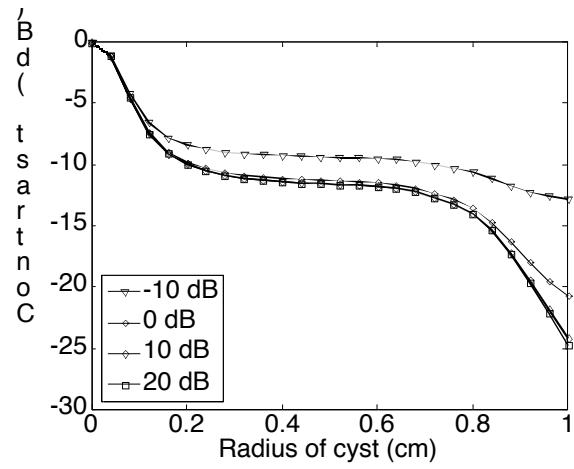
**(b)**

**Figure 4**
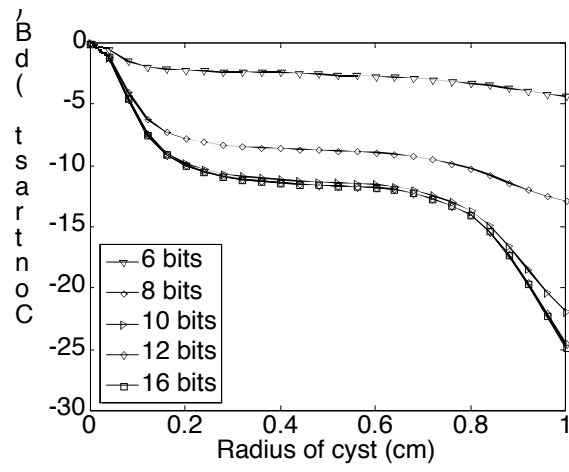
**Figure 5**
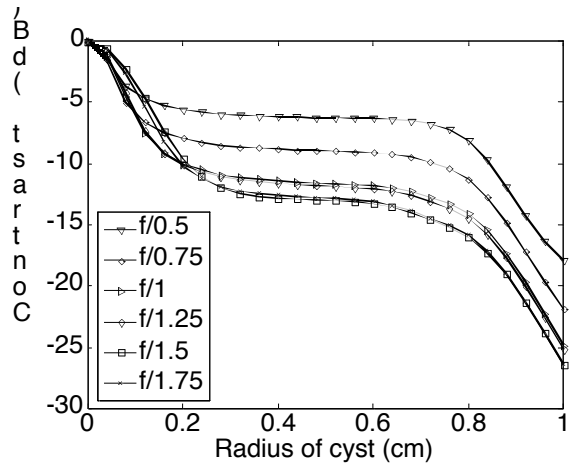
**Figure 6**
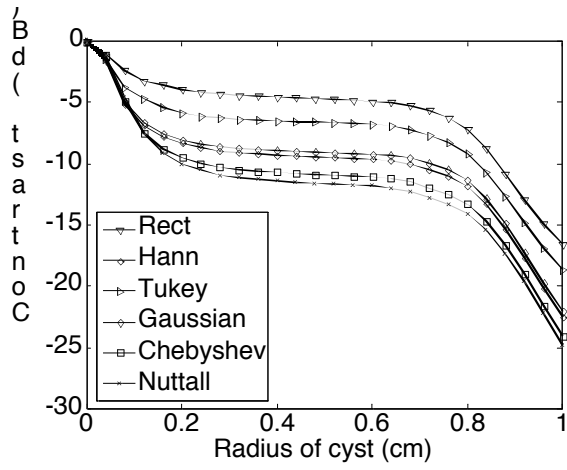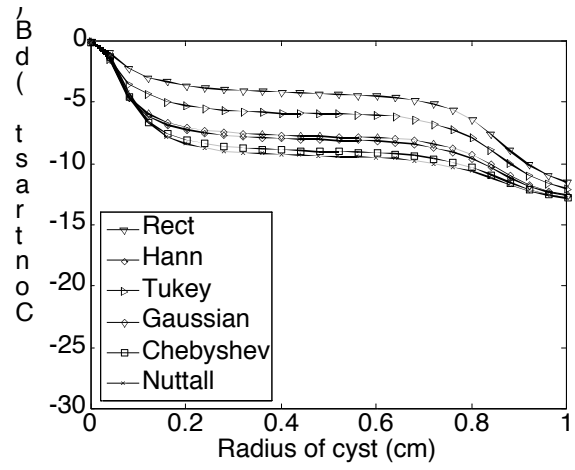
**(a)**                                    **(b)**

**Figure 7**

| | |
|---|---|
| 2D array layout | 32 x 32 |
| Pitch | 635 µm |
| Receive focus | 1 cm |
| f/# | 1 |
| Receive apodization | Nuttall window |
| Transmit pulse center frequency | 3.3 MHz |
| Transmit pulse length | 3 cycles weighted by a Nuttall window |
| Spatial window over which psf was computed | Cylindrical volume with radius 2.4 cm and height 1 cm |
| Spatial sampling | 60 µm radially, 1 degree in angle, and 60 µm in range |

**Table 1**

| Electronic SNR per channel (dB) |
| --- |
| -10 |
| 0 |
| 10 |
| 20 |

**Table 2**

| Quantization (# bits) |
| --- |
| 6 |
| 8 |
| 10 |
| 12 |
| 16 |

**Table 3**

| f/# |
| --- |
| 0.50 |
| 0.75 |
| 1 |
| 1.25 |
| 1.5 |
| 1.75 |

**Table 4**

| Apodization |
| --- |
| Flat |
| Hann [12] |
| Tukey [13] |
| Gaussian [13] |
| Chebyshev (relative sidelobe attenuation of 100 dB) [14] |
| Nuttall [7] |

**Table 5**

| Window | Array gain (dB) | Contrast (dB) with - 10dB electronic SNR | Contrast (dB) with 0 dB electronic SNR | Contrast (dB) with no electronic noise |
|---|---|---|---|---|
| Rect | 0 | -4 | -4 | -4 |
| Hann | -7 | -8 | -9 | -9 |
| Tukey | -2 | -6 | -6 | -6 |
| Gaussian | -7 | -7 | -8 | -8 |
| Chebyshev | -9 | -8 | -10 | -10 |
| Nuttall | -11 | -9 | -10 | -11 |

**Table 6**

**Optimal Apodization Design for Medical Ultrasound using Constrained Least Squares.
Part I: Theory**
**D. A. Guenther and W. F. Walker**

**Abstract**

Aperture weighting functions are critical design parameters in the development of ultrasound systems because beam characteristics affect the contrast and point resolution of the final output image. In previous work by our group, we developed a metric which quantifies a broadband imaging system's contrast resolution performance [1]. We now utilize this metric to formulate a novel general ultrasound beamformer design method. In our algorithm we use constrained least squares (CLS) techniques and a linear algebra formulation to describe the system point spread function (psf) as a function of the aperture weightings. In one approach we minimize the energy of the psf outside a certain boundary and impose a linear constraint on the aperture weights. In a second approach we minimize the energy of the psf outside a certain boundary while imposing a quadratic constraint on the energy of the psf inside the boundary. We present detailed analysis for an arbitrary ultrasound imaging system and discuss several possible applications of the CLS techniques, such as designing aperture weightings to optimize cystic resolution and improve the system depth of field. Simulation results are presented in an accompanying paper [2].

**Introduction**

The determination of array aperture weights which produce a synthesized beam pattern with a narrow mainlobe and low sidelobes is a classical problem with a rich history in the signal processing literature. Dolph used Chebyshev polynomials to calculate aperture weights for a uniformly spaced, continuous wave linear array that achieved the minimum possible beamwidth

for a given maximum sidelobe level [3]. Taylor expanded this formulation to achieve tapered sidelobes further away from the mainlobe for continuous apertures [4], and Villeneuve applied it to discrete arrays [5]. Alfred H. Nuttall, in his paper [6], improved upon the Blackman-Harris window to achieve beam patterns whose maximum sidelobes are minimized. Whereas these previous papers focused on uniformly spaced arrays, Olen and Compton developed an iterative procedure using an arbitrarily shaped adaptive array to produce the desired sidelobe behavior by using a recursive feedback procedure [7]. Tseng and Griffiths also produced a simple iterative algorithm that can be used to find array weights for nonuniform geometries to produce beam patterns with a given look direction and minimum energy in the sidelobes [8]. An interesting outcome of their methods allowed for the design of beam patterns where the desired sidelobe response could vary with angle.

Although these previous methods produced excellent results narrowband assumptions, computational complexities, and iterative procedures limit their applicability to general ultrasound beamformer design. Considerable gains can be made in computation time with the use of least squares methods. In fact, over the last two decades many authors have developed constrained least squares algorithms for the design of FIR filters [9-12]. These methods typically minimize the error of the filter over a certain frequency band with respect to some desired filter response. For example, Selesnick described a constrained least squares approach to design FIR filters that did not require the specification of a transition band of frequencies between the passband and stopband. By setting up a minimization problem on the $l^2$ error of the filter's amplitude response subject to linear equality constraints, Selesnick derived filters with minimum error and devoid of Gibb's phenomenon [9]. Other authors used least squares methods to produce eigenfilters, or filters that minimize a quadratic error measure in the passband and

stopband [10-12]. Later in a series of papers, Er *et al.* employed a variety of constrained least squares techniques to synthesize arbitrary array patterns subject to different criteria such as sidelobe level and mean squared sidelobe energy. Their algorithms employ linear and quadratic constraints to achieve array patterns for general array geometries which produce beam patterns that are highly directional with very low sidelobes [13-18].

The rich history of array pattern synthesis optimization has been only recently applied to medical ultrasound imaging and most applications have been specialized [19-23]. For example, Ebbini and Cain [19] proposed a method for synthesizing multiple focal regions on single transmit events for applications in hyperthermia treatment via ultrasound. Li *et al.* [20] used a total least squares method to compensate for psf degradation due to "dead" array elements or elements blocked by acoustically opaque windows in the interrogated media. Recently, Wilkening *et al.* designed optimal FIR filters for improved image contrast in contrast agent imaging [22] and FIR filters that increased the depth of field for dynamic receive focusing [23]. Although insightful and useful, these methods failed to address the larger problem of general beam pattern synthesis given arbitrary arrays. Previously, our group developed a general aperture design tool, supported by rigorous theory that is applied to the design of aperture weighting functions for arbitrary system design [24], [25]. The method utilized a minimum sum squared error (MSSE) formulation between the system psf and the desired or goal psf. One strength of the approach is that it allowed for full beam optimization given system parameters obtained through theory, simulation, or experiment. The method is useful because it allows for the design of any controllable system parameter in a straightforward, rigorous, time efficient manner. Ranganathan's approach, although extremely useful in aiding the design of prototype systems, suffers from the lack of a quantitative measure detailing how system performance

changes with respect to a deviation in system parameters. Furthermore, the approach offers no guidance in the selection of an appropriate goal point spread function. These shortcomings make system optimization using the MSSE approach difficult.

The method of apodization profile design presented in this paper is general enough to be applied to any coherent imaging system and is similar to many of the previous array pattern synthesis techniques utilizing constrained least squares (CLS). For example, our linearly constrained least squares (LCLS) formulation is similar to the array pattern synthesis technique by Tseng [8], and our quadratically constrained least squares (QCLS) formulation is similar to the constrained eigenfilter design [10], [26]. However while these prior analyses were for a single carrier frequency, we use a broadband formulation. Keitmann-Curdes *et al.* [27] previously developed an algorithm similar to our QCLS formulation which generated apodization profiles for ultrasound imaging with minimum sidelobe energy of the two dimensional space-time psf. Recently Schwann *et al.* used two different resolution criteria to design optimal frequency dependent apodization profiles [28], a method whose goals are similar to ours of improving image contrast. However, their multiple objective formulation requires computationally expensive iterative methods to arrive at one Pareto optimum solution, or a solution where further improving one objective necessarily degrades all others [29]. Further review of the differences between our LCLS and QCLS methods and the techniques mentioned above will be discussed in more detail later in this manuscript.

Since the ultrasound system's beam characteristics fundamentally affect the quality of the image, a great deal of effort is put into optimizing system parameters. Estimating the imaging performance of ultrasound systems is critical, both to characterize the fundamental imaging limits of the system, and to optimize image quality. It is possible to estimate the performance of

existing systems by imaging phantoms or human subjects, but it is necessary during system design to be able to determine imaging performance prior to system construction. The ability to accurately predict performance enables system optimization, quantitative consideration of engineering tradeoffs, and significantly reduces the time and cost investment in system development.

Synthesis of beampatterns in diagnostic ultrasound receives a great deal of attention during system design. The system's spatial impulse response, or point spread function, characteristics will determine such parameters as point resolution and contrast in the resulting image. Thus control over mainlobe width and sidelobe level is significant. These beam parameters are influenced by the size of the active aperture, the frequency of the ultrasound pulse, the magnitude and phase (or time delay) of the weightings applied to the active elements, and the pulse length. Because so many factors affect the characteristics of the psf and there is no global parameter describing psf quality, beamforming parameters are usually determined through iterative simulation and experimentation.

A quantitative resolution metric is essential to guide optimization of system parameters, including the system's psf. The most common measure of scanner performance is the beamplot [30], which has been adapted from RADAR. The -6dB beamwidth of the beamplot, the full width at half maximum (FWHM), and the beamwidth at other levels are used to estimate scanner resolution. Sidelobe and grating lobe levels are used to estimate eventual image contrast. Although widely used in medical ultrasound, there are scenarios in which the FWHM criterion indicates excellent performance, but actual images of tissue do not reveal important details.

Vilkomerson *et al.* addressed the limitations of the beamplot and proposed the concept of "cystic resolution" [31] in which performance was quantified as the size of a void that produced

a given contrast. The analysis, while novel and useful, was limited to narrowband circular apertures and neglected the axial dimension. Johnson [32] further developed the contrast resolution metric to include a 3D broadband model for circular apertures and compared different imaging parameters using maximum output contrast curves versus cyst diameter. Üstüner *et al.* [33] extended cystic resolution to a 3D broadband model for arbitrary apertures, but did not describe its theoretical foundation, resulting in a limited understanding of the formulation and its utility and drawbacks. A general cystic resolution metric was previously derived by our group [1]. This metric accounts for the effect of electronic noise and, under certain assumptions, reduces to that described in [33]. Whereas, the FWHM criterion sometimes provides misleading information about resolution in ultrasound systems, the cystic resolution metric identifies specific points in the psf of the system that can be optimized to increase image quality and performance.

This paper utilizes the cystic resolution metric to guide optimization of apodization profiles for coherent imaging systems. Specifically, we design optimal receive apodization profiles for a 1D linear array; however, our theory can be applied to a 2D array of arbitrary geometry and can be used to design one way or two way apodization profiles. We propose two different methods for optimal apodization design. The first algorithm minimizes the energy of the psf outside some specified region subject to a linear constraint of the apodization weights. We call the resultant weights the linearly constrained least squares (LCLS) apodization profile. The second algorithm minimizes the energy of the psf outside some region subject to a quadratic energy constraint of the psf inside the boundary. We call the resultant weights the quadractically constrained least squares (QCLS) apodization profile.

Our CLS apodization design methods return real weights and achieve a spatial impulse response with minimum sidelobe levels in a least squares sense given a specified mainlobe area. We formulate the problem starting from basic principles of acoustic wave diffraction theory and apply linear algebra techniques to represent the system psf. We generate a least squares problem subject to either a linear or quadratic constraint in order to minimize the energy outside a given mainlobe area in the psf. The algorithm can be applied to enhance the depth of field (DOF) in an imaging system as well as improve lesion detectability in inhomogeneous scattering media. The algorithm is arguably optimal for detecting anechoic cysts via ultrasound; however we believe it will also improve ultrasound system performance in general imaging applications. This paper outlines the theoretical description of the constrained least squares technique for designing apodization profiles for broadband, coherent imaging systems, describes a technique for reduced computational cost, and finally discusses examples of application. Results from simulations are presented in an accompanying paper [2].

**Theory**

We present two-way broadband formulations for the LCLS and QCLS apodization design technique. The one-way broadband formulation can be expressed in a similar manner; however we note that in most ultrasonic imaging applications, apodization is typically applied only on receive and the two-way impulse response is of greater interest.

*Linear Algebra Formulation of the Broadband Spatial Impulse Response (psf)*

The acoustic pressure field emanating from a transducer during pulse echo propagation at a single point in space at a single instant in time can be expressed as the product of a propagation

matrix, $S$, and a set of aperture weightings, $w$. The propagation matrix uses superposition to describe the contribution of each transducer element at each field point at an instant in time. The propagation function may be derived from the Rayleigh-Sommerfeld diffraction equation derived in ([34, pp.46-50]) and may also include a term relating to limited element angular response [35]. Alternatively, the propagation matrix may be computed via broadband simulation or estimated experimentally. For our formulation, $S$ is a function of the transmit aperture weights, the excitation pulse, and the individual element impulse responses of the transmit and receive apertures [24].

The two way pulse echo propagation matrix, $S$, for a fixed transmit aperture and a $n$ element receive aperture at a total number of $p$ points in three dimensional space is:

$$S = \begin{bmatrix} s_{1,1} & s_{1,2} & \cdots & s_{1,n} \\ s_{2,1} & . & \cdots & . \\ \vdots & \vdots & \ddots & \vdots \\ s_{p,1} & . & \cdots & s_{p,n} \end{bmatrix}, \tag{1}$$

where $s_{i,j}$ is the contribution of the $j$th element at the $i$th point in space. The receive aperture weighting function, $w$ , for each of the $n$ elements used on receive can be written in vector form as:

$$w = \begin{bmatrix} w_1 & w_2 & w_3 & \cdots & w_n \end{bmatrix}^T , \tag{2}$$

where T denotes the vector transpose operation. Using (1) and (2), we can now write the complete two-way pulse echo system psf, $P$, as follows:

$$P = Sw , \tag{3}$$

the propagation matrix multiplied by the receive weighting vector. Note that this results in the one dimensional column vector, $P$, of length $p$ the total number of points in three dimensional space where the system psf is measured.

This formulation can be expanded to describe the psf as a function of time. In this case, the receive weightings would be a function of element number and time, essentially forming the coefficients of a FIR filter on each receive channel. Adequate spatial and temporal sampling of the three dimensional psf yields huge propagation matrices, and therefore for this and the accompanying paper we have limited our analysis to a single instant in time and two spatial dimensions, azimuth and range. Clearly the elevation dimension matters in planar ultrasonic B-mode images, even with acoustic lenses on linear arrays. However, restricting our analysis to two dimensions eases visualization of the algorithm while still providing meaningful results.

*Cystic Resolution Metric*

The goal of the cystic resolution metric is to quantify the contrast resolution of an arbitrary broadband ultrasound system. We refer the reader to [1] for a more detailed discussion of the derivation of the metric and highlight the meaningful results here. The metric completely characterizes the 4D spatiotemporal contrast performance for a system imaging an anechoic void. However, analysis at the instant in time when the received signal is minimum (i.e. when as much of the psf energy as possible lies within the cyst) is usually sufficient. At this single instant in time, the psf can be expressed as a function of 3D space at the time of interest. The SNR is also considered at the time of interest ($SNR_{t_o}$). The contrast of the cyst relative to the background is defined as the ratio of the rms signal received from the cyst to the rms signal received from the background [1]:

$$C_{t_0} = \sqrt{\frac{1 + SNR_{t_o}^2 \frac{E_{out}}{E_{tot}}}{1 + SNR_{t_o}^2}} \quad , \tag{4}$$

where $E_{out}$ is the psf energy outside the cyst and $E_{tot}$ is the total psf energy, both at time $t_o$. Equation (4) describes the contrast of an anechoic cyst, whose size and location are described by a mask, relative to background speckle obtained by an imaging system with a given psf and electronic SNR defined statistically by $SNR_{t_o}$. Neglecting electronic noise, $SNR_{t_o}$ becomes infinite and (4) can be modified to the equation for contrast presented in [33], which is simply the square root of the ratio of the psf energy outside the cyst and the total psf energy:

$$C_{t_o} = \sqrt{\frac{E_{out}}{E_{tot}}} \quad . \tag{5}$$

The contrast for cysts of different sizes can be computed using the above expressions for cystic contrast, and system performance can be characterized as a function of cyst size as in [1, 31-33]. This metric can be used for 4D spatiotemporal analysis of broadband ultrasound systems, but 3D spatial analysis using (4) or (5) is typically adequate to characterize scanner performance as temporal analysis does not usually provide critical information. Note that in certain cases, it is valuable to compute the metric with cysts at different locations to quantify the depth of field, the effect of dynamic focusing, and other factors pertaining to the shift variance of the imaging system. Note also that while the metric can be used to determine cystic resolution, it can also be used to optimize system parameters by computing contrast as a function of cyst size and determining parameter values that maximize the contrast at the cyst sizes of interest.

*Linearly Constrained Least Squares (LCLS) Apodization Design*

One conspicuous result of the above resolution metric is that cystic contrast, or our objective function, is defined in terms of the spatiotemporal psf energy. In fact, contrast would be maximum if all the energy of the psf lay inside the void of the cyst. Whereas beamplot details can be misleading about overall image quality, this metric considers the psf globally to determine the impact on cystic contrast. Contrast improves when the psf energy outside the cyst boundary is reduced or the psf energy inside the cyst is increased. The cystic resolution metric defines a simple objective function for maximizing cystic contrast. The reader should note that different objective functions could be formulated, such as improving point contrast, but for the discussion presented here we focus on improving cystic contrast.

Cystic contrast is degraded by the presence of psf energy outside the cyst. We minimize this energy by solving for the set of receive aperture weights that, when applied to the synthetic receive element responses, will yield a psf with minimum energy outside the designated cyst boundary. Combining the above resolution metric with our linear algebra formulation of the psf, our beam synthesis problem becomes determining the vector of weights that minimize the psf energy outside the cyst boundary subject to a linear constraint to avoid the trivial case of all the receive weights set equal to zero. This is analogous to the problem of solving for the set of FIR filter coefficients that minimize the energy in the stopband.

Assuming the psf is focused at the center of the cyst, the algorithm is initialized by selecting the spatial points of the psf which lie outside the cyst boundary. We form the associated propagation matrix, $S$, which has as many rows as the number of points outside the cyst region and as many columns as elements in the active receive aperture. Therefore, each column of the $S$ matrix is one focused synthetic receive element response at all the spatial points outside the cyst boundary. Ranganathan's MSSE beamformer design approach outlined in [24]

and [25] uses focused or unfocused aperture propagation matrices. Although imaging scenarios exist with unfocused apertures, for the CLS apodization design technique presented here, we pre-focus our two way psfs so that the peak of the mainlobe lies in the center of the cyst boundary. This allows us to maximize the cost function in (5), cystic contrast. Using unfocused apertures is possible with the CLS formulation, but unfocused apertures would not typically be used for imaging cysts so a new cost function should be derived to reflect the system's intended application.

The CLS algorithm calculates the weights which minimize the energy in the sidelobe regions while simultaneously maintaining a peak gain at the center of the cyst. These weights are determined from the constrained least squares problem:

$$\min_{w} \left\| Sw \right\|^2 \quad \text{subject to the linear constraint} \quad C^T w = 1 . \tag{6}$$

In this expression $\left\| \bullet \right\|^2$ denotes the square of the $\ell^2$-norm and the row vector $C^T$ has elements corresponding to the amplitude of each synthetic receive element response. More specifically, $C^T$ is a vector of the amplitudes of the receive element responses at the focus in the center of the cyst. The expression in (6) is common in the signal processing literature and drawing upon [36] the optimal receive aperture weightings are given by:

$$w_{opt} = (S^T S)^{-1} C [C^T (S^T S)^{-1} C]^{-1} , \tag{7}$$

where $(\bullet)^{-1}$ denotes the matrix inverse operation. Equation (7) provides a simple method to calculate the receive weightings that will minimize the energy in the psf outside a specified mainlobe region while simultaneously achieving peak gain inside the mainlobe region. The optimal receive weights minimize $E_{out}$ in (5) above, so we expect to see improved cystic contrast

using the LCLS apodization windows over commonly used windows such as the flat, Hamming and Nuttall [6] windows.

*Linearly Constrained Least Squares Apodization Design with Weighting Function*

In certain applications, the psf characteristics at specific spatial positions may be more important than others because of the effects that the psf has on point resolution and system contrast. For example, in hyperthermia applications the ultrasonic field pattern requires high power levels at some points while reducing the power deposition at other potential hot spots [19]. In other applications, it may be more important to reduce sidelobe levels than to precisely control the mainlobe. In these cases and others we can incorporate a weighting function, *g*, that emphasizes or deemphasizes certain spatial points in the psf during the apodization design procedure. The LCLS apodization design problem can be rewritten with the weighting function as:

$$\min_{w}\|g_d Sw\|^2 \quad \text{subject to the linear constraint} \quad C^T w = 1 \quad , \tag{8}$$

where $g_d$ is a diagonal *p* x *p* matrix with elements of *g* along the $0^{th}$ diagonal. The elements of *g* have a large value where minimizing psf energy is important and smaller values where the psf energy is less critical. The solution for optimal receive weightings, drawing upon [36] is:

$$w_{opt} = (S^T g_d^T g_d S)^{-1} C [C^T (S^T g_d^T g_d S)^{-1} C]^{-1} \quad . \tag{9}$$

*Quadratically Constrained Least Squares (QCLS) Apodization Design*

The LCLS apodization design algorithm minimized the energy in the psf outside a given region of the mainlobe. By doing so the cystic contrast should improve according to (5). This

analysis minimizes the numerator of (5); however, it ignores the denominator. As a result, although the energy outside the cyst will be minimized the total psf energy could also be decreased thus limiting cystic contrast improvements. We therefore develop an alternate approach where we minimize the energy of the psf outside a given boundary while at the same time keeping the energy of the psf inside the boundary constant. This formulation becomes similar to the earlier beam synthesis problem of creating eigenfilters [10], [26]. In the FIR eigenfilter design case, the energy constraint on the filter coefficients is usually just the quadratic constraint $w^T w = 1$ which constrains the total energy of the filter's frequency response to be unity. However, for broadband beamformers, this constraint is meaningless and we must devise a new formulation [26]. The modified quadratic constraint is straightforward given the cystic resolution metric. We wish to minimize $E_{out}$ while maximizing $E_{tot}$ in (5), and we can change $E_{tot}$ to just the psf energy inside the cyst boundary, $E_{in}$. Note that this problem can be set up as a multiple objective optimization problem [29], [37]. However, that approach does not yield an intuitive optimal solution like utilizing the cystic resolution metric does. Therefore, we choose to formulate this problem using a quadratically constrained least squares formulation:

$$\min_{w} \| S_{out} w \|^2 \quad \text{subject to the quadratic constraint} \quad \| S_{in} w \|^2 = 1 \quad , \tag{10}$$

where $\| \bullet \|^2$ denotes the square of the $\ell^2$-norm, $S_{out}$ is the propagation matrix for all the spatial points of the psf lying outside the cyst boundary, and $S_{in}$ is the propagation matrix for all the spatial points of the psf lying inside the cyst boundary. Note that the quadratic constraint essentially keeps the energy of the psf inside the cyst constant. Drawing upon [26], [38-40] the optimal receive aperture weightings satisfying the quadratic constraint is the generalized eigenvector, $w_{eig}$, corresponding to the minimum generalized eigenvalue resulting from the

generalized eigenvalue decomposition problem of $S_{out}^T S_{out}$ and $S_{in}^T S_{in}$. The generalized eigenvalue problem [38, pp. 375-376] for a matrix pair, $(A, B)$ both n x n matrices, is finding the eigenvalues, $\lambda_k$, and the eigenvectors, $x_k \neq 0$, such that:

$$Ax_k = \lambda_k Bx_k \quad .$$ (11)

The number of eigenvalues, $k$, is dependent upon the rank of matrix $B$. One of the main advantages of the QCLS technique is that no matrix inversion is required to solve for the optimal apodization profile, unlike the LCLS apodization design.

*Quadratically Constrained Least Squares Apodization Design with Weighting Function*

As with the LCLS apodization design, a weighting function, $g$, can be added that emphasizes or deemphasizes certain regions of the psf during the minimization process. Rewriting the QCLS apodization design problem above with the added weighting function we arrive at:

$$\min_w \left\| g_{out} S_{out} w \right\|^2 \quad \text{subject to the quadratic constraint } \left\| g_{in} S_{in} w \right\|^2 = 1 \;,$$ (12)

where $g_{out}$ is a diagonal $p$ x $p$ matrix with elements of $g$ associated with the spatial points of the psf outside the cyst boundary along the $0^{th}$ diagonal, and $g_{in}$ is a diagonal $q$ x $q$ matrix with elements of $g$ associated with the spatial points of the psf inside the cyst boundary along the $0^{th}$ diagonal. We solve this problem by forming the Lagrangian and utilizing the necessary conditions for a minimum:

$$L(w, \lambda) = w^T S_{out}^T g_{out}^T g_{out} S_{out} w - \lambda(w^T S_{in}^T g_{in}^T g_{in} S_{in} w - 1) , \quad (13)$$

where $\lambda$ is the associated Lagrange multiplier. Following the Kuhn-Tucker conditions, a necessary condition for a minimum is that $\dfrac{\partial L}{\partial w} = 0$ [37]. Thus taking the associated partial derivative of the Lagrangian with respect to the weighting vector we arrive at:

$$S_{out}^T g_{out}^T g_{out} S_{out} w = \lambda S_{in}^T g_{in}^T g_{in} S_{in} w . \quad (14)$$

Therefore the set of optimal receive weightings satisfying (14) is again the generalized eigenvector, $w_{eig}$, corresponding to the minimum generalized eigenvalue resulting from the generalized eigenvalue decomposition problem of $S_{out}^T g_{out}^T g_{out} S_{out}$ and $S_{in}^T g_{in}^T g_{in} S_{in}$.

*Reduced Computational Cost Through Symmetry Relations*

The computation of CLS apodization profiles requires significant resources due to the large propagation matrices and matrix inverse operations (for the LCLS design method). In order to reduce the computational complexity of the algorithm we take advantage of the lateral symmetry present in the system psf for symmetric, non-steered apertures. This symmetry means that we can use just half of the system psf for the calculations of the optimal weightings. The propagation matrix, *S*, then becomes:

$$S = \begin{bmatrix} s_{1,1} & s_{1,2} & \cdots & s_{1,n} \\ s_{2,1} & . & \cdots & . \\ \vdots & \vdots & \ddots & \vdots \\ s_{p/2,1} & . & \cdots & s_{p/2,n} \end{bmatrix} , \quad (15)$$

16

where $S$ is a $(p/2)$ x $(n)$ matrix, consisting of the pressure field at only $p/2$ points in space for each element $[1, 2, \ldots n]$.

The symmetry of the non-steered receive aperture is another property that can be exploited to reduce computational cost. As shown in Fig. 1, pairs of elements can be grouped together that are the same distance from the center axis of the array. Pairing is possible because these elements should have the same weights applied, assuming no beam steering and an even number of elements in the aperture. Therefore the propagation matrix can be rewritten:

$$
S = \begin{bmatrix} s_{1,1,n} & s_{1,2,n-1} & \cdots & s_{1,n/2,n/2+1} \\ s_{2,1,n} & \cdot & \cdots & \cdot \\ \vdots & \vdots & \ddots & \vdots \\ s_{p/2,1,n} & \cdot & \cdots & s_{p/2,n/2,n/2+1} \end{bmatrix} , \tag{16}
$$

where $s_{i,j,k}$ is the response at the point $i$ in space for the element $j$ plus the response for element $k$ at the same point in space. The aperture weights must also be reshaped as:

$$
w = \begin{bmatrix} w_{1,n} & w_{2,n-1} & w_{3,n-2} & \cdots & w_{n/2,n/2+1} \end{bmatrix}^T , \tag{17}
$$

where $w_{i,j}$ is the weight applied for element $i$ and element $j$, respectively.

The derivation is now analogous to that in (6) and (10) and the optimal weights can be determined directly. The use of symmetry reduces the size of the propagation matrix, $S$, by a factor of 2 in each dimension, for a total reduction of a factor of 4 in memory requirements. The computational savings will be even greater since the necessary solution algorithms have polynomial costs as a function of matrix size.
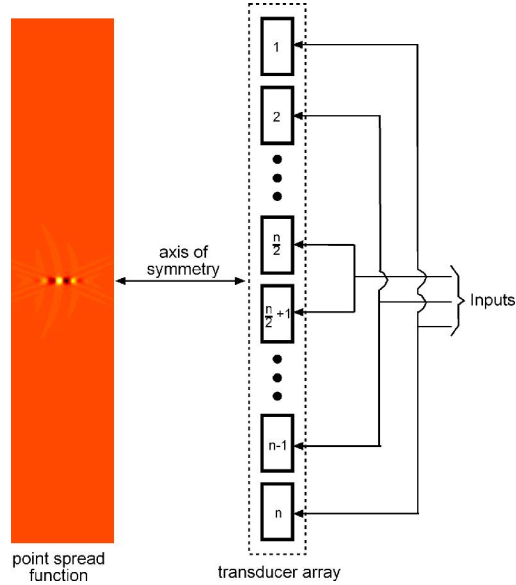
Fig. 1. Exploitation of symmetry for reduced computational cost. The aperture is symmetric about the center axis; therefore pairs of elements that would have the same weights are grouped together. Also, the lateral symmetry in the psf about the same center axis allows for analyzing just one half of the psf. This symmetry assumes a symmetric non-steered aperture.

## Applications

Although the CLS apodization profiles discussed above were constructed to optimize cystic resolution, the techniques are general enough to be applied in wide-ranging scenarios. A few possible applications are described.

### A. *Improved Cystic Contrast and Improved Point Resolution*

The cystic resolution metric described in [1] stated that the point contrast of an ultrasound system imaging a cyst is a function of the psf energy. Neglecting system SNR, we note that according to (5) we can improve the contrast of a cyst in two ways. If we minimize the energy of the psf outside the cyst boundary, the numerator in (5) decreases and contrast improves. Furthermore, if we minimize the energy of the psf outside the cyst boundary and increase the

energy of the psf inside the cyst boundary, contrast will improve even more dramatically. The LCLS and QCLS methods described above minimize the psf energy outside a specified boundary subject to a linear constraint on the weights or a quadratic constraint on the weights, respectively. Thus cystic contrast will be improved by using optimal apodization profiles.

The LCLS apodization profiles produce psfs with narrow mainlobes and minimum sidelobe energy. These profiles seem to break the governing rule of windowing in signal processing: in order to achieve lower sidelobes the mainlobe must broaden, a result exhibited by traditional apodization functions. Therefore, the LCLS psfs are more attractive for point imaging in general ultrasound applications, not only imaging anechoic lesions. Although the LCLS design approach improves cystic resolution, it is not truly optimal for imaging diffuse lesions and low echogenicity cysts. In these cases a broader mainlobe may be desirable. Such profiles can be designed using the QCLS approach.

### B. Enhanced Depth of Field

The depth of field (DOF) of an ultrasound imaging system is generally defined as the axial region over which the system is in focus, or the axial region over which the system response remains similar to the psf at the focus. Current methods to improve DOF include transmitting at a high f/#, dynamically receiving at low f/#'s, and dynamic receive apodization [41]. The implementation of these techniques lacks formal theory describing effectiveness in improving DOF. Application of the CLS algorithms at every range yields receive weightings that force the psf at each interrogated range to have a specific mainlobe width and the lowest possible sidelobe energy outside that mainlobe. Applying dynamic receive apodization with these weightings will produce similar psfs in range and improve the DOF.

### C. Optimal Apodization for Harmonic Imaging

The linear algebra formulation of the psf requires linear superposition on receive but places no linearity constraint on transmit. Conventionally, ultrasound imaging systems assume that the propagation of the sound pulse on transmit is linear and that the receive signal has the same frequency content as that of the transmitted pulse. However, the propagation process is substantially nonlinear and it is possible to receive echoes whose energy content is shifted to harmonics of the fundamental transmit frequency. Imaging with these higher harmonic echoes can improve contrast and resolution in the resulting images. Our CLS techniques can be adapted to calculate receive apodization profiles that take nonlinear propagation into account. The nonlinear propagation of the transmit beam can be determined analytically, experimentally, or through simulation and substituted into the linear algebra formulation of the psf. Assuming linear propagation on receive, the algorithm will design receive aperture functions that minimize the energy of the two-way psf outside a specified boundary. Equation 7 which is rewritten below, describes the relationship between the harmonic imaging scenario and the receive aperture weightings which will minimize the sidelobe energy of the psf. Note that the propagation matrix $S$ will have to take into account the nonlinear propagation effects of the transmit acoustic beam:

$$w_{opt} = (S^T S)^{-1} C [C^T (S^T S)^{-1} C]^{-1} .$$

### D. Arbitrary psf shapes for general imaging, hyperthermia or Doppler applications

In some scenarios it may be more important to achieve psfs with greater sidelobe rolloff. The weighted CLS formulations described above can achieve such system responses by incorporating

a weight function that increases with distance from the mainlobe. It is also possible with the weighted CLS algorithms to design psfs with localized areas of reduced energy. It should be noted that we focused on producing apodizations that minimized the psf energy in the region lying outside a (typically spherical) void. This procedure was implemented in order to optimize cystic resolution. However, there is no need that the mainlobe and sidelobe regions be delineated according to the shape of a cyst. The CLS formulations can be adapted to design optimal psfs for a variety of ultrasound applications.

In ultrasound hyperthermia procedures, where control of the acoustic energy delivered to the tissue is of great concern [19], designing psfs with multiple mainlobes or "hot spots" while minimizing energy transfer at other locations could improve treatment efficacy as well as shorten treatment times. It is possible with the CLS formulation to specify regions of the psf where delivered energy should be maximized while at the same time specifying regions where acoustic energy should be minimized. In the LCLS design case, the linear constraint could be augmented to constrain the peak gain at a number of point locations, which would result in the $C^T$ vector of (6) becoming a matrix whose row size corresponded to the number of hot spots. The QCLS algorithm may produce even better results for this scenario since the quadratic constraint could be modified to include all regions where the energy of the psf should be constant.

Many authors have considered the issue of improving the estimation of the blood flow velocity vectors by modulating the acoustic beam in the azimuthal direction using the receive apodization function and using an autocorrelation estimator to determine the lateral velocity [42], [43]. Similar CLS formulations could be designed in order to produce apodization profiles that generate psfs with modulation in the azimuthal direction as well as the elevation dimension.

These apodization profiles may be able to produce spatial modulation frequencies higher than those previously produced, reducing the variance of the lateral motion estimates [44].

**DISCUSSION**

CLS apodization design is a general formulation for designing mathematically optimal system responses. We describe formulation of this approach for a variety of imaging applications. The required propagation functions can be determined through experiments, simulations, or theory.

Implementing CLS apodization is conceptually and practically simple. Apodization weights could be pre-calculated and stored for the intended application, then retrieved from a look up table during imaging. Current systems already employ dynamic apodization, so implementing the CLS profiles on clinical scanners should be straightforward. However, in order for CLS apodization to be implemented on a clinical system, thorough characterization of the system is required, including the shift variance of the system response. Depending on the system the degree of spatial variance in the impulse response may be great or could be neglected. Either way, once the system has been well characterized our algorithms save a great deal of development time by obviating iterative design.

For cyst imaging, successive imaging with apodization profiles corresponding to all different design cyst radii would be impractical. The question becomes, "which apodization profiles should be used?" Simulation results, presented in an accompanying paper [2], show that CLS apodization profiles are relatively stable across a range of cyst sizes. In fact, profiles calculated for specific cyst radii outperform conventional windows at all cyst sizes. Choosing

the appropriate apodization profile is straightforward when analyzed with the cystic resolution metric. Each apodization yields a contrast curve as a function of cyst radius, and therefore choosing the optimal profile simply requires selecting the apodization that achieves a specified level of contrast for the smallest cyst, or choosing the profile that yields the best contrast for a given cyst size.

The authors acknowledge that the resolution metric, while greatly improving theoretical design considerations, still has some shortcomings. The most worrisome is that the metric describes contrast at a given point in space at a specific instant in time. The metric quantifies contrast of the cyst center versus the background, not the overall cystic contrast. Incorporating detection algorithms, where contrast is defined relative to a speckle region, such as those presented in [45] and [46] may be necessary. This notion raises further questions regarding cyst detectability and observer efficiency [47]. Which cyst is easier to detect: (1) a cyst with well defined boundaries but low overall contrast, or (2) a cyst with blurred edges but greater maximum contrast? A simple one dimensional analysis yields some insights (Fig. 2).

If we view image formation as a simple convolution between the impulse response of the imaging system and the target function, then the CLS algorithms produce two very different results. In one dimension the cyst is modeled as a rect function subtracted from a constant i.e. (1−rect). In the LCLS case, the psf may resemble a triangle function whose base corresponds to the width of the cyst. The resulting image of this cyst will be a smooth Gaussian like function. Note that in Fig. 2 that the resulting convolutions are not to scale with the original inputs. In the QCLS case, the cyst remains the same but the psf resembles a rect function whose width corresponds to the size of the cyst. The resulting image of the cyst will be a triangle function whose negative peak is deeper than that of the smooth Gaussian resulting from the LCLS

apodized psf. It is not obvious which cyst would be more readily detectable. One has sharper edges (LCLS) but the other has a greater maximum contrast. This effect was also seen in Johnson's analysis comparing Hamming and flat apodization [32]. We hope to explore this issue through a human observer study where detection of cysts using the CLS apodization profiles will be investigated.
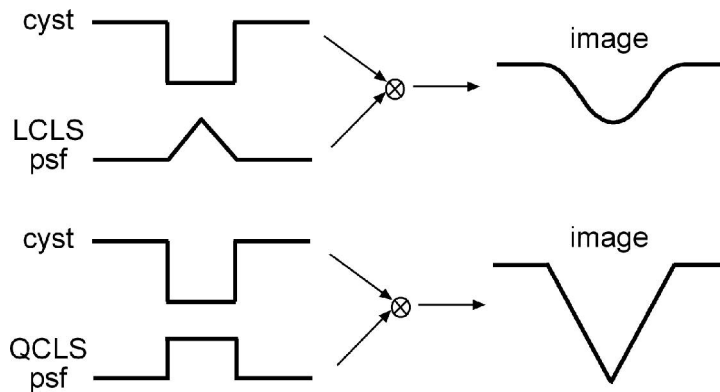


Fig. 2. One dimensional representation of imaging a cyst with the two CLS psfs. In the LCLS case the resulting image of the cyst has sharper defined edges. In the QCLS case the resulting image has blurred edges but more overall contrast than the LCLS imaged cyst.

The design method described here is different than that described in [24] for several reasons. First, we do not require a goal psf in our minimization. Second, our method is considerably easier to implement for broadband imaging systems, while still taking into account the 4 dimensional spatio-temporal nature of the psf. Another difference is that the algorithm described by Ranganathan has no constraints on the design weights which could lead to instability of the results. Our algorithm is similar to the MSSE method described by Ranganathan in that it is general enough to apply to both one way and two way responses, continuous wave and broadband operations, and can be used to design apertures for a variety of

applications. Another similarity is that the entire psf is used to obtain a least squares solution to an overdetermined system of equations.

Our method of apodization profile design for coherent imaging systems is similar to many previously described array pattern synthesis techniques. The LCLS formulation is similar to the array pattern synthesis technique by Tseng [8], however we use a broadband formulation, a different linear constraint on the weights, and our algorithm does not require iterations to achieve an optimum. This QCLS formulation is similar to the constrained eigenfilter design [10], [26]; however, we use a broadband formulation and a quadratic constraint on the energy in the psf.

Keitmann-Curdes *et al.* [27] used a formulation similar to our QCLS formulation in designing optimal apodizations in simulated ultrasound fields. However, their method minimized the energy in the sidelobes of the system response over time. The use of space-time psfs in their model neglects the inherent shift variant properties of the imaging system and integrating the pressure field power over the time axis is not a realistic measure of the system's spatial impulse response. Finally Schwann *et al.* elegantly used two different resolution criteria to design frequency dependent receive apodization profiles [28]. Their resolution criteria: maximum to average ratio and the fill-in measure relate directly to cystic contrast. However, their multiple objective formulation requires computationally expensive iterative methods to arrive at one Pareto optimum solution. Furthermore, given a Pareto optimal frontier, a curve of all the Pareto optimal solutions as a function of the objectives, for the maximum to average ratio versus fill-in criteria, it is unclear as to what point on that curve is truly optimal for clinical ultrasound imaging. The contrast curves we produce using the cystic resolution metric on the other hand, provide a straightforward approach for parameter optimization.

Our method offers an elegant path for optimizing the ultrasound system's psf and has potential application to apodization design for many varied applications. Overall, the CLS apodization design technique has the potential to improve the contrast of anechoic legions and improve beamforming in general by forming psfs with narrow mainlobes and low sidelobes. The technique may also aid in the design of system responses used for hyperthermia applications and Doppler signal processing. Stability of the CLS algorithms in the presence of sound speed errors as well as changing system parameters needs to be investigated. Simulation results addressing these issues for the CLS apodization design technique and its applications are described in an accompanying paper [2]. Results show that CLS apodization profiles improve cystic contrast compared to many conventional windows as well as improve DOF.

**Conclusion**

The CLS apodization design technique presented in this paper is a general beamforming method that can be used to design apertures for specific applications. It achieves mathematically optimal cystic contrast by designing mathematically optimal aperture weights for a given system. The contrast is optimized because the weights minimize the energy of the psf outside the specified cyst boundary while either maintaining peak gain inside the cyst (LCLS) or maintaining constant psf energy inside the cyst (QCLS). The CLS apodization design technique also has the potential to improve point resolution by forming psfs that have narrower mainlobes and lower sidelobes than psfs generated from conventional windows. Therefore, we believe the CLS apodization design algorithms have significant potential to improve ultrasound beamforming and can be applied in any ultrasound application where the system response is well characterized.

**REFERENCES**

[1] K. Ranganthan and W. F. Walker, "A General Cystic Resolution Metric for Medical Ultrasound," submitted to the *IEEE Transactions on Ultrasonics, Ferroelectrics, and Frequency Control*.

[2] D. A. Guenther and W. F. Walker, "Optimal Apodization Design for Medical Ultrasound using Constrained Least Squares. Part II: Simulation Results," submitted to the *IEEE Transactions on Ultrasonics, Ferroelectrics, and Frequency Control*.

[3] C. L. Dolph, "A current distribution for broadside arrays which optimizes the relationship between beamwidth and sidelobe level," *Proc. IRE*, vol. 34, pp. 335-348, 1946.

[4] T. T. Taylor, "Design of line source antennas for narrow beamwidth and low sidelobes," *IRE Trans. Antennas Propagat.*, vol. AP-3, pp. 16-28, 1955.

[5] A. T. Villeneuve, "Taylor Patterns for Discrete Arrays," *IEEE Trans. Antennas Propagat.*, vol. 32, no. 10, pp 1089-1093, 1984.

[6] A. H. Nuttall, "Some Windows with Very Good Sidelobe Behavior." *IEEE Trans. Acoust. Speech Signal Process.*, vol. 29, no. 1, pp. 84-91, 1981.

[7] C. A. Olen and R. T. Compton, Jr., "A Numerical Pattern Synthesis Algorithm for Arrays," *IEEE Trans. Antennas Propagat.*, vol. 38, no. 10, pp. 1666-1676, 1990.

[8] C.-Y Tseng and L. J. Griffiths, "A Simple Algorithm to Achieve Desired Patterns for Arbitrary Arrays*," IEEE Trans. Signal Proc.*, vol. 40, no. 11, pp. 2737-2746, 1992.

[9] I. W. Selesnick, M. Lang, and C. S. Burrus, "Constrained Least Square Design of FIR Filters without Specified Transition Bands," *IEEE Trans. Signal Proc.*, vol. 44, no.8, pp. 1879-1892, 1996.

[10] Y.-M. Law and C.-W. Kok, "Constrained Eigenfilter Design Without Specified Transition Bands," *IEEE Trans. On Circuits and Systems-II: Express Briefs*, vol. 52, no. 1, pp. 14-21, 2005.

[11] S.-C. Pei and J.-J. Shyu, "2-D FIR Eigenfilters: A Least-Squares Approach," *IEEE Trans. Circuits and Systems*, vol. 37, no. 1, pp. 24-43, 1990.

[12] P. P. Vaidyanathan and T. Q. Nguyen, "Eigenfilters: A New Approach to Least-Squares FIR Filter Design and Applications Including Nyquist Filters*," IEEE Trans. Circuits and Systems*, vol. 34, no. 1, pp. 11-23, 1987.

[13] M. H. Er, "Array Pattern Synthesis with a Controlled Meas-Square Sidelobe Level," *IEEE Trans. Signal Proc.*, vol. 40, no. 4, pp. 977-981, 1992.

[14] S. L. Sim and M. H. Er, "Constrained optimization technique for general array pattern synthesis," *Electronics Letters*, vol. 32, no. 10, pp. 861-862, 1996.

[15]    M. H. Er, S. L. Sim, and S. N. Koh, "Application of constrained optimization techniques to array pattern synthesis," *Signal Processing*, vol. 34, pp. 323-334, 1993.

[16]    M. H. Er, "On the Limiting Solution of Quadratically Constrained Broad-Band Beam Formers," *IEEE Trans. Signal Proc.*, vol. 41, no. 1, pp. 418-419, 1993.

[17]    S. L. Sim and M. H. Er, "Sidelobe suppression for general arrays in presence of element failures," *Electronics Letters*, vol. 33, no. 15, pp. 1278-1280, 1997.

[18]    B.P. Ng, M. H. Er, and C. Kot, "Linear array geometry synthesis with minimum sidelobe level and null control," *IEE Proc. Microw. Antennas Propagat.*, vol. 141, no. 3, pp. 162-166, 1994.

[19]    E. S. Ebbini and C. Cain, "Multiple-focus ultrasound phased-array pattern synthesis: Optimal driving-signal distributions for hyperthermia," *IEEE Trans. Ultrason. Ferroelect.,and Freq. Contr.*, vol. 36, no. 5, pp. 540-548, 1989.

[20]    P.-C. Li, S. W. Flax, E. S. Ebbini, and M. O'Donnell, "Blocked element compensation in phased array imaging*," IEEE Trans. Ultrason. Ferroelect., and Freq. Contr.*, vol. 40, no. 4, pp. 283-292, 1993.

[21]    B. Mandersson and G. Salomonsson, "Weighted Least-Squares Pulse-Shaping Filters with Application to Ultrasonic Signals," *IEEE Trans. Ultrason. Ferroelect., and Freq. Contr.*, vol. 36, no. 1, pp. 109-113, 1989.

[22]    W. Wilkening, B. Brendel, H. Jiang, J. Lazenby, and H. Ermert, "Optimized Receive Filters and Phase-Coded Pulse Sequences for Contrast Agent and Nonlinear Imaging," *Proc. IEEE Ultrason. Symp.*, pp. 1733-1737, 2001.

[23]    W. Wilkening, B. Brendel, C. Hansen, and H. Ermert, "Optimized Filters for Dynamic RF Echo Blending in Multiple Focal Zone Imaging," *Proc. IEEE Ultrason. Symp.*, pp. 1729-1732, 2004.

[24]    K. Ranganathan and W. F. Walker, "A novel beamformer design method for medical ultrasound.  Part I: Theory*," IEEE Trans. Ultrason., Ferroelect., and Freq. Contr.*, vol. 50, no. 1, pp. 15-24, 2003.

[25]    K. Ranganathan and W. F. Walker, "A novel beamformer design method for medical ultrasound.  Part II: Results," *IEEE Trans. Ultrason., Ferroelect., and Freq. Contr.*, vol. 50, no. 1, pp. 25-39, 2003.

[26]    S. Docolo and M. Moonen, "Design of far-field and near-field broadband beamformers using eigenfilters," *Signal Processing*, vol. 83, pp. 2641-2673, 2003.

[27]    O. Keitmann-Curdes, B. Brendel, C. Marg, and H. Ermert, "Optimization of Apodization Based on the Sidelobe Pressure Energy in Simulated Ultrasound Fields," *Proc. IEEE Ultrason. Symp.*, pp. 1677-1680, 2002.

[28]    R. Schwann, N. Stache, and T. G. Noll, "Optimization of Frequency Dependent Receive Apodization," presented at the *2005 IEEE International Ultrasonics Symposium*, 18-21 Sept. 2005, Rotterdam, The Netherlands.  In press.

[29]    M. D. Intriligator, *Mathematical Optimization and Economic Theory*. Pennsylvania: Society for Industrial and Applied Mathematics, 2002, p. 258.

[30]    B. D. Steinberg, *Principles of Aperture and Array System Design*, John Wiley & Sons, 1976, pp. 40-52.

[31]    D. Vilkomerson, J. Greenleaf, and V. Dutt, "Towards a resolution metric for medical ultrasonic imaging," *Proc. IEEE Ultrason. Symp.*, vol. 2, pp. 1405-1410, 1995.

[32]    R. Johnson, "Contrast Response Analysis for Medical Ultrasound Imaging," *IEEE Trans. Ultrason., Ferroelect., and Freq. Contr.*, vol. 44, no. 4, pp. 805-809, 1997.

[33]    K. F. Üstüner and G. L. Holley, "Ultrasound Imaging System Performance Assessment," presented at the *2003 AAPM Annual Meeting*.

[34]    J. W. Goodman, *Introduction to Fourier Optics, 3rd ed*. Colorado: Roberts & Company, 2005.

[35]    A. R. Selfridge, G. S. Kino, and B. T. Khuri-Yakub, "A theory for the radiation pattern of a narrow-strip acoustic transducer," Appl. Phys. Lett., vol. 37, no. 1, pp.35-36, 1980.

[36]    L. L. Scharf, Statistical Signal Processing: Detection, Estimation, and Time Series Analysis, Addison-Wesley Publishing Company, 1991, p.365.

[37]    Y. Y. Haimes, *Risk Modeling, Assessment, and Management, 2nd ed.* John Wiley and Sons, Inc., 2004.

[38]    G. H. Golub and C. F. Van Loan, *Matrix Computations, 3rd ed.* Baltimore: The Johns Hopkins University Press, pp. 375-378, 1996.

[39]    W. H. Gander, "Least Squares with a Quadratic Constraint," Numerische Mathematik, vol. 36, pp. 291-307, 1981.

[40]    A. Björck, *Numerical Methods for Least Squares Problems*. Philadelphia, Society for Industrial and Applied Mathematics, pp. 203-213, 1996.

[41]    K. Thomenius, "Evolution of ultrasound beamformers," in Proc. IEEE Ultrason. Symp., 1996, pp. 1615-1622.

[42]    J. A. Jensen and P. Munk, "A new method for estimation of velocity vectors," *IEEE Trans. Ultrason., Ferroelect., and Freq. Contr.,* vol. 45, pp. 837-851, 1998.

[43]    M. E. Anderson, "Spatial Quadrature: A novel technique for multidimensional velocity estimation," In *Proc. IEEE Ultrason. Symp.*, vol. 45, pp. 1233-1238, 1997.

[44]    W. F. Walker and G. E. Trahey, "A Fundamental Limit on Delay Estimation Using Partially Correlated Speckle Signals," *IEEE Trans. Ultrason., Ferroelect., and Freq. Contr.,* vol. 42, pp. 301-308, 1995.

[45]    S. W. Smith, R. F. Wagner, J. M. Sandrik, and H. Lopez, "Low Contrast Detectability and Contrast/Detail Analysis in Medical Ultrasound," *IEEE Trans. Sonics and Ultrason.*, vol. 30, no. 3, pp. 164-173, 1983.

[46]    S. W. Smith and H. Lopez, "A contrast-detail analysis of diagnostic ultrasound imaging," *Med. Phys.*, vol. 9, no. 1, pp. 4-12, 1982.

[47]    C. K. Abbey, R. J. Zemp, J. Liu, K. K. Lindfors, and M. F. Insana, "Observer Efficiency in Discrimination Tasks Simulating Malignant and Benign Breast Lesions Imaged With Ultrasound," *IEEE Trans. Medical Imaging*, vol. 25, no. 2, pp. 198-209, 2006.

**Optimal Apodization Design for Medical Ultrasound using Constrained Least Squares.**
**Part II: Simulation Results**
**D. A. Guenther and W. F. Walker**

**Abstract**

In the first part of this work we introduced a novel general ultrasound apodization design method using constrained least squares (CLS) [1]. The technique allows for the design of system spatial impulse responses with narrow mainlobes and low sidelobes. In the linear constrained least squares (LCLS) formulation, the energy of the psf outside a certain mainlobe boundary was minimized while maintaining a peak gain at the focus. In the quadratic constrained least squares (QCLS) formulation, the energy of the psf outside a certain boundary was minimized while the energy of the psf inside the boundary was held constant. In this paper, we present simulation results that demonstrate the application of the CLS methods to obtain optimal system responses. We investigate the stability of the CLS apodization design methods with respect to errors in the assumed wave propagation speed. We also present simulation results that implement the CLS design techniques to improve cystic resolution. According to the metric presented in [2], our apodization profiles improve cystic resolution by -3dB to -10dB over conventional apodizations such as the flat, Hamming, and Nuttall [3] windows. We also show results using the CLS techniques to improve conventional depth of field (DOF).

**Introduction**

In an accompanying paper [1], we describe two apodization design methods using a constrained least squares (CLS) formulation. The algorithms allow for the synthesis of beam patterns with a specified mainlobe width and minimum energy in the sidelobe regions. The CLS techniques express the system spatial impulse response (psf) using a linear algebra formulation

1

of the aperture weights and a propagation function. The propagation matrix uses superposition to describe the contribution of each transducer element at each field point at an instant in time and can be determined from experiment, simulation, or theory. The CLS formulations provide closed form solutions for the aperture weightings that minimize the energy of the psf outside some specified boundary subject to either a linear or quadratic constraint on the weights. A brief review of the major results derived in [1] is provided below.

*A. Linear Algebra Formulation of the Broadband Spatial Impulse Response (psf)*

The acoustic pressure field emanating from a transducer during pulse echo propagation at a single point in space at a single instant in time can be expressed as a function of a propagation matrix, *S*, and a set of receive aperture weightings, *w*. *S* can be derived from the Rayleigh-Sommerfeld diffraction equation, outlined in ([4, pp.46-50]) and may also include a term relating to limited element angular response [5] and frequency dependent attenuation. The propagation matrix can also be simulated or measured experimentally. For our formulation, *S* is a function of the transmit aperture weights, the excitation pulse, and the individual element spatial impulse responses of the transmit and receive apertures. The two way psf, *P*, is then simply the matrix multiplication between the propagation matrix and the weight vector:

$$P = Sw .$$
(1)

*B. Linearly Constrained Least Squares (LCLS) Apodization Design*

In the first CLS apodization design technique, we minimize the energy of the psf outside a certain mainlobe region. Although our formulation can account for the 4-dimensional nature of the spatio-temporal psf, we restrict our analysis to two spatial dimensions, azimuth and range,

and a single instant in time. The mainlobe region is defined by a circle of a specified radius centered at the peak of the 2D psf. We impose a linear constraint on the aperture weights in order to maintain a peak gain of the psf at the intended focus. Drawing upon [6], we can derive the least squares solution for the receive aperture weightings that produce the desired psf:

$$w_{opt} = (S^T S)^{-1} C [C^T (S^T S)^{-1} C]^{-1}, \tag{2}$$

where the superscripts T and -1 denote the transpose and matrix inverse operations, respectively. *S* represents the propagation matrix for every spatial point of the psf where energy is to be minimized and *C* is the linear constraint vector. *C* has elements corresponding to the individual amplitude response of each synthetic receive element at the intended focus.

*C. Quadratically Constrained Least Squares (QCLS) Apodization Design*

The second CLS apodization design technique minimizes the energy of the psf outside the defined mainlobe region, while maintaining constant energy of the psf inside the mainlobe region. We formulate this problem as a least squares minimization subject to a quadratic constraint on the weights. This method requires the formation of two propagation matrices. The first, $S_{out}$, represents the propagation matrix associated with every point of the psf where energy is to be minimized, as in (2) above. The second, $S_{in}$, represents the propagation matrix associated with every point of the psf lying inside the mainlobe boundary. Drawing upon [7] and [8], the set of optimal receive weightings for this scenario is given by the generalized eigenvector corresponding to the minimum generalized eigenvalue resulting from the generalized eigenvalue decomposition problem of $S_{out}^T S_{out}$ and $S_{in}^T S_{in}$:

$$S_{out}^T S_{out} w = \lambda S_{in}^T S_{in} w \ , \tag{3}$$

where the weight vector $w$ is the generalized eigenvector and $\lambda$ is the associated generalized eigenvalue.

*D. Reduced Computational Cost through Symmetry Relations*

The CLS apodization design techniques can become computationally expensive rather easily due to the large propagation matrices and the computation of the matrix inverse (only for the LCLS design case). In order to reduce this computational complexity we exploit the lateral symmetry of the aperture and the psfs that arise from symmetric, non-steered apertures [1]. Due to the symmetry relationships, we need only compute half of the aperture weights using just half of the psf, thereby enabling more efficient computation of the apodization profiles. Note that while the design of the weights is more costly computationally, the application of the weights is trivial in modern ultrasound system hardware. Once the CLS apodization profiles have been calculated, they can be stored in a lookup table and applied as dynamic apodization with range.

All the formulas for the design methods described above are thoroughly described and derived in [1]. This paper presents results of simulations that were implemented to demonstrate the validity and stability of the LCLS and QCLS apodization design techniques.

**Simulations**

In order to test our apodization design algorithms and to highlight the utility of the cystic resolution metric [2] we performed simulations using DELFI [9], a custom ultrasound simulation tool which efficiently computes spatial pulse-echo responses. All simulations were performed under MATLAB (The Mathworks, Inc., Natick, MA). Spatial pulse-echo responses were

computed by transmitting a focused wave from a subaperture of elements and synthetically receiving on each individual element. Uniform apodization was applied on transmit. Dynamic receive focusing was used to calculate multiple psfs at varying depths. The focal ranges on receive were 1cm, 1.5cm, 2cm, 2.5cm and 3cm. The psfs were computed at the instant in time corresponding to the given receive depth and over a 2D planar area in azimuth and range that encompassed the entire extent of the psf.

We simulated two different 1D linear arrays. The first array, whose system parameters are described in Table I, operated at 6.5MHz center frequency with a 50% fractional bandwidth calculated as:

$$Fractional\ BW\ (\%) = \frac{f_c}{BW} \times 100 \quad , \tag{4}$$

where $f_c$ is the center frequency of the transmitted pulse in MHz and $BW$ is the -6dB bandwidth of the pulse also in MHz. The array had fixed transmit focus at 2cm (f/2). The 6.5MHz array was used for general CLS apodization design and for the speed of sound simulations. The second array was more aggressive with a higher operating frequency of 10MHz with a 75% fractional bandwidth. We kept the transmit focus fixed at 2cm but used a larger f/# on transmit (f/4). This array was also used for apodization design and for the varying receive f/# simulations. The system parameters for the second array are described in Table II.

Constrained least squares apodization profiles were designed and analyzed for improvements in system performance relative to conventional apodization. All calculations were performed on an IBM Intellistation Z Pro (Processor speed 2.80GHz, 3.00Gb RAM). In general the CLS apodization profiles took less than two minutes of CPU time to generate, and the QCLS profiles were faster to generate than the LCLS profiles since they do not require computing a

matrix inverse. The 2D psfs generated using DELFI [9] were used to calculate the optimal

receive weights according to the CLS algorithms outlined above. CLS apodization profiles were

computed for each dynamic receive response because of the spatial shift variance of the psf with

range. The sidelobe region was defined by centering a cyst of a specified radius about the

mainlobe peak of the psf. Since this cyst specifies the mainlobe and sidelobe regions of the psf,

we call it the "design cyst." Cystic contrast, neglecting electronic SNR, was computed according

to the equation given in [2] as:

$$C = \sqrt{\frac{E_{out}}{E_{tot}}} \quad , \tag{5}$$

where $E_{out}$ is the energy of the psf outside the mainlobe boundary and $E_{tot}$ is the entire energy of

the psf. Corresponding cystic contrast curves as a function of cyst radius were calculated for the

CLS windows and compared to those for the flat, Hamming, and the Nuttall windows.

   To investigate the performance of the algorithms, we computed apodization profiles for a

large number of design cyst radii. Specifically we present results of LCLS and QCLS aperture

weights with design cyst radii from 0.1mm to 2.0mm. We also computed the weights that

minimized the mainlobe width for the LCLS design case in order to test the limits of this

particular algorithm.

   Since most commercial systems use dynamic receive focusing to improve image contrast

and extend the conventional depth of field (DOF), we investigated the stability of our algorithms

in this scenario. We calculated psfs at varying depths on receive (1.0cm, 1.5cm, 2.0cm (Tx

focus), 2.5cm and 3.0cm) and then applied the CLS algorithms on each psf. The resulting

aperture weights should improve depth of field since the goal of applying the CLS algorithms

was to make psfs with a similar mainlobe and minimum sidelobe energy.

An important system parameter that affects image quality and contrast is the f/# used on receive. It is an important parameter for a linear array because dynamic focusing schemes which maintain constant f/# throughout the image range are limited by aperture size. We investigated the impact of f/# on our CLS apodization design algorithms by computing contrast curves as a function of cyst radius for varying f/#'s.

Errors in the assumed sound wave propagation velocity adversely affect an ultrasound system's response, potentially degrading the resulting images [10]. Because our CLS technique uses dynamic shift variant aperture weights, errors in the assumed sound speed are of great concern. Therefore, we implemented simulations in which the assumed propagation speed was underestimated by 25m/s, 50m/s and 75m/s, and overestimated by 25m/s, 50m/s and 75m/s. The psfs were calculated at the intended transmit focus of 2cm, not the shifted focus. The purpose of these simulations was to investigate the robustness of our algorithm to incorrect assumptions about the wave propagation speed.

**Results**

Optimal receive apodization profiles were computed for a linear 1D array according to the CLS formulations discussed above. Cystic resolution curves were calculated in order to visualize and quantify the changes in system performance using the CLS windows compared to the conventional windows. Apodization profiles were computed for a range of design cyst radii from 0.1mm to 2.0mm. For every design cyst radius the CLS apodization profiles resulted in psfs that had lower energy in the sidelobe regions compared to the other windows.

Figure 1 shows results for the 6.5MHz simulations with a fixed transmit focus at 2cm (f/2) and dynamic receive focus at 2cm (f/1). The plot on the left shows an up close view of the

mainlobe region of the integrated lateral beamplots using different apodization schemes.  All lateral beamplots were computed by taking the square root of the energy of the 2D psf summed in range.  The CLS profiles were designed using a cyst radius of 0.6mm.  We also used the LCLS algorithm to design an apodization profile that produces a psf with the narrowest possible mainlobe.  This beamplot is the mCLS plot in figure 1 designated by a   . The full width at half maximums (FWHM), -6dB beamwidths, were 264, 304, 328, 297, 301 and 190 µm for the flat, Hamming, Nuttall, LCLS, QCLS and mCLS apodizations, respectively.  The LCLS and QCLS apodization profiles had smaller -6 dB beamwidths than all but one of the conventional windows. The LCLS and QCLS lateral beamplots have decreased sidelobe levels by about -5 dB over the Hamming window, -12 dB over the flat apodization, and almost -16 dB over the Nuttall window. The mCLS apodization lateral beamplot has the narrowest mainlobe (20% reduction compared to the flat window) but the highest sidelobe levels.  The plot on the right shows the full extent of the integrated lateral beamplots of the psfs with notable differences in the grating lobe levels.  The reduction of the sidelobe levels for the LCLS and QCLS apodization profiles did result in higher grating lobes than the Hamming and Nuttall windows but these larger grating lobes are around -60 dB, a typical noise floor for diagnostic ultrasound imaging systems [11].  The mCLS lateral beamplot shows much larger grating lobes around -40dB.

Since it is unreasonable to scan through apodization profiles for every cyst radius with conventional systems, it is interesting to monitor the behavior of the CLS apodization profiles with increasing design cyst radius.  Furthermore, using contrast curves we can easily compare the performance of the different apodization schemes and optimize based on required operation values.  In figure 2 we show the performance of both the LCLS apodization windows (left column) and the QCLS apodization windows (right column) as we increase the design cyst

radius from 0.2mm to 0.8mm in 0.2mm steps. These simulations used the 6.5MHz linear array

conditions described in Table I. The results at different dynamic receive depths were similar so

we present one set of simulation results in figure 2 corresponding to a dynamic receive depth of

1.5cm. The first row of plots, panels (a) and (b), shows the contrast curves over cyst radii from

0.1mm to 1.0mm. All curves were normalized to the flat apodization curve which is also plotted

for reference. For the LCLS windows, (a), we see a general trend of decreased contrast for the

smaller cyst sizes when increasing the design cyst radius. At the same time we see greatly

improved contrast over a large range of cyst radii for the larger design radius curves. Overall the

LCLS windows maintained relatively similar contrast curves for design cyst radii of 0.4, 0.6 and

0.8mm. These profiles improved contrast around -5 dB over the flat apodization scheme across

the range of larger cyst sizes (0.4mm-1.0mm). The QCLS contrast curves changed more than the

LCLS curves across the range of design cyst radii. Each QCLS apodization profile achieved the

best contrast of any window for the specific design radius; however the QCLS profiles suffered

greater losses in contrast for cyst sizes smaller than the design cyst radius compared to the LCLS

profiles designed for the same cyst radius. This phenomenon can be easily seen with the 0.6mm

and 0.8mm contrast curves where they decrease contrast by about +3dB compared to the flat

apodization for cyst radii smaller than 0.4mm. The second row of plots in figure 2 show the

mainlobe region of the CLS integrated lateral beamplots. The widening of the mainlobe for the

QCLS profiles is more dramatic than the LCLS profiles. This phenomenon is to be expected due

to the formulation of the QCLS algorithm, which maintains constant energy of the psf inside the

mainlobe boundary. The third row of plots, panels (e) and (f), shows the changes in the grating

lobes with different design cyst radius. The final row of plots in figure 2 shows the designed

apodization weights for each individual element. It is interesting to note that the CLS algorithms

produced profiles that have negative weights on some elements. For the most part the CLS profiles have a typical smooth, curved shape like many of the conventional windows; however, the CLS windows' behavior at the ends of the aperture is discontinuous.

In our simulations we also investigated the effects of dynamic receive focusing on the performance of the CLS algorithms. Conventional systems typically maintain a constant beamwidth over a large range by transmitting on a higher f/# and dynamically receiving with a constant, lower f/#. Since our apodization design schemes effectively control mainlobe size, we expect to see improvements in depth of field (DOF). For these simulations we used the 6.5MHz linear array setup with the fixed transmit focus at 2cm (f/2) and then we dynamically received focused data at 1cm, 1.5cm, 2cm, 2.5cm and 3cm with an f/1 aperture. CLS apodization profiles were designed with an aggressive cyst radius of 0.4mm for the psfs at each range. Figure 3 shows the results from these dynamic receive focused and apodized simulations. We only show data from dynamic receive depths of 1cm, 2cm and 3cm since the data at the two other depths showed similar trends. Figure 3 panels (a)-(c) show the contrast curves for the different apodization schemes across cyst radii. The LCLS and QCLS contrast curves for all three ranges are very similar, hence why the QCLS curve is difficult to distinguish. The reduced contrast at the 1cm and 3cm depths can be attributed to the spreading of the mainlobe away from the transmit focus. At all three ranges the CLS apodization schemes show marked contrast improvements over the flat and Nuttall apodization schemes across a large range of cyst sizes and reasonable improvements over the Hamming window at smaller cyst radii. Both the Hamming and the Nuttall window outperform the CLS apodization profiles for cyst radii greater than 0.5mm when receiving at 1cm but these improvements are a modest gain of around -2dB. Panels (d)-(f) of figure 3 show the mainlobe characteristics of integrated lateral beamplots using

the CLS apodization profiles. The dotted vertical lines on these images correspond to the cyst boundary used to design the windows. Mainlobes for the LCLS and QCLS windows are quite similar for the three different ranges. The third row of plots in figure 3 shows the designed apodization weights for the LCLS and QCLS profiles across the aperture. Note that the aperture size increases with range to maintain a constant f/# on receive. These profiles show discontinuities of the weighting function at the edges of the aperture.

In order to investigate the improvements in DOF for the CLS algorithms compared to the conventional windows, we looked at the beamwidths of the integrated beamplots at -6dB (FWHM) and -20dB. We also show images of the 2D psfs for the 6.5MHz array at each range superimposed to qualitatively depict the constant mainlobe size with range. In figure 4 we show images of the 2D psfs at each range for flat, Hamming, Nuttall, LCLS and QCLS apodization profiles. The CLS profiles were designed using a cyst radius of 0.4mm. The images are 1cm in azimuth and extend from 0.8cm to 3.2cm in range. Each image was normalized and log compressed to -60dB. The CLS apodization profiles maintain a relatively constant mainlobe size through range compared to the mainlobe spreading seen in the Hamming and Nuttall windows. The sidelobes of the CLS profiles are higher than the Hamming and Nuttall windows at the 2.5 and 3cm depths but lower than the large sidelobes evident in the flat apodization psfs. Figure 5 plots the -6dB (FWHM) and -20dB beamwidths of the psfs for the different apodizations at all five ranges. In figure 5 we see that the CLS apodization profiles maintain a relatively constant beamwidth with range compared with the Nuttall and Hamming windows. The flat apodization profile maintains a somewhat constant FWHM level across range but deviates greatly with range at the -20dB level; whereas the CLS profiles remain relatively constant.

We also produced similar images for the CLS apodization profiles using a design cyst radius of 0.6mm in figure 6. Again, the CLS apodization profiles maintain a relatively constant mainlobe size across ranges compared to the mainlobe spreading evident with the Hamming and Nuttall windows. The sidelobes of the CLS profiles are suppressed at the 2.5 and 3cm depths compared to figure 4. The QCLS psf exhibits a larger mainlobe with higher sidelobes at 1cm dynamic receive, a phenomenon due to the algorithm maintaining constant energy of the psf inside the cyst boundary. This effect is quantified in figure 7, where the QCLS profile exhibits the largest FWHM at a range of 1cm. Other than this anomaly, the CLS apodization profiles exhibit a relatively constant FWHM and -20dB beamwidth across range.

The effect of f/# on receive was investigated to test the robustness of the CLS apodization design algorithms. For these simulations we used the more aggressive 10MHz array utilizing a fixed transmit focus at 2cm (f/4) and dynamic receive focusing and apodization. F/#'s ranging from f/0.5 to f/4 were used on receive, which varied the size of the receive aperture. Therefore, CLS apodization profiles were calculated for each receive aperture using a 0.6mm design cyst radius. Figure 8 shows the results of these simulations. The data shows three different f/#'s used (f/0.5, f/2, and f/4) while dynamically receiving at 2.0cm in range. We also analyzed the CLS algorithms at 1.0cm and 3.0cm in range and they gave similar results. Panels (a)-(c) in figure 8 show the contrast curves for the different apodization profiles across a range of cyst radii. The CLS apodization profiles show modest contrast gains (-1dB to -3dB) over the flat, Hamming and Nuttall windows. The contrast improvements of the CLS windows over the conventional windows increase with increasing f/#. It is interesting to note that the Hamming and Nuttall windows have worse cystic resolution than the flat, LCLS and QCLS windows at f/2 and f/4 across the entire range of cyst radii. This is a phenomenon that we did not observe in the

previous 6.5MHz array simulations. The Hamming and Nuttall windows increase the size of the mainlobe in order to achieve sidelobe suppression; furthermore when analyzed with the cystic resolution metric the decrease in sidelobe energy of the Hamming and Nuttall psfs does not outweigh their relative increase in mainlobe width. The CLS apodization profiles on the other hand are able to maintain a narrow mainlobe width while at the same time decreasing the energy in the sidelobe region, hence improving cystic contrast. The second row of plots, (d)-(f), in figure 8 show the mainlobe region of the CLS integrated beamplots. The dotted line is the boundary of the design cyst radius of 0.6mm. We see very little difference between the two mainlobes with the QCLS mainlobe a bit wider than the LCLS mainlobe. The third row of plots in figure 8 show the weights of the CLS apodizations across the aperture. For the lower f/#'s the difference between the CLS windows are greater.

In the 10MHz simulations we calculated CLS apodization profiles for a number of different cyst radii. Through this investigation we observed a peculiar phenomenon for the QCLS algorithm for the larger design cyst radii. Because the algorithm attempts to keep the energy of the psf inside the cyst boundary constant, when larger design cyst radii are used, the QCLS weights make a psf with multiple peaks. This is equivalent to the eigenfilter design approach where the frequency response ripples in the pass band [12], [13]. Figure 9 plots (e) and (f) accurately depicts this phenomenon. This data uses the 10MHz array described in Table II with a dynamic receive focus at 1.0cm (f/2). The first row of plots, (a)-(c), shows the contrast curves for increasing design radii of 0.5mm, 1.0mm and 1.5mm respectively. Note for the larger design radii, the QCLS algorithm results in contrast improvements ranging from -5dB to -10dB but poor contrast resolution for smaller cyst sizes. Figure 9 plots (d)-(f) show the integrated beamplots for the LCLS and QCLS apodization profiles. Here we see how the QCLS algorithm

was able to achieve the dramatic contrast improvements for the larger cyst sizes by having multiple mainlobes inside the cyst boundary. Likewise, for large design radii the LCLS apodization profile results in higher sidelobes inside the boundary in order to achieve lower sidelobes outside the boundary. The modulation of the mainlobe for the QCLS beamplots would not intuitively be an "ideal" spatial response for general imaging purposes. This phenomenon is discussed later in detail in this manuscript. The third row of plots in figure 9 show the weights of the LCLS and QCLS apodization profiles across the aperture.

In our final set of simulations we investigated the sensitivity of the CLS apodization design algorithms to errors in the assumed speed of acoustic wave propagation. We performed these simulations using the 6.5MHz array with a transmit focus at 2.0cm (f/2) and a receive focus at 2.0cm (f/1). Figure 10 shows the contrast curves (left) and integrated lateral beamplots (right) for the CLS apodizations with the correct sound speed of 1545m/s. This figure should be used as a reference for the later simulation results presented in figures 11 and 12. We applied the CLS apodization profiles computed for a design radius of 1.0mm with the correct speed of sound, 1545 m/s, to the psfs obtained when the speed of sound was overestimated by 25m/s, 50m/s and 75m/s and then underestimated by 25m/s, 50m/s and 75m/s. Figure 11 shows the results for the simulations when the assumed speed of sound was overestimated. The first row of plots, (a)-(c), shows the contrast curves which were computed at the intended focus, not the shifted focus. The plateau seen in the contrast curves at the smaller cyst radii results from the psfs being shifted towards the transducer by such an extent that when computing the contrast for a small cyst, no significant psf energy lies within the boundary. The Hamming and LCLS curves are similar as are the Nuttall and QCLS contrast curves. The second row of plots in figure 11 shows the mainlobe region of the integrated lateral beamplots for the CLS apodized psfs. Panels (g)-(i) in

this figure show the entire lateral extent of the integrated beamplots where differences in the grating lobes for the CLS apodized psfs can be seen.

We also investigated the effect of underestimating the sound speed by 25m/s, 50m/s and 75m/s. These results are shown in figure 12. Plots (a)-(c) show the contrast curves computed at the intended focus, and again the same plateau is seen for the smaller cyst radii as was observed in the overestimated sound speed simulations. The Hamming and LCLS curves are similar as are the Nuttall and QCLS contrast curves. The second row of plots in figure 12 show the mainlobe region of the integrated lateral beamplots for the CLS apodized psfs. Plots (g)-(i) in this figure show the entire lateral extent of the integrated beamplots where differences in the grating lobes for the CLS apodized psfs can be seen. These results closely match those from the overestimated speed of sound simulations.

The design radius for the speed of sound simulations was 1.0mm. This cyst is larger than the design cyst radii previously used in simulation however we chose this size because the psfs shift in range by such a great deal that smaller cysts would not even be detected since they would lie outside the mainlobe of the psf. In order to be thorough, we present results showing how the contrast curves change when we apply CLS apodizations designed with smaller cyst radii (0.4mm-1.0mm). We show results for two simulations, one where the sound speed was underestimated by 25m/s and another where we have grossly overestimated the sound speed by 75m/s.

The contrast curves for the underestimated sound speed are shown in figure 13. The effects of design radius for the LCLS profiles are shown in the left panel of figure 13. The corresponding QCLS profiles are plotted on the right. The flat apodization contrast curve is plotted for reference in both plots. The QCLS contrast curves show more variability with design

radius where larger design radii achieve better contrast for larger cysts, but smaller design radii achieve better contrast for smaller cysts. The contrast curves corresponding to changing design radii with an overestimated speed of sound by 75m/s are shown in figure 14. The LCLS curves are shown on the left and QCLS curves are shown on the right. Both plots depict the flat apodization contrast curve for reference. In general the curves designed with the smaller radii result in worse contrast for cysts with radii greater than 1.0mm. The QCLS algorithm has a greater variability in achieved contrast than the LCLS algorithm. It should be noted that in both cases depicted in figures 13 and 14 the CLS apodization profiles achieve better contrast at all cyst sizes compared with the flat apodization contrast curve except the 1.0mm QCLS contrast curve for the 25m/s underestimated simulation.

We applied the CLS profiles designed with a smaller cyst radius of 0.4mm to the speed of sound simulations to see how they would compare against the conventional windows. Since the results for the underestimation and overestimation simulations were quite similar we only show the results for the overestimated speed of sound. Again the profiles computed with the correct speed of sound were applied to the psfs that resulted when the assumed sound speed was overestimated by 25m/s, 50m/s and 75 m/s. The results are shown in figure 15. Panels (a)-(c) in figure 15 show the contrast curves for these simulations, and the CLS algorithms remain stable. The QCLS and LCLS curves are quite similar with the QCLS curve being difficult to distinguish. The CLS curves do not achieve better contrast than the Hamming and Nuttall windows for the larger cyst sizes, but note the aggressive design cyst radius of 0.4mm lies in or close to the plateau region of the contrast curves. The second row of plots show the mainlobe region of the CLS apodized psfs where the vertical dotted lines delineate the design radius of 0.4mm. Both the LCLS and QCLS apodizations result in very similar lateral beamplots.

**Discussion**

Our simulations demonstrate the use of our novel strategies for designing optimal apodization profiles. In our methods we collect spatial impulse responses at the instant in time corresponding to the dynamic receive focus. We produce weights that minimize the energy of the spatial point spread function outside a selected radius from the mainlobe peak. This minimization is subject to a constraint that either forces unity amplitude gain at the peak of the response (LCLS method) or maintains constant energy of the psf inside the circular region defined by the selected radius (QCLS method). The LCLS approach in general yields a narrow mainlobe and low sidelobe levels. While such narrow mainlobes are attractive for point imaging, they may not be optimal for imaging diffuse legions and low echogenicity cysts. In these cases the QCLS approach which yields a slightly broader mainlobe and slightly higher sidelobe levels may be desirable.

While the LCLS and QCLS apodization design methods have been validated theoretically and through computer simulations, we must begin to assess their performance experimentally. Initial results are positive and suggest that the technique is quite robust, however full assessment with an experimental scanner will be necessary to fully prove their efficacy. We are currently designing such experiments, and collecting the entire data set of single channel receive spatial impulse responses is a challenging task. We will need to account for spatial variance of the psf in the lateral dimension as well as in range. Once we have fully characterized the spatial impulse response of the system, we will be able to produce CLS apodization profiles for each output image pixel, make data reconstruction seamless and rapid, and assess the performance of our algorithms to produce optimal contrast.

Our results in figure 1 demonstrate the use of the CLS apodization design algorithm in a basic system configuration. A linear array was used with a transmit frequency of 6.5MHz, a 50% fractional bandwidth, a fixed transmit focus at 2cm (f/2) and dynamic receive focus at 2cm (f/1). The LCLS approach achieved lower sidelobe levels than any of the alternative apodization profiles, with slightly higher grating lobes, and simultaneously attained a narrower mainlobe width than all but the flat apodization profile. The QCLS approach achieved a slightly wider mainlobe (301μm) than the LCLS mainlobe width (297μm) and still kept the sidelobe levels low. In the extreme case of minimizing the mainlobe width, the LCLS apodization weights achieved the narrowest FWHM of 190μm, almost 50μm smaller than the transmitted acoustic wavelength, however the resulting psf suffered from larger sidelobes and grating lobes.

Figure 2 depicts how the CLS apodization profiles changed with respect to design radius of the mainlobe region. For the LCLS profiles larger radii produced contrast curves that achieved better cystic resolution for larger cysts with minor contrast degradation for the smaller cyst sizes. The QCLS algorithm on the other hand achieved -2dB to -3dB gains in contrast for the larger cysts but suffered greater contrast losses for the smaller cyst sizes than compared to the LCLS curves. This result can be explained by the increased mainlobe size for the QCLS algorithm. Plots (g) and (h) in figure 2 show that the CLS algorithms produce apodization profiles that have a typically smooth curvature in the middle of the profile much like a Hamming or Nuttall window but the edges of the profiles were jagged and usually had larger magnitudes than would be expected. This suggests that the outside elements in the aperture contribute to the psf in such a way that they can be used to achieve a tighter mainlobe and low sidelobe levels. These apodization profile plots also show that some elements have negative weights, a phenomenon never seen in the conventional window functions.

Obviously, the CLS apodization design algorithms can only be realistically employed in a conventional system by choosing a specific design radius. While the cystic resolution metric can be employed to decide which profile can achieve the "best" contrast for a given application, i.e. imaging a cyst with a 0.4 mm radius or achieving -15 dB contrast for cysts ranging from 0.2mm to 2.0mm, the definitive optimal CLS profile is difficult to determine. We have found empirically that choosing the profile corresponding to the point where the contrast curve begins to level off results in the best contrast for the entire range of cyst sizes. Ideally, a library of CLS profiles could be constructed and specific profiles applied depending on the imaging application. A peripheral vasculature exam where contrast for larger voids would be important might use a profile designed for larger cysts, while breast imaging, where finer detail is critical might use a profile designed for a smaller cyst. Application of the CLS apodization profiles in a clinical system is an area of future development.

Figure 3 depicts the results of applying the CLS apodization profiles in a dynamic receive configuration. We maintained a constant f/# (f/1) on receive by growing our receive aperture with range. The results from these simulations show that the CLS algorithms are able to attain better contrast than the conventional windows in a dynamic receive operating condition. When we also look at the 2D psfs with range in the images from figures 4 and 6 we see the improved depth of field achieved by utilizing the CLS apodization profiles. The spreading of the mainlobe and higher sidelobe levels in the nearfield and beyond the transmit focus typical of flat apodization and the other conventional windows is mitigated by the use of the CLS technique. These qualitative observations are further corroborated by the FWHM and -20dB beamwidth plots in figures 5 and 7. The LCLS and QCLS apodization profiles maintain relatively constant beamwidths across the axial ranges investigated.

Changing the f/# on receive did not produce results that we intuitively predicted. We assumed that operating the CLS algorithms with smaller f/#'s or larger apertures would yield markedly better contrast curves than the conventional windows. Even though the CLS algorithms had more information to use in potentially achieving smaller sidelobe levels, the synthetic responses simply could not be summed together at that instant in time in order to destructively interfere. Ultimately the algorithms are still governed by diffraction. Although large gains in contrast were not achieved with smaller f/#'s, the LCLS and QCLS profiles did achieve improved contrast (-2dB to -4dB) compared to the conventional windows at the f/#'s investigated. Note that increasing the receive aperture size with range, a method typically used to maintain a constant f/# and improve DOF, is not entirely necessary with the CLS algorithms. It may be possible to use a fixed number of elements in the receive aperture at all ranges and let the algorithms control beam size. This is a method we are currently investigating.

It is important to note that our contrast analysis is for a specific instant in time, when the psf is centered directly in the middle of the cyst. For the speed of sound simulations where errors in the assumed wave propagation speed shift the psf in range, we still calculate contrast at the intended focus. Therefore the center of the cyst, which lies at the intended focus, is shifted away from the mainlobe of the psf. Furthermore, the contrast resolution metric describes the *point* contrast of an image, not the overall contrast of the cyst. Overall cystic contrast analysis requires taking a B-mode image of a cyst, integrating the intensities over the lesion and comparing this to the integrated intensity over a region of background speckle of the same size at the same depth [14], [15]. Incorporating this metric with the point resolution metric is an area of ongoing research.

The mainlobe modulation phenomenon of the QCLS algorithm seen in figure 9 is an interesting result. Notice that the shape of the QCLS apodization profiles which yield multiple mainlobe peaks are approximately sinusoidal (panels (h) and (i)). According to the Fraunhoffer approximation, which states that the spatial response of an aperture is the Fourier transform of the aperture function [16], a rectangular windowed sinusoidal aperture function should result in a lateral spatial response resembling two sinc functions (the convolution between a sinc and two impulses). These two sinc functions correspond to the two mainlobes in the responses seen in panels (e) and (f). Furthermore, note that when the frequency of the sinusoid corresponding to the aperture definition is increased (comparing panel (h) to panel (i)) the two mainlobes of the spatial response separate further in azimuth (panel (e) and (f)). This result is consistent with Fourier transform theory.

Clearly imaging with a psf that has two mainlobes should not produce an image of a cyst with -10dB contrast improvement, as the contrast curves of figure 9 panels (b) and (c) suggest. This result relates to the overall cystic contrast conundrum described above. However, there are applications where lateral modulation of the psf could prove beneficial [17], [18]. For example, such a psf could be used in Doppler ultrasound where acquiring the axial as well as lateral component of velocity can lead to more accurate estimation of the velocity vector [19]. Other applications could include designing ultrasound spatial responses for hyperthermia treatments where control over localized energy delivery is paramount [20]. We are also investigating ways to modify the QCLS apodization design formulation to reduce the modulation/multiple peak effect to an equiripple, similar to FIR filter design [21]. One possible method is to utilize the weighting function discussed and derived in [1]. Applying a weighting function to the mainlobe region of the psf that emphasizes the focal point compared to the surrounding area would yield a

psf with a single mainlobe.  Preliminary results show that the weighting can be applied to the QCLS algorithm to mitigate the multiple mainlobe effect.  The resulting QCLS weights produce psfs whose lateral beamplots are similar to the LCLS beamplots in figure 12 panels (e) and (f) with slightly higher sidelobes inside the cyst boundary.

Figures 10-15 show the results from our investigation into the stability of the CLS apodization design algorithms when the assumed speed of sound in the medium is erroneous.  The results when we underestimated the speed of sound were quite similar to the results for overestimating the speed of sound.  The plateaus in the contrast curves in figures 11 and 12 result from the psf being shifted in range to such an extent that no significant psf energy lies inside the cyst that is at the intended focus.  For large sound speed errors (1470m/s and 1620m/s) the Nuttall window achieves the best contrast for the largest range of cyst sizes.  For these cases the CLS windows achieve cystic contrast 2dB worse than the Nuttall window.  For the smaller sound errors, the CLS windows actually achieve better contrast than the Hamming and the Nuttall windows for smaller cyst sizes.  In all cases the QCLS window achieves lower grating lobes than the LCLS window for the profiles designed for a cyst radius of 1.0mm (figures 11 and 12).

Figures 13 and 14 investigate the changes in cystic contrast for sound speed errors as a function of design cyst radius.  For the most part the performance of the LCLS algorithm remains quite stable for the 1570m/s and 1470m/s degraded psfs.  Smaller design cyst radii yield lower contrast for larger cyst sizes.  The QCLS contrast curves changed more as a function of design cyst radius than the LCLS curves.  Whereas smaller design radii resulted in better contrast for smaller cysts with the QCLS algorithm, the four LCLS profiles achieved similar contrast across the range of smaller cyst radii.

The CLS profiles designed with a smaller radius of 0.4mm achieved great contrast improvements (Fig. 3), however in the presence of sound speed errors (Fig. 15) the Nuttall window performs better.  Yet, with the correct speed of sound, the Nuttall window had the worst contrast for cyst sizes up to 0.8mm.  We argue that the -10dB contrast improvement of the CLS windows around the 0.4mm cyst radius when the correct speed of sound was used outweigh the degraded contrast results of the sound speed trials in figure 15.  These simulations address the concerns that the variation of sound speed in human tissues will degrade the CLS profiles.  We have shown that the CLS algorithms remain relatively stable in the presence of wave propagation speed errors, but ultimately these results must be tested experimentally.

Results presented in this paper show that the CLS algorithms for apodization design outperform conventional windows such as the Hamming, Nuttall, and flat apodizations across a range of imaging scenarios and system parameters.  The contrast curve results must be interpreted with caution because the resolution metric used to compute the cystic contrast is a point contrast value not the contrast of the overall anechoic region compared to the background speckle.  We intend to perform human observer studies that will further investigate the use of the CLS apodization profiles for optimal cystic contrast, and based on the simulation results presented we believe that the CLS windows will meet our expectations.  Overall the CLS apodization design technique has the potential to improve contrast of anechoic legions but also improve beamforming in general due to the formation of psfs that have narrower mainlobes and lower sidelobes than the conventional windows.  There also exists the potential for the technique to aid in the design of system responses used for hyperthermia applications and Doppler signal processing.  In order for our technique to be implemented on a clinical system, adequate characterization of the system is required, including the shift variance of the psf.  However, once

the system has been characterized our algorithms save a great deal of time by obviating iterative design.

**Conclusion**

The CLS array pattern synthesis technique presented in this paper has been shown to be effective in designing apodization profiles that can improve contrast in ultrasound images. The LCLS approach achieved a 2D spatial impulse response with a narrower mainlobe and lower sidelobes than conventional windows currently used to reduce clutter. In cases where imaging cysts or anechoic regions are of importance and a wider mainlobe may improve cystic resolution the QCLS technique can be used for improved contrast. We have shown that our algorithms are stable across imaging scenarios such as dynamic receive focusing, varying f/#, and different transmit frequencies. The LCLS and QCLS algorithms also improved DOF by maintaining relatively constant beamwidths through range. In cases where the wave propagation speed is different than the assumed sound speed, the algorithms remain stable and can still improve contrast. Simulation results obtained by implementing the CLS algorithms demonstrate the success of the technique in solving common problems associated with ultrasound imaging, such as a restricted depth of field.

The CLS apodization design algorithms have significant potential to improve ultrasound beamforming and can be applied in any ultrasound application where the system response is well characterized. There is no iteration involved in producing the apodization profiles; therefore, design time is considerably reduced as compared to other optimal apodization design techniques. Further investigation is required to examine the effects of phase aberration, blocked elements, shift variance of the system response, and overall cystic contrast. However, our simulations

indicate that the CLS techniques improve cystic resolution and consistently outperform current

conventional apodization profiles.

**REFERENCES**

[1] D. A. Guenther and W. F. Walker, "Optimal Apodization Design for Medical Ultrasound using Constrained Least Squares. Part I: Theory," submitted to the *IEEE Transactions on Ultrasonics, Ferroelectrics, and Frequency Control*.

[2] K. Ranganthan and W. F. Walker, "A General Cystic Resolution Metric for Medical Ultrasound," submitted to the *IEEE Transactions on Ultrasonics, Ferroelectrics, and Frequency Control*.

[3] A. H. Nuttall, "Some Windows with Very Good Sidelobe Behavior." *IEEE Trans. Acoust. Speech Signal Process.*, vol. 29, no. 1, pp. 84-91, 1981.

[4] J. W. Goodman, *Introduction to Fourier Optics, 3rd ed*. Colorado: Roberts & Company, 2005.

[5] A. R. Selfridge, G. S. Kino, and B. T. Khuri-Yakub, "A theory for the radiation pattern of a narrow-strip acoustic transducer," Appl. Phys. Lett., vol. 37, no. 1, pp.35-36, 1980.

[6] L. L. Scharf, Statistical Signal Processing: Detection, Estimation, and Time Series Analysis, Addison-Wesley Publishing Company, 1991, p.365.

[7] S. Docolo and M. Moonen, "Design of far-field and near-field broadband beamformers using eigenfilters," *Signal Processing*, vol. 83, pp. 2641-2673, 2003.

[8] W. H. Gander, "Least Squares with a Quadratic Constraint," Numerische Mathematik, vol. 36, pp. 291-307, 1981.

[9] W. F. Walker, "A Spline Based Approach for Computing Spatial Impulse Responses," submitted to the *IEEE Transactions on Ultrasonics, Ferroelectrics, and Frequency Control*.

[10] M. E. Anderson, "The impact of sound speed errors on medical ultrasound imaging," *J. Acoust. Soc. Amer.*, vol. 107, no. 6, pp. 3540-3548, 1997.

[11] J. T. Bushberg, J. A. Seibert, E. M. Leidholt, Jr., and J. M. Boone, *The Essential Physics of Medical Imaging, 2nd ed.* New York: Lippincott, Williams, and Wilkins, 2002, pp. 506-508.

[12] Y.-M. Law and C.-W. Kok, "Constrained Eigenfilter Design Without Specified Transition Bands," *IEEE Trans. On Circuits and Systems-II: Express Briefs*, vol. 52, no. 1, pp. 14-21, 2005.

[13] S.-C. Pei and J.-J. Shyu, "2-D FIR Eigenfilters: A Least-Squares Approach," *IEEE Trans. Circuits and Systems*, vol. 37, no. 1, pp. 24-43, 1990.

[14] S. W. Smith, R. F. Wagner, J. M. Sandrik, and H. Lopez, "Low Contrast Detectability and Contrast/Detail Analysis in Medical Ultrasound," *IEEE Trans. Sonics and Ultrason.*, vol. 30, no. 3, pp. 164-173, 1983.

[15]  S. W. Smith and H. Lopez, "A contrast-detail analysis of diagnostic ultrasound imaging," *Med. Phys.*, vol. 9, no. 1, pp. 4-12, 1982.

[16]  J. W. Goodman, *Introduction to Fourier Optics, 3ʳᵈ ed*. Colorado: Roberts & Company, 2005.

[17]  J. A. Jensen and P. Munk, "A new method for estimation of velocity vectors," *IEEE Trans. Ultrason., Ferroelect., and Freq. Contr.,* vol. 45, pp. 837-851, 1998.

[18]  M. E. Anderson, "Spatial Quadrature: A novel technique for multidimensional velocity estimation," In *Proc. IEEE Ultrason. Symp.*, vol. 45, pp. 1233-1238, 1997.

[19]  W. F. Walker and G. E. Trahey, "A Fundamental Limit on Delay Estimation Using Partially Correlated Speckle Signals," *IEEE Trans. Ultrason., Ferroelect., and Freq. Contr.,* vol. 42, pp. 301-308, 1995.

[20]  E. S. Ebbini and C. Cain, "Multiple-focus ultrasound phased-array pattern synthesis: Optimal driving-signal distributions for hyperthermia," *IEEE Trans. Ultrason. Ferroelect.,and Freq. Contr*., vol. 36, no. 5, pp. 540-548, 1989.

[21]  I. W. Selesnick, M. Lang, and C. S. Burrus, "Constrained Least Square Design of FIR Filters without Specified Transition Bands," *IEEE Trans. Signal Proc*., vol. 44, no.8, pp. 1879-1892, 1996.

**TABLE I**

**Parameters Used in General CLS Apodization Design and Speed of Sound Simulations**

| Parameter | Value |
|---|---|
| Number of Elements | 192 |
| Element Pitch | 200 μm |
| Focus | 2.0 cm |
| psf window lateral sampling interval | 34 μm |
| psf window axial sampling interval | 20 μm |
| Ultrasonic wave propagation speed | 1545 m/s |
| Frequency | 6.5 MHz |
| Fractional Bandwidth | 50% |

**TABLE II**

**Parameters Used in General CLS Apodization Design and F/# Simulations**

| Parameter | Value |
|---|---|
| Number of Elements | 192 |
| Element Pitch | 150 μm |
| Focus | 2.0 cm |
| psf window lateral sampling interval | 25 μm |
| psf window axial sampling interval | 20 μm |
| Ultrasonic wave propagation speed | 1545 m/s |
| Frequency | 10 MHz |
| Fractional Bandwidth | 75% |
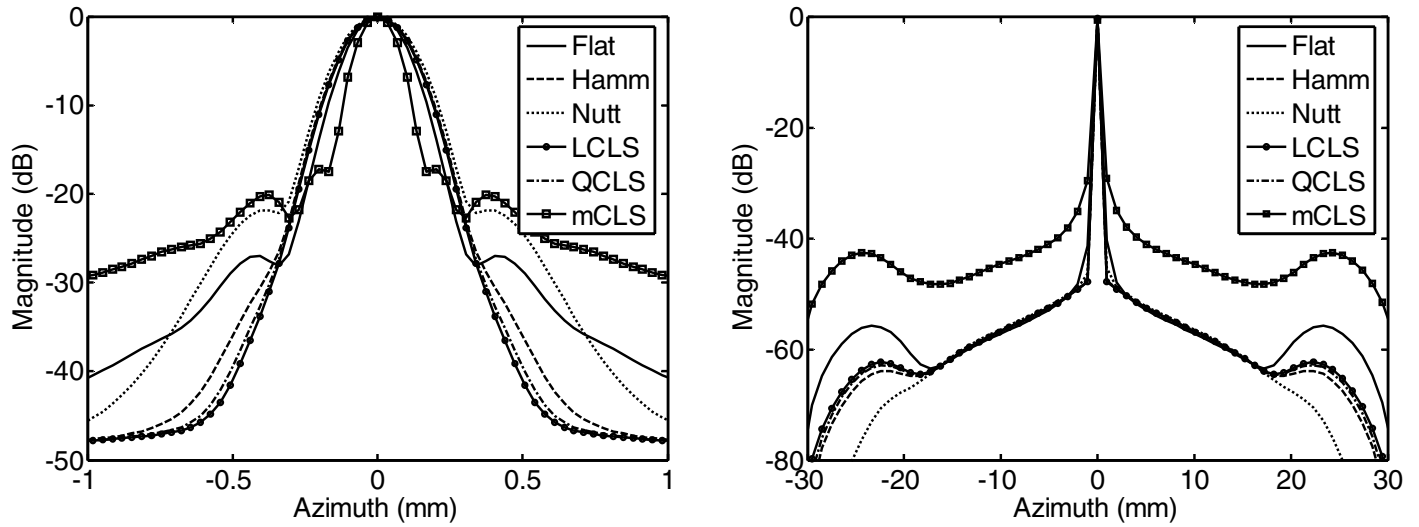
Fig. 1. Integrated lateral beamplots for different apodization schemes with the 1D Linear array operating at 6.5MHz center frequency, fixed Tx focus at 2cm (f/2) and dynamically focused on Rx at 2cm (f/1). The LCLS and QCLS profiles were designed with a cyst radius of 0.6mm. Note that the LCLS and QCLS profiles yield sidelobe levels lower than and mainlobe levels comparable to all other apodizations.

**LCLS**

**QCLS**



**(a)**



**(b)**



**(c)**



**(d)**

**(e)**



**(f)**



**(g)**



**(h)**
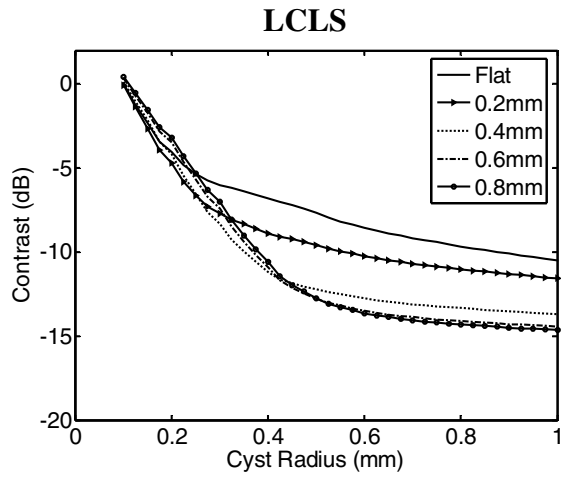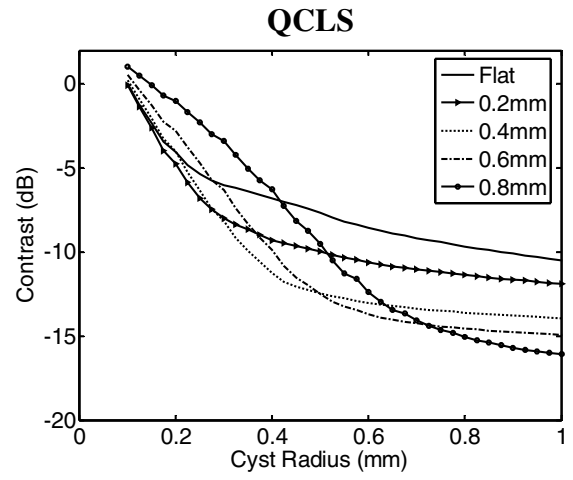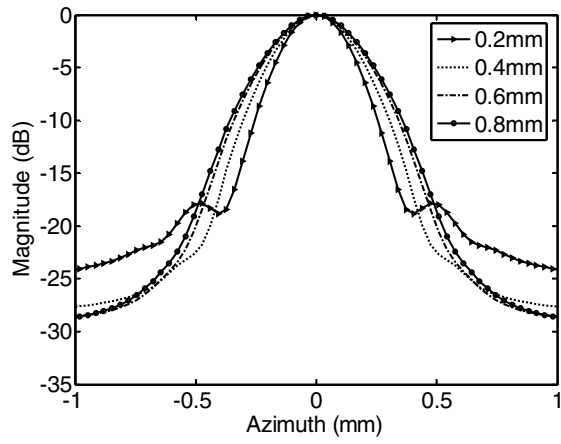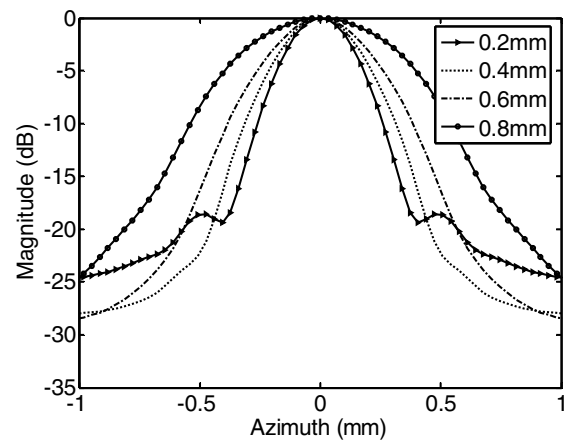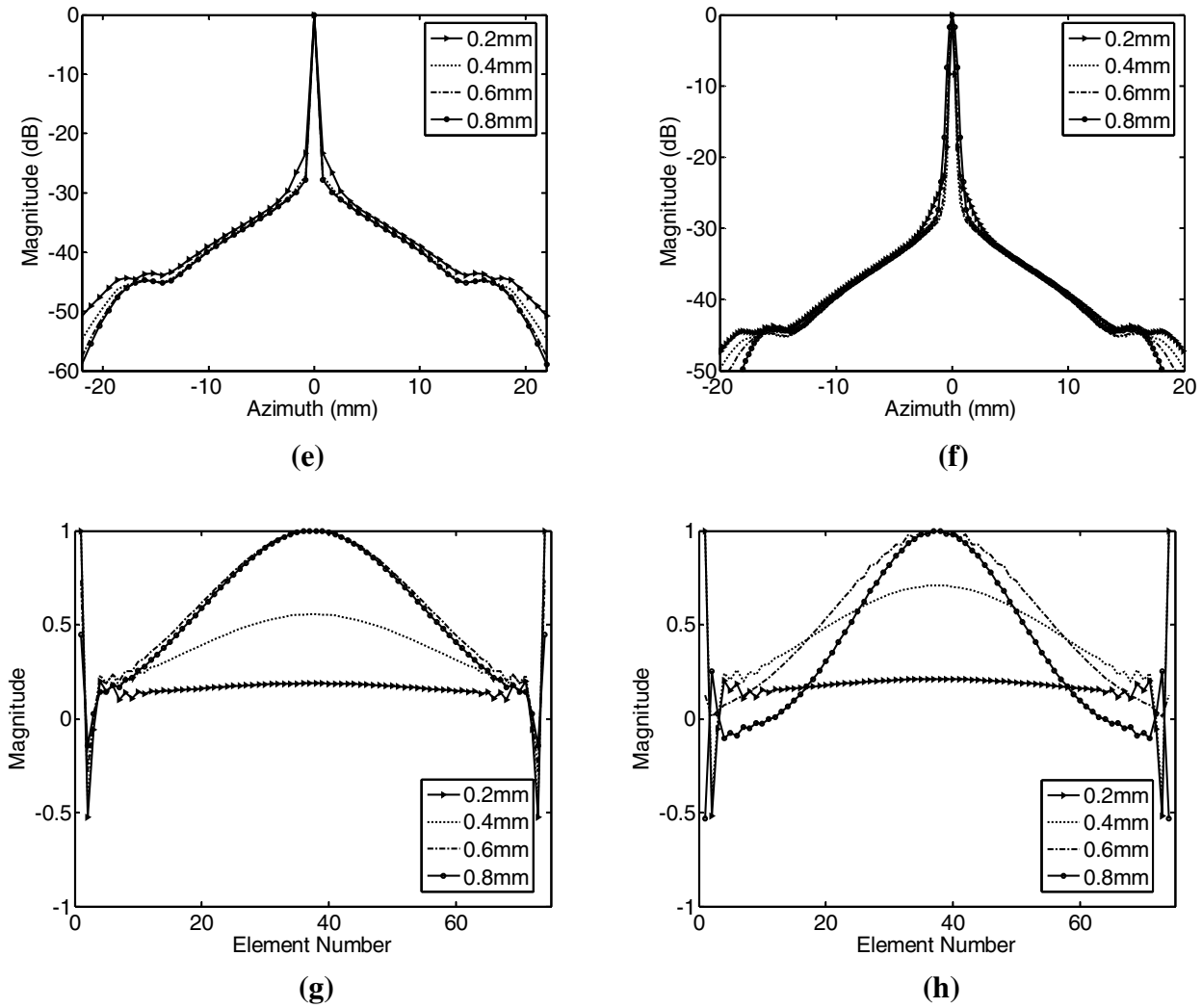
Fig. 2. Comparison of CLS apodization given different design cyst radii. The entire left column of this figure corresponds to the LCLS algorithm and the right column corresponds to the QCLS algorithm. (a) and (b) show the associated contrast curves over a range of cyst sizes compared to the flat apodization profile. Panels (c) and (d) show the mainlobe behavior of the CLS windows, and the third row, panels (e) and (f), gives the full range of the integrated lateral beamplots. (g) and (h) plot the apodization profile versus element number. Note how the mainlobe width trends with increasing design radius are indicative of the contrast performance between the two algorithms.
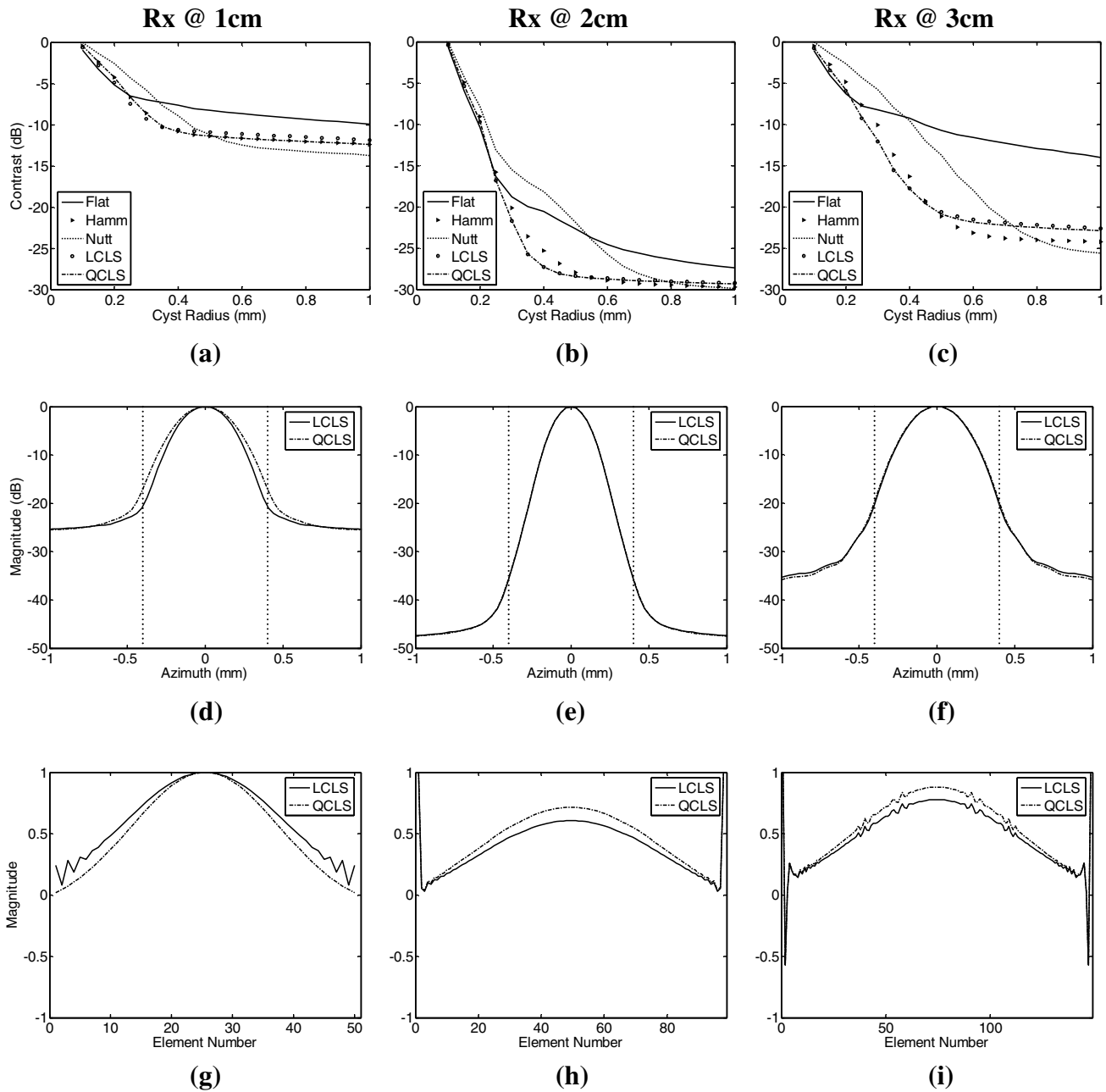
Fig. 3. Comparison of apodization profiles at different dynamic receive foci of 1cm, 2cm and 3cm and constant f/# (f/1). Panels (a)-(c) show contrast curves for the different apodization schemes (flat, Hamming, Nuttall, LCLS and QCLS). The second row of plots, (d)-(f), show the integrated beamplots of the CLS profiles where the dotted line corresponds to the cyst boundary used to design the windows. Plots (g)-(i) show the magnitude of the CLS profiles across the aperture. The CLS profiles improve contrast over a range of smaller cysts at all dynamic receive focal depths.
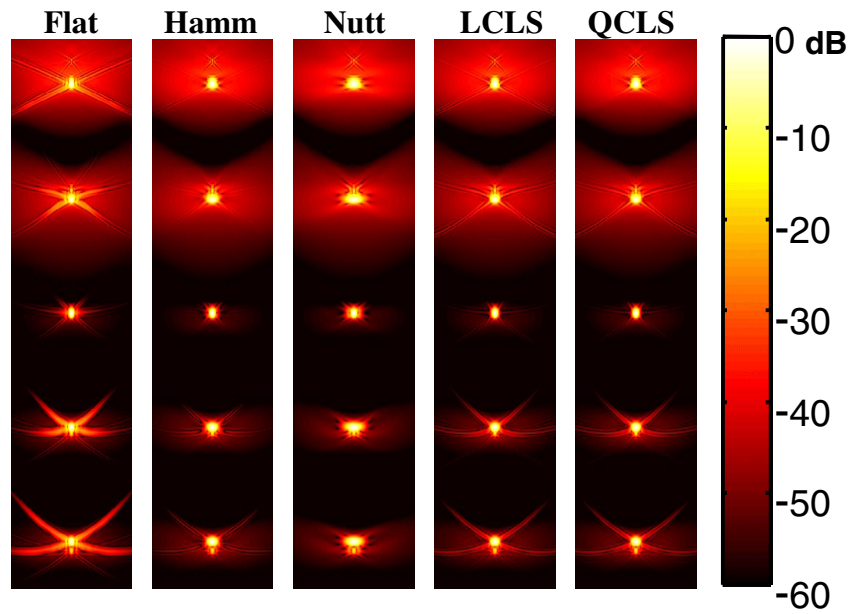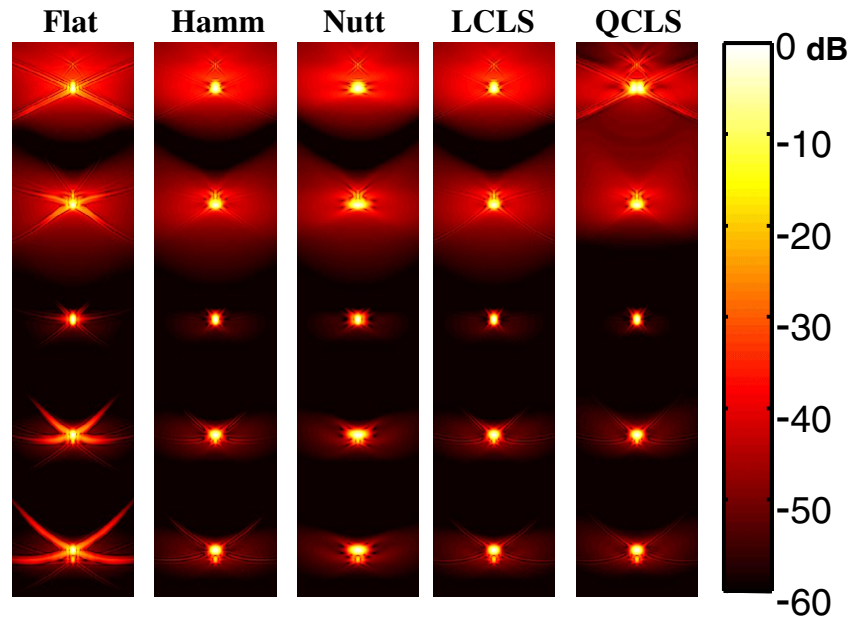
Fig. 4. Comparison of 2D psfs of different apodization profiles with range on dynamic receive. The CLS profiles were designed using a cyst radius of 0.4mm. The system had a transmit focus at 2cm (f/2) and then was dynamically focused and apodized at ranges of 1cm, 1.5cm, 2cm, 2.5cm and 3cm (f/1). Each image was normalized and log compressed to -60dB. Note the spreading of the mainlobe in the conventional windows psfs away from the transmit focus and the relatively constant mainlobe of the CLS apodized psfs.
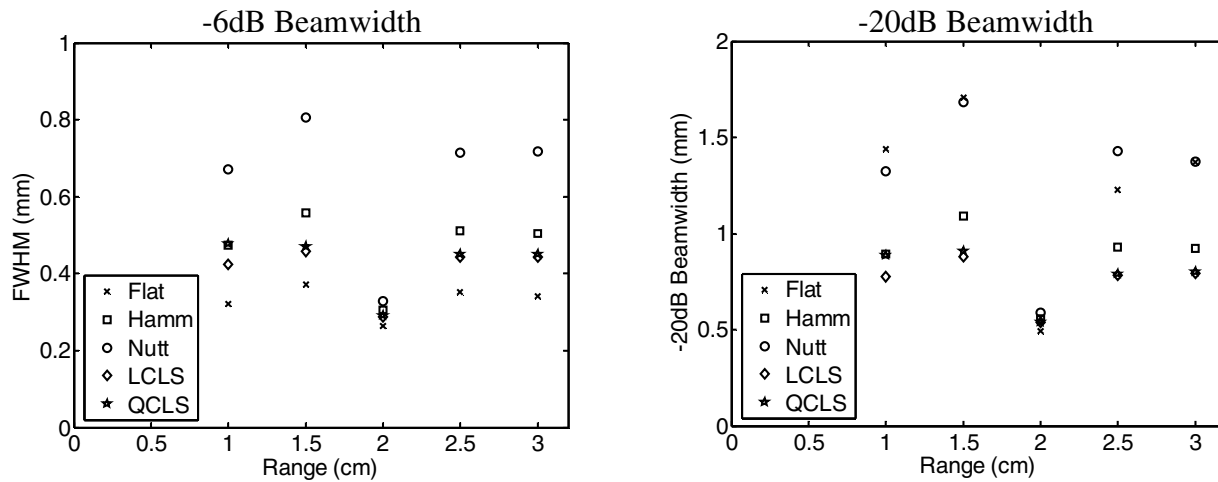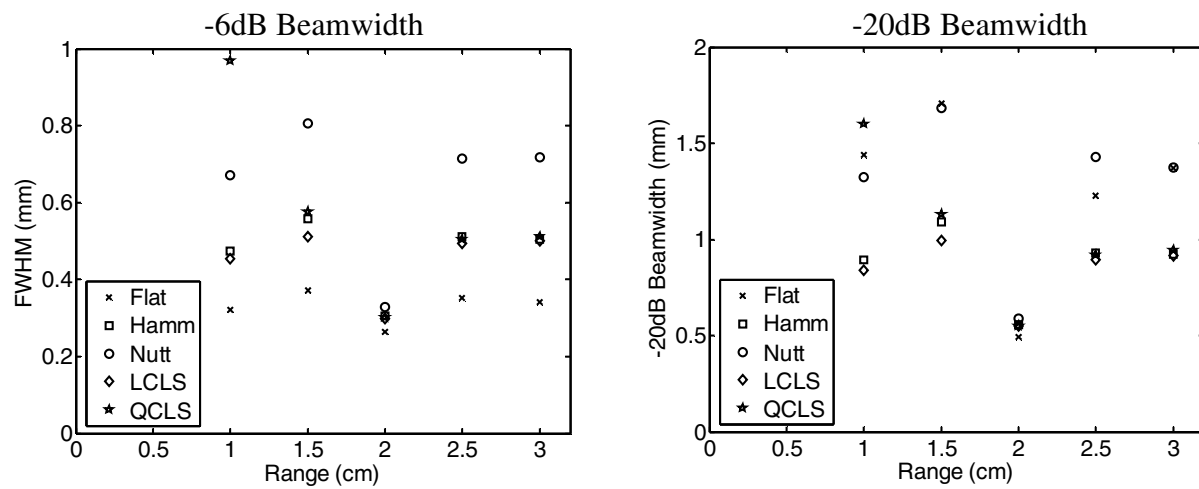
Fig. 5.  Comparison of the -6dB (FWHM) and -20dB beamwidths of the psfs for different apodization profiles with range on dynamic receive.  The CLS apodization profiles were designed using a cyst radius of 0.4mm.  The system had a transmit focus at 2cm (f/2) and then was dynamically focused and apodized at ranges of 1cm, 1.5cm, 2cm, 2.5cm and 3cm (f/1).  The FWHM and the -20dB beamwidths of the CLS psfs remain stable in range.  They also achieve the narrowest -20dB beamwidths away from the transmit focus.

Fig. 6. Comparison of 2D psfs of different apodization profiles with range on dynamic receive. The CLS profiles were designed using a cyst radius of 0.6mm. The system had a transmit focus at 2cm (f/2) and then was dynamically focused and apodized at ranges of 1cm, 1.5cm, 2cm, 2.5cm and 3cm (f/1). Each image was normalized and log compressed to -60 dB. Notice the greater sidelobe suppression of the CLS profiles in the deeper ranges compared to Fig. 4 above.

Fig. 7. Comparison of the -6dB (FWHM) and -20dB beamwidths of the psfs for different apodization profiles with range on dynamic receive. The CLS apodization profiles were designed using a cyst radius of 0.6mm. The system had a transmit focus at 2cm (f/2) and then was dynamically focused and apodized at ranges of 1cm, 1.5cm, 2cm, 2.5cm and 3cm (f/1). Notice the large FWHM of the QCLS algorithm compared to Fig. 5 at a range of 1cm, a phenomenon due to the algorithm's attempt to maintain constant energy of the psf inside the mainlobe region.
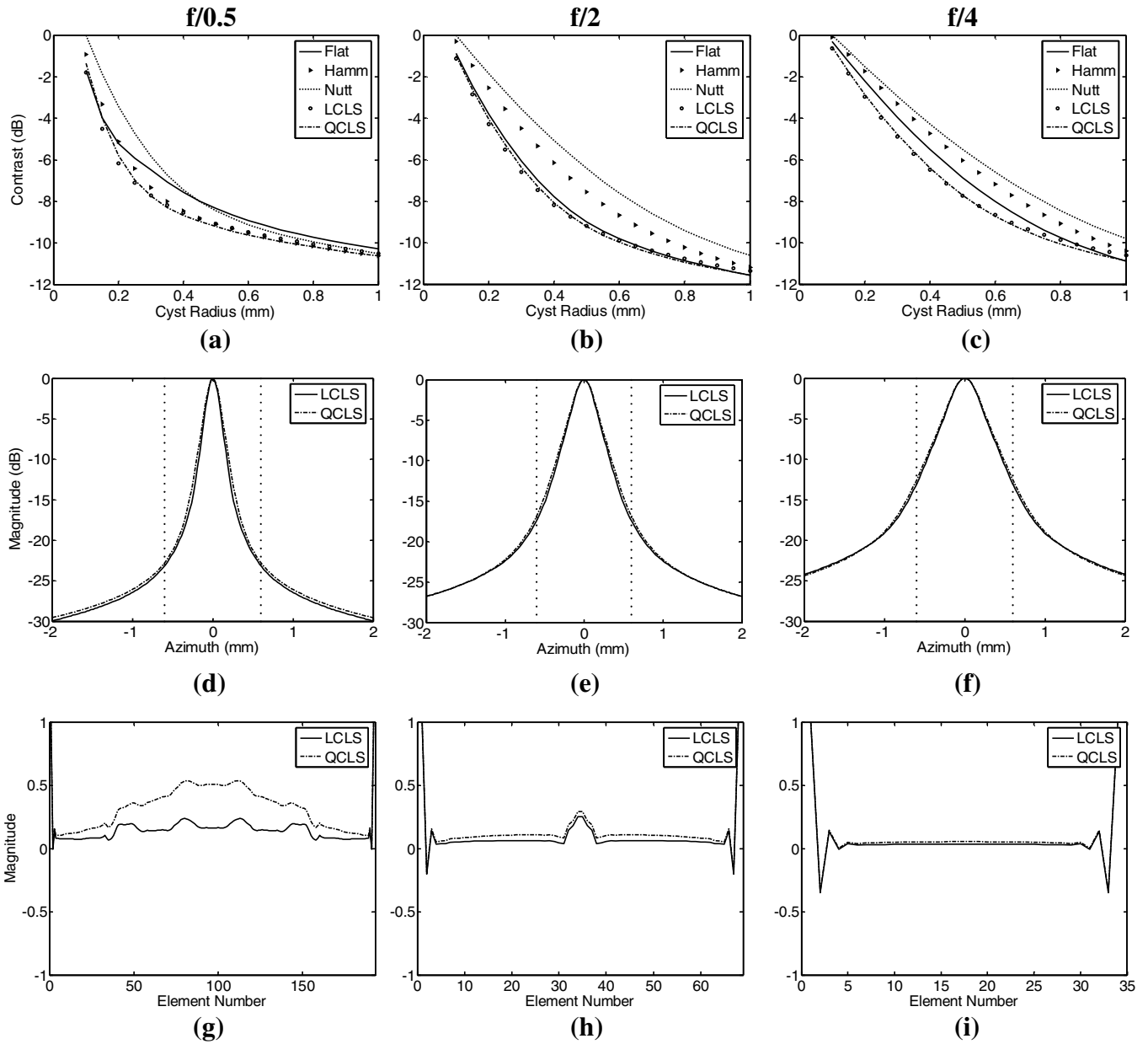
Fig. 8. Comparison of apodization profiles at different f/#'s on receive (f/0.5, f/2 and f/4). These simulations use the 10MHz linear array with fixed transmit focus at 2cm (f/4) and dynamic receive at 2cm. Panels (a)-(c) show contrast curves for the different apodization schemes (flat, Hamming, Nuttall, LCLS and QCLS). The second row of plots, (d)-(f), shows the integrated beamplots of the CLS profiles where the dotted line corresponds to the cyst boundary used to design the windows. Panels (g)-(i) show the magnitude of the CLS profiles across the aperture. The CLS algorithms produce better contrast at every cyst size for all f/#'s investigated than the Hamming and Nuttall windows.
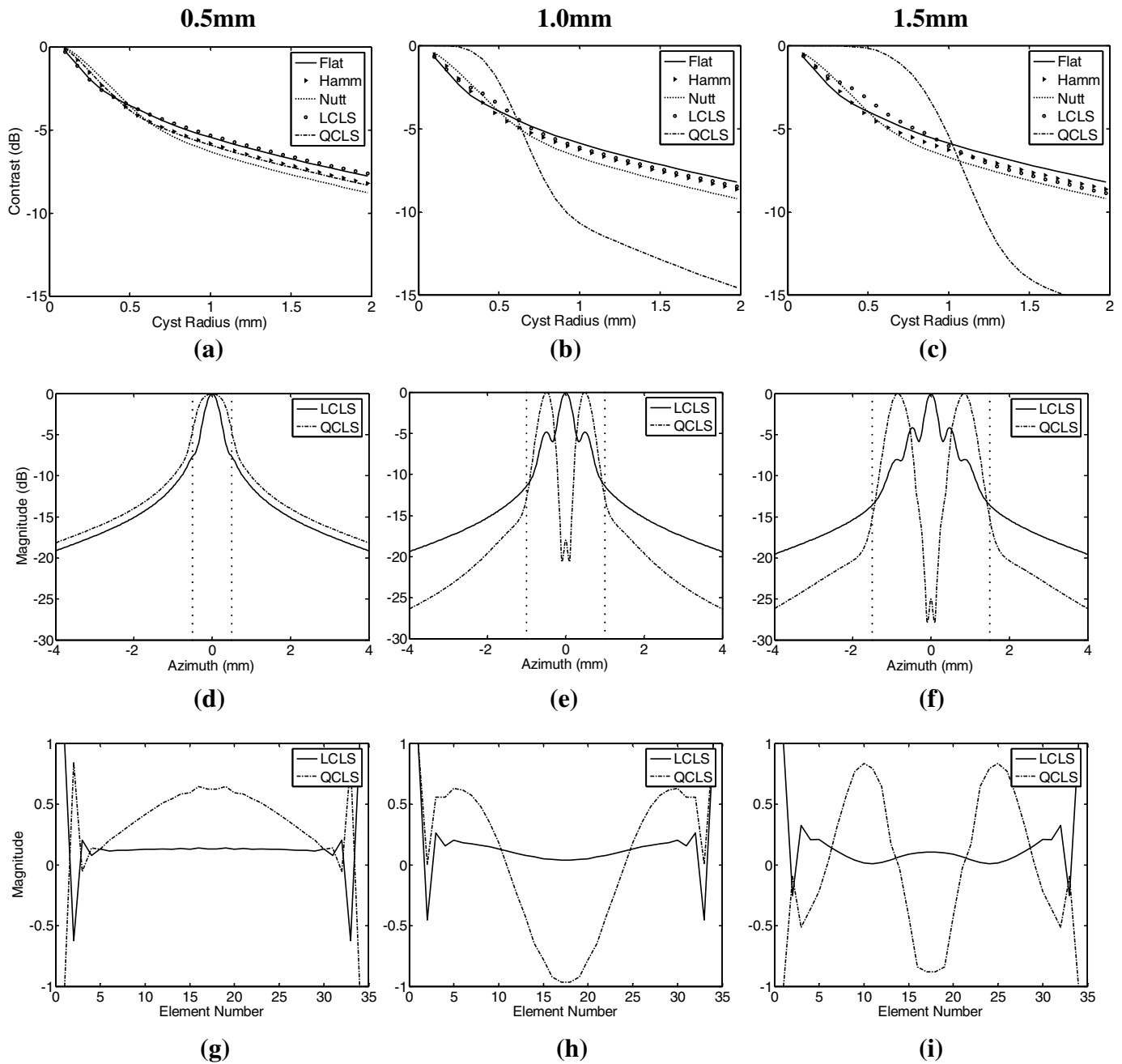
Fig. 9. Comparison of apodization profiles with large design cyst radius. Panels (a)-(c) plot the contrast curves for design radii of 0.5mm, 1.0mm and 1.5mm respectively. The second row of plots shows the integrated lateral beamplots and the third row of plots, panels (g)-(i), shows the LCLS and QCLS apodization profiles as a function of element number across the aperture. Note that for larger design radii, the QCLS algorithm results in psfs with multiple peaks in the mainlobe region.
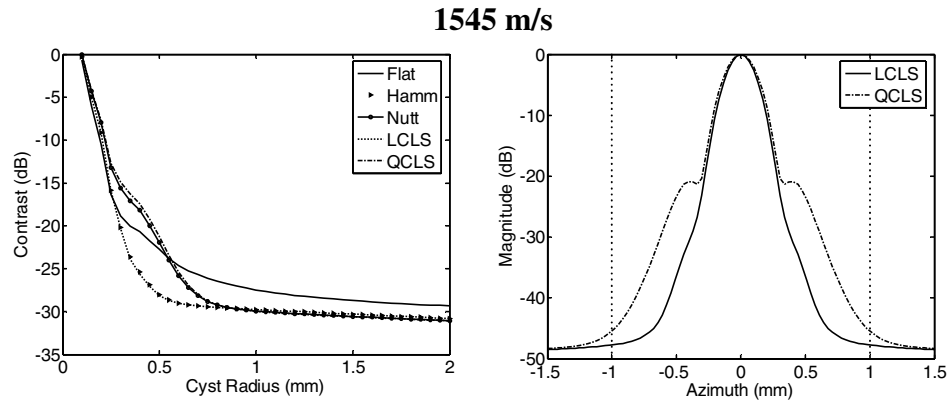
**1545 m/s**



Fig. 10. Contrast curves (left) and integrated lateral beamplots (right) for the CLS apodizations designed assuming the correct speed of sound (1545 m/s). The dotted vertical lines delineate the design cyst radius of 1.0mm. The LCLS and Hamming windows produced similar contrast curves.
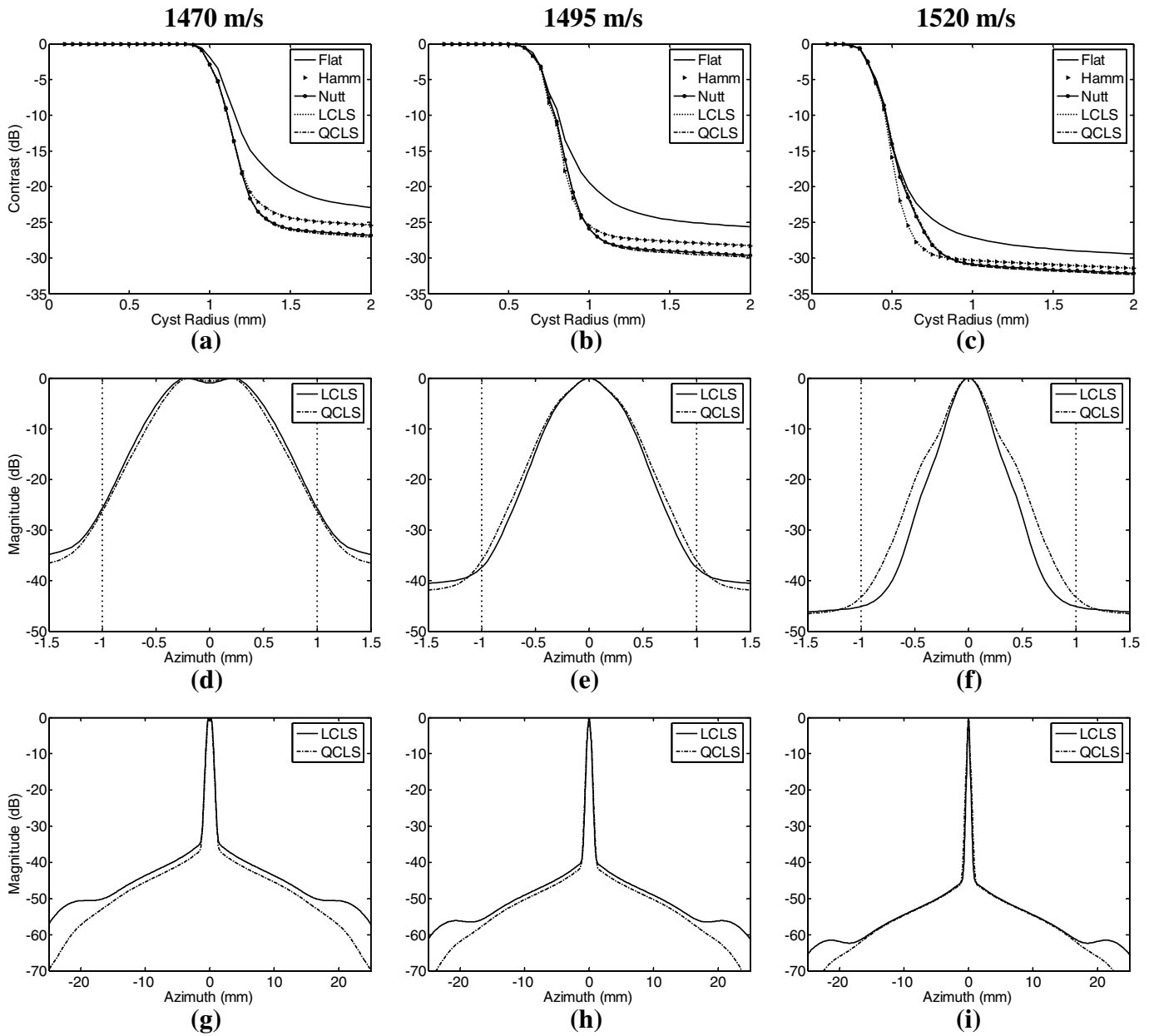
Fig. 11. Effect of assumed sound speed on the CLS algorithm. For these simulations the wave propagation speed was overestimated by 25m/s, 50m/s and 75m/s. The CLS profiles computed for 1545m/s were applied to the degraded psfs. Panels (a)-(c) show the resulting contrast curves. The Hamming and LCLS contrast curves are similar as are the Nuttall and QCLS curves. The second row, (d)-(f), plots the mainlobe region of the CLS apodized psfs where the dotted line delineates the design radius of 1.0mm. The entire lateral extent of the integrated beamplots for the CLS apodized psfs are shown in (g)-(i). The CLS algorithms remain quite stable for the sound speed errors investigated, where the worst cystic contrast is for the simulation corresponding to the grossest sound speed error of 75m/s.
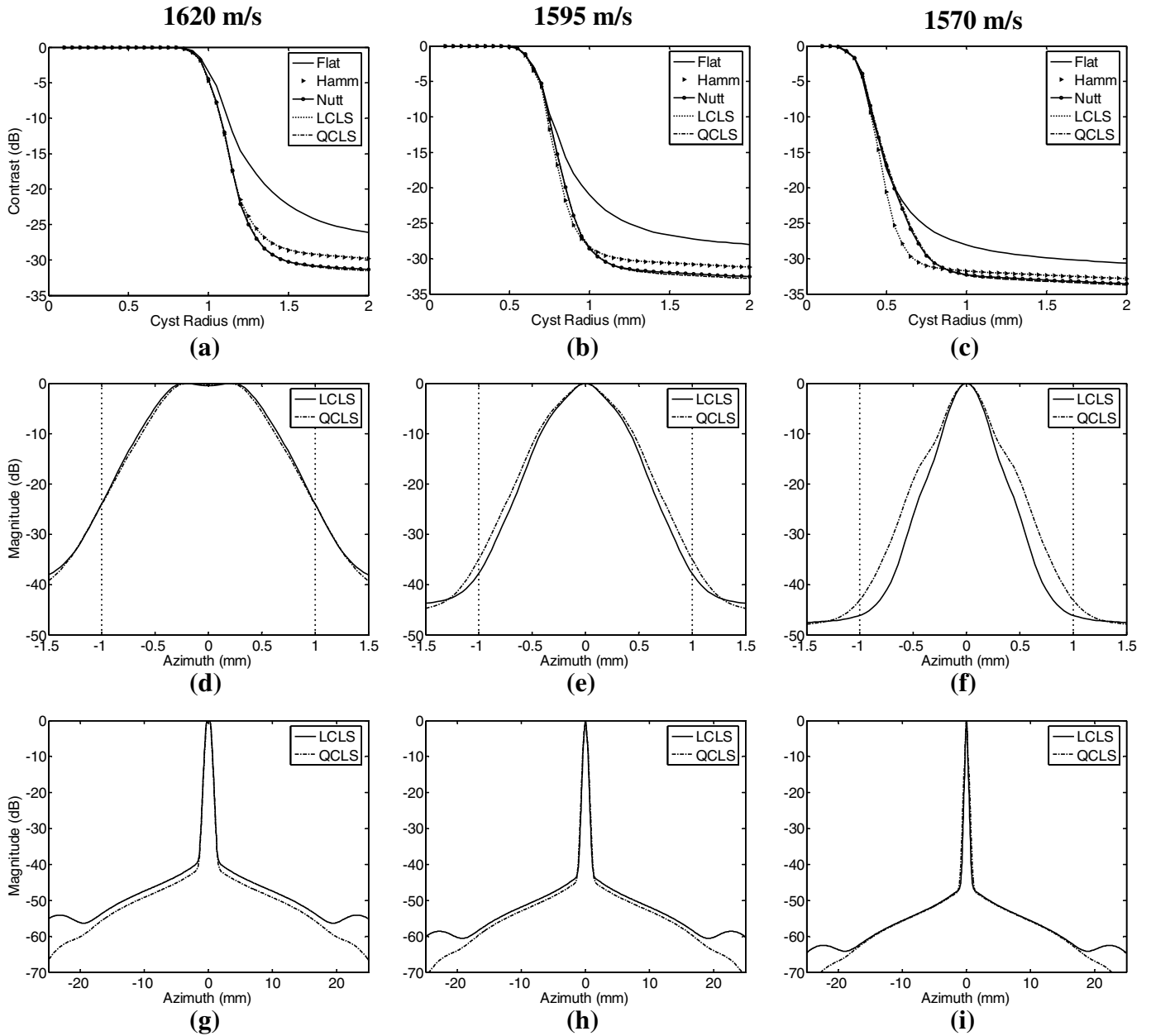
Fig. 12. Effect of assumed sound speed on the CLS algorithm. For these simulations the wave propagation speed was underestimated by 25m/s, 50m/s and 75m/s. The CLS profiles computed for 1545m/s were applied to the degraded psfs. Panels (a)-(c) show the resulting contrast curves. The Hamming and LCLS contrast curves are similar as are the Nuttall and QCLS curves. The second row of plots, (d)-(f), shows the mainlobe region of the CLS apodized psfs where the dotted line delineates the design radius of 1.0mm. The entire lateral extent of the integrated beamplots for the CLS apodized psfs is shown in (g)-(i). The CLS algorithms remain quite stable for the sound speed errors investigated; these results closely resemble those seen for the overestimated sound speeds in Fig. 11.
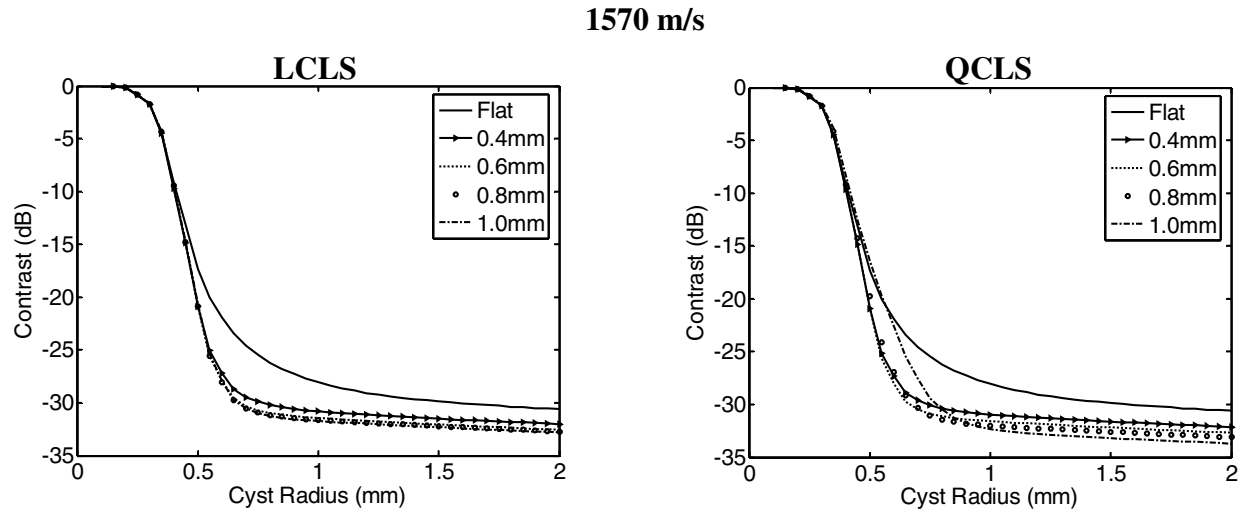
**1570 m/s**



Fig. 13. Effect of design cyst radius when the assumed sound speed has been underestimated by 25m/s. The LCLS (left) and QCLS (right) apodization profiles were designed for 0.4mm, 0.6mm, 0.8mm and 1.0mm cyst radii. The flat apodization contrast curve is shown for reference. The CLS profiles achieve better contrast than flat apodization across a wide range of cyst sizes. The LCLS and QCLS contrast curves remain stable in the presence of sound speed errors as the design cyst radius increases.
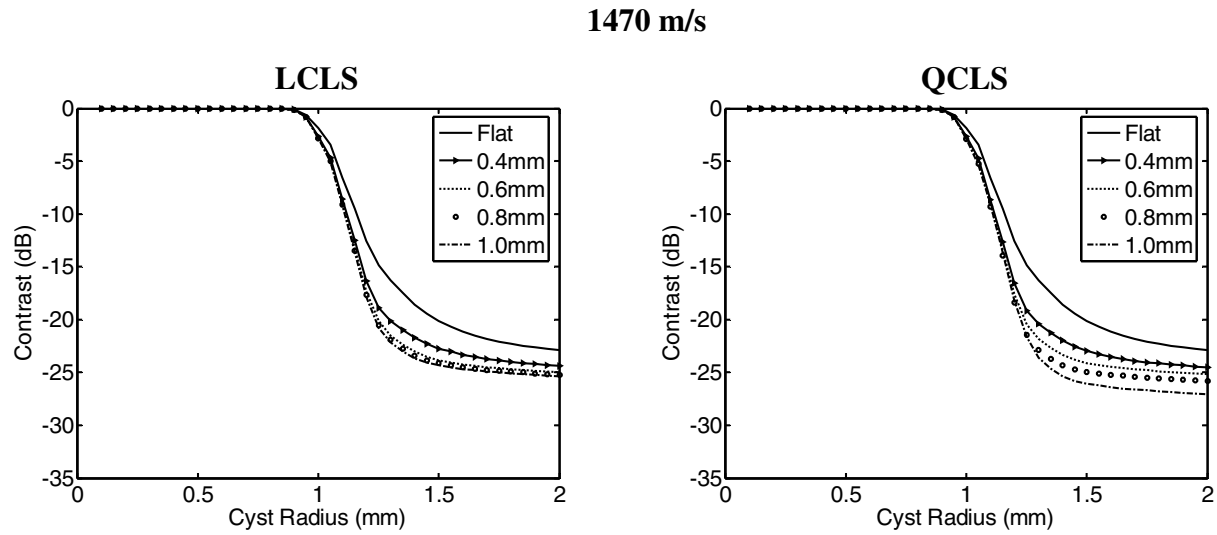
**1470 m/s**



Fig. 14. Effect of design cyst radius when the assumed sound speed has been grossly overestimated by 75m/s. The LCLS (left) and QCLS (right) apodization profiles were designed for 0.4mm, 0.6mm, 0.8mm and 1.0mm cyst radii. The flat apodization contrast curve is shown for reference. The LCLS and QCLS contrast curves remain stable in the presence of sound speed errors and in general contrast improves for larger design cyst radii.
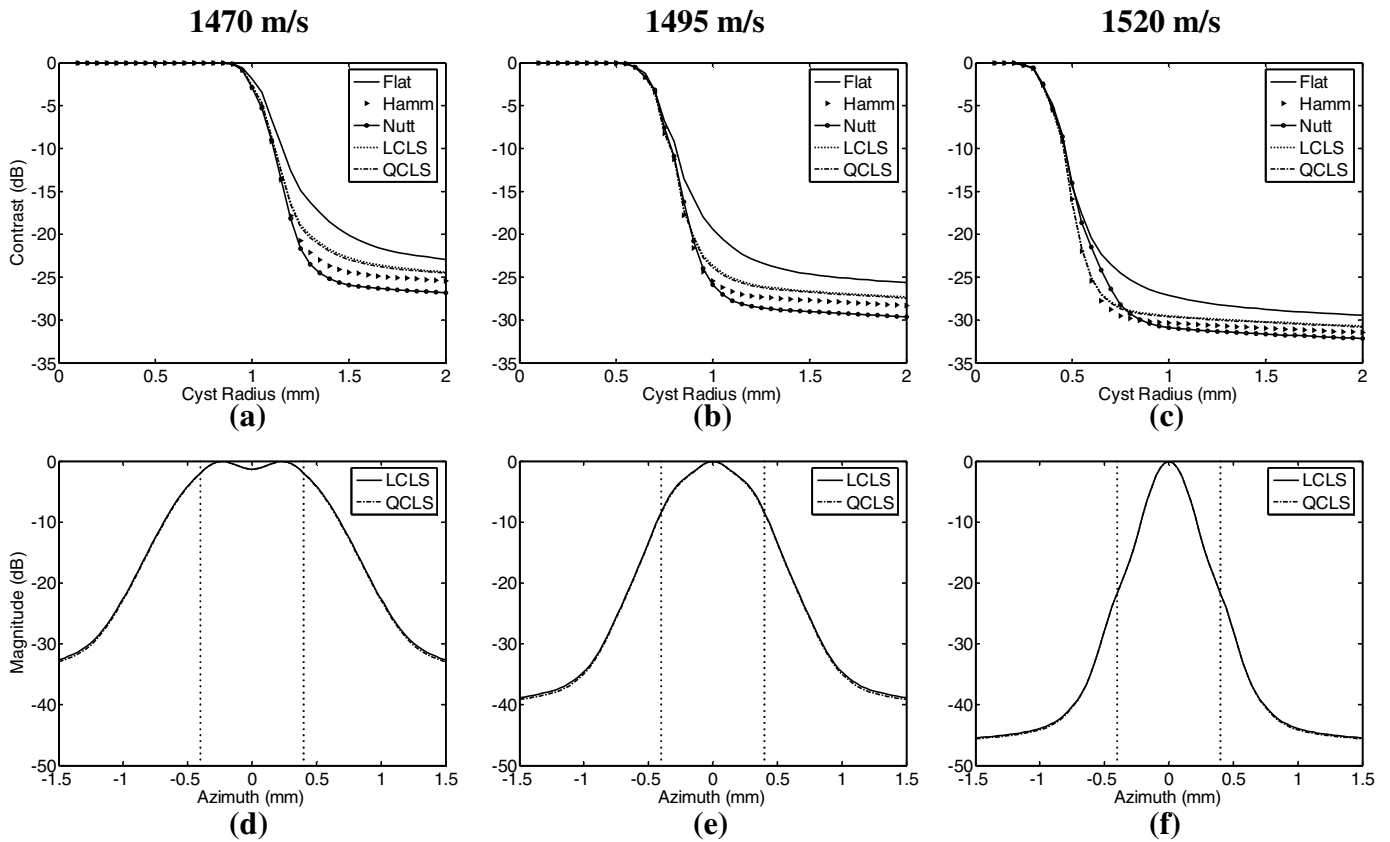
Fig. 15. Effect of assumed sound speed on the CLS algorithm for profiles designed using a small cyst radius of 0.4mm. For these simulations the assumed wave propagation speed was overestimated by 25m/s, 50m/s and 75m/s. The CLS profiles computed for the correct sound speed of 1545m/s were applied to the degraded psfs. The first row of plots, (a)-(c), shows the resulting contrast curves. Plots (d)-(f) show the mainlobe region of the CLS apodized psfs where the dotted line delineates the design radius of 0.4mm. Both CLS profiles produce similar lateral beamplots. The CLS algorithms remain quite stable for the sound speed errors investigated, however they do not achieve better contrast than the Hamming and Nuttall windows for the larger cyst sizes.